TOWARDS A SUBCELLULAR DESCRIPTION OF CHOLESTEROL HOMEOSTASIS

A DISSERTATION

SUBMITTED TO THE FACULTY OF THE GRADUATE SCHOOL

OF THE UNIVERSITY OF MINNESOTA

BY

KATHERINE MURATORE

IN PARTIAL FULFILLMENT OF THE REQUIREMENTS

FOR THE DEGREE OF

DOCTOR OF PHILOSOPHY

EDGAR A. ARRIAGA, ADVISOR

JANUARY, 2018

Acknowledgements

This work would not have been possible without the guidance of my thesis advisor, Edgar A. Arriaga. You have taught me how to examine biochemical problems with the techniques and rigor of an analytical chemist, skills that will remain with me for the rest of my career. Thank you for never wavering in your belief that I would complete this (despite my vocal self-doubt), and enabling me to stand on the shoulders of giants. I also would like to thank my committee members, Deb Ferrington, Yue Chen, Sharon Murphy, and Ling Li.

It has been a privilege to work with all the Arriaga group members, but I want to individually acknowledge Heather Brown and Deirdre Manion-Fisher. There is not one piece of data in this thesis that I did not run by Heather. Your input and analytical eye were invaluable, and I will miss you greatly at my next lab. Deirdre, you were my spirit guide in the lab and have become one of my most supportive friends. Thank you for always telling me my feelings were valid, emphasizing the importance of self-care, helping me make figures, and working next to me while I wrote this dissertation.

I would not have become a scientist without the example and advice of my mentor, Dyann Wirth. I am so proud to be the second scientist in our family, and I strive to become as respected in the scientific community as you. Jay Bangs, my first research mentor, thank you for introducing me to protozoans and teaching me the “lab savvy” I needed to succeed in graduate school.

My fiancé, Mark Smalley, was a constant source of love and support during my entire graduate career. Thank you for patiently talking me through numerous crises, and always believing in my skills as a scientist. Your mind for data analysis, interpretation, and programming is unlike any I have ever encountered. Thank you for your constant assistance and feedback. Also, thanks for being my example for graduate and postdoctoral success, and for providing me with your thesis formatting template. I deleted all the words you wrote because CloudSat is going to fall out of the A-Train on my defense day ☺.

Thank you to my parents for loving and supporting me as I grew up and through my 7.5 years of postsecondary education. Thank you both for putting up with my relentless phone calls and providing me with everything I needed (both emotionally and financially) to complete my education. Dad, thank you for patiently proofreading this thesis. My brother, Mike and sister-in-law, Jordan, thank you for moving to Minneapolis to be closer to me (you're moving to LA now too, right?), and making my last two years of graduate school much more enjoyable.

Abstract

The role of autophagy in the maintenance of skeletal muscle cholesterol homeostasis has not been investigated prior to this thesis. Cholesterol abundance has two known inputs: (i) *de novo* synthesis via the mevalonate pathway, and (ii) adsorption of dietary cholesterol via lipoprotein receptor mediated uptake. Breakdown of cellular cholesterol depots by autophagy, known as macrolipophagy, may contribute as a third source of cellular cholesterol. Furthermore, the selectivity of macrolipophagy and the subcellular distribution of cholesterol may play integral roles in cholesterol homeostasis that have not been investigated.

The driving hypothesis in the field is that autophagy contributes to cholesterol abundance through macrolipophagy and regulation of cholesterol synthesis. In this thesis, new methods were developed for macrolipophagy organelle analysis in tissues and to determine lipid droplet size. The first method is the initial step in measuring macrolipophagy at the individual organelle level. The second method, which involves the characterization of lipid droplet size, is critical because of the impact of dysfunctional macrolipophagy on cholesterol homeostasis.

Equally important is the characterization of the inter-regulation of autophagy and cholesterol homeostasis. Inhibition of autophagy using ATG7 siRNA suggests that autophagy plays a key role in mediating cholesterol abundance and the

mevalonate pathway (the parent pathway of cholesterol synthesis and protein prenylation). Together, these two advances could contribute to the future refinement of how autophagy and cholesterol homeostasis are inter-regulated at the subcellular level.

Table of Contents

Acknowledgements i

Abstract iii

List of Tables vii

List of Figures viii

List of Abbreviations ix

Chapter 1: Introduction 1

1. Thesis Overview 2
2. Current Understanding of Autophagy and Cholesterol Homeostasis 6
   - 2A. Autophagy 6
   - 2B. Selective Autophagy of Lipid Droplets 9
   - 2C. Cholesterol Homeostasis 13
3. Advancing Understanding of Autophagy and Cholesterol Homeostasis 18
   - 3A. Capillary Electrophoresis with Laser Induced Fluorescent Detection of Autophagy Organelles 18
   - 3B. Nanoparticle Tracking Analysis of Lipid Droplets 21
   - 3C. Investigation of Mevalonate Pathway Regulation by Autophagy 23

Chapter 2: Capillary Electrophoresis with Laser Induced Fluorescent Detection of Individual Autophagy Organelles Isolated From Liver Tissue 25

- Summary 26
- Introduction 27
- Experimental Section 30
- Results and Discussion 39
- Concluding Remarks 54

Chapter 3: Sizing Lipid Droplets from Adult and Geriatric Mouse Liver Tissue Via Nanoparticle Tracking Analysis 55

- Summary 56
- Introduction 57
- Experimental Section 61
- Results and Discussion 66
- Concluding Remarks 79

Chapter 4: Defining the Inter-Regulation of Autophagy and Cholesterol Homeostasis 80

- Summary 81
- Introduction 82
- Materials and Methods 84
- Results 94
- Discussion 107

Chapter 5: Conclusions and Future Directions 113

1. Overall Conclusions 114
2. Future Directions 118
   - 2A. Introduction 118

2B. Measurement of Autophagy Flux by CE-LIF 118
2C. Selective Monitoring of Macrolipophagy Flux 120
2D. Confirmation of the Regulation of the Mevalonate Pathway by Autophagy 123

Bibliography **128**

Appendix 1: Supplementary Information to Chapter 2 ..... **139**
Supplementary Methods (Chapter 2) **140**
Supplementary Figure 1 (Chapter 2) **141**
Supplementary Figure 2 (Chapter 2) **142**
Supplementary Figure 3 (Chapter 2) **143**
Supplementary Figure 4 (Chapter 2) **144**
Supplementary Figure 5 (Chapter 2) **145**
Supplementary Figure 6 (Chapter 2) **146**
Supplementary Figure 7 (Chapter 2) **147**

Appendix 2: Supplementary Information to Chapter 3 ..... **148**
Supplementary Data Analysis (Chapter 3) **148**
Supplementary Tables (Chapter 3) **149**
Supplementary Figure 1 (Chapter 3) **151**
Supplementary Figure 2 (Chapter 3) **152**
Supplementary Figure 3 (Chapter 3) **153**
Supplementary Figure 4 (Chapter 3) **154**
Supplementary Figure 5 (Chapter 3) **155**
Supplementary Figure 6 (Chapter 3) **156**

Appendix 3: Supplementary Information to Chapter 4 ..... **157**
Supplementary Methods (Chapter 4) **157**
Supplementary Figure 1 (Chapter 4) **158**
Supplementary Figure 2 (Chapter 4) **159**
Supplementary Figure 3 (Chapter 4) **160**
Supplementary Figure 4 (Chapter 4) **161**
Supplementary Figure 5 (Chapter 4) **162**

List of Tables

Chapter	Table Number	Title	Page
3	1	Standard Polystyrene Latex Nanospheres	69
3	2	Dilution series of 203nm standard polystyrene latex nanospheres.	69
3	3	Lipid Droplet Stabilty Study	74
3	4	Lipid Droplets from Adult and Geriatric Mice	77
4	1	Summary of canonical pathways significantly affected by ATG7 siRNA treatment	105
4	2	ATG7 siRNA treatment resulted in increase abundance of proteins involved in the mevalonate pathway	106

List of Figures

Chapter	Number	Figure Title	Page
1	1	Organelles Involved in Autophagy	7
1	2	Basic Morphology of Lipid Droplets	10
1	3	LDL Receptor Mediated Cholesterol Uptake	14
1	4	Cholesterol Synthesis	15
1	5	Diagram of Home-Built CE-LIF instrument	20
1	6	Schematic of NTA Optical Configuration	22
2	1	Representative electropherograms of individual autophagy organelles	41
2	2	Autophagy organelle DyLight488 intensity and electrophoretic mobility distributions	44
2	3	Comparison of intensity and electrophoretic mobility distributions of organelles labeled with DyLight488 Anti-LC3 or Isotype control	47
2	4	Selection of DyLight488-conjugated anti LC3 antibody concentration for analysis of autophagy organelles from tissue samples	51
2	5	Reproducibility of technical replicates.	53
3	1	Histograms and size percentiles of polystyrene latex nanosphere standard size distributions.	70
3	2	Histogram of corrected mouse liver lipid droplet size distribution	74
3	3	Stability of uncorrected lipid droplet size distribution	75
3	4	QQ plot of adult and geratric mice	78
4	1	The mevalonate pathwy synthesizes cholesterol through isoprenoid intermediates	83
4	2	ATG7 knockdown affects cholesterol abundance and prenylation.	96
4	3	ATG7 knockdown affects cholesterol synthesis	98
4	4	Relative cholesterol synthesis gene expression in ATG7 siRNA treated and negative control siRNA treated cells.	100
4	5	Significantly changed proteins mapped to a KEGG diagram of the mevalonate pathway	103
4	6	Working model of mevalonate pathway regulation by autophagy.	104
5	1	Flow-gram of Lipid Tox Red Labeled Lipid Drop	122
5	2	Mean pixel intensity per cell vs image acquisition time.	125
5	3	Computational Cell Segmentation Example	126

List of Abbreviations

Phrase	Abbreviation
acyl-CoA:acyltransferase	ACAT
analysis of variance	ANOVA
arginine	Arg
autophagy related gene	ATG
capillary electrophoresis	CE
capillary electrophoresis with laser induced fluorescent detection	CE-LIF
dynamic light scattering	DLS
Dulbecco's modified eagle medium	DMEM
dimethyl sulfoxide	DMSO
ethaminetetraacetic acid	EDTA
ethylene-bis(oxyethylenenitrilo)tetraacetic acid	EGTA
fluorophore/protein	F/P
fetal bovine serum	FBS
farnesyl diphosphate transferase type 1	FDFT
farnesyl diphosphate synthase	FDPS
false discovery rate	FDR
green fluorescent protein	GFP
heavy to light	H/L
high density lipoprotein	HDL
4-(2-hydroxyethyl)-1-piperazineethanesulfonic acid	HEPES
HMG-CoA reductase	HMGCR
Ingenuity Pathway Analysis	IPA
microtubule-associated protein 1A/1B-light chain 3	LC3
low density lipoprotein	LDL
lipid droplets	LDs
lysine	Lys
mouse embryonic fibroblast	MEF
nanoparticle tracking analysis	NTA
phosphate buffered saline	PBS
posterior error probability	PEP
personal protective equipment	PPE
parts per million	ppm
quantitative polymerase chain reaction	qPCR
quantile quantile	QQ
standard error of mean	SEM
stable isotope labeling in culture	SILAC
statistical overlap theory	SOT
squalene synthase	SQS
sterol regulatory element binding protein	SREBP
transmission electron microscopy	TEM

Chapter 1: Introduction

Katherine Muratore wrote this chapter and illustrated Figures 4 and 5. Deirdre Manion-Fischer illustrated Figures 1, 2, 3, and 6.

1. Thesis Overview

Muscle mass and function decrease with aging in skeletal muscle, contributing to decreased mobility, an increased number of fall related injuries and increased frailty.[1] Despite a decrease in muscle mass, lipid accumulation also occurs in skeletal muscle of aging patients.[2–4] Blockage of autophagy (degradation of cellular components) results in the loss of muscle mass.[5,6] The role of autophagy in the maintenance of skeletal muscle lipid (cholesterol and tryglyceride) homeostasis has not been investigated prior to this thesis.

Cholesterol homeostasis refers to the abundance and distribution of cholesterol in cells. Cells obtain cholesterol from two known sources, *de novo* synthesis via the mevalonate pathway and adsorption of dietary cholesterol via lipoprotein receptor mediated uptake. A selective form of autophagy known as macrolipophagy regulates the release of neutral lipids stored in lipid droplets, including cholesterol.[7–9] Regulation of cholesterol depots in these organelles, through size or cholesterol abundance, may be contributing as a third source of cellular cholesterol. Furthermore, the subcellular distribution of cholesterol and the selectivity of macrolipophagy may play important roles in cholesterol homeostasis that have not been investigated.

The central hypothesis of this thesis is that autophagy contributes to cholesterol abundance through macrolipophagy and regulation of cholesterol synthesis in

aging muscle. To begin testing this hypothesis, it was imperative to develop tools to selectively monitor macrolipophagy, assess the size of cholesterol depots (lipid droplets) and investigate changes in cholesterol abundance, synthesis, and uptake that occur with inhibition or blockage of autophagy. The first objective of this thesis was to develop new methods for individual macrolipophagy organelle analysis in tissues. To demonstrate the feasibility of this method in a biological system, a pilot study was performed to determine age associated changes in lipid droplet size. The second objective of this thesis was to determine the role of autophagy in regulating cholesterol synthesis.

Macrolipophagy is one of several forms of selective autophagy. Individual organelle measurements are needed to determine what fraction of autophagy organelles are associated with lipid droplets. The work in Chapter 2 is the development of a technique using capillary electrophoresis with laser induced fluorescent detection (referred hereafter as “CE-LIF”) to measure individual autophagy organelles from tissues. DyLight488-conjugated anti-LC3 antibodies were used to label the endogenous LC3 present on autophagy organelles isolated from murine liver tissue prior to CE-LIF analysis. This method is capable of detecting changes in a known model system of altered autophagy and the antibody labeling was found to be both specific and reproducible. This method is both the first application of individual organelle CE-LIF to measure the properties of autophagy organelles isolated from tissue and the first demonstration of

fluorophore conjugated primary antibodies as individual organelle labels for CE-LIF.

While tissue lipid accumulation is associated with aging,[2–4] it is unknown if impaired autophagy associated with aging results results in changes to the size and composition of lipid droplet cholesterol depots. This calls for the development of a technical capability to enable the measurement of individual lipid droplet sizes in model systems of aging and impaired autophagy. The work in Chapter 3 is the first application of Nanoparticle Tracking Analysis (referred to hereafter as “NTA”) to measure lipid droplet size. An NTA instrument was evaluated and determined to be adequate for measuring lipid droplet size. NTA was subsequently used to evaluate the stability of a lipid droplet preparation over a period of time. We also applied NTA to compare relative size distributions of lipid droplets from adult and geriatric mice liver tissues, and uncovered smaller lipid droplet size distributions in geriatric mice. These are the first measurements of lipid droplet size in a comparative aging study.

To determine if autophagy contributes to cholesterol abundance through macrolipophagy in aging muscle, the effect of altered autophagy on cholesterol synthesis in cells associated with skeletal muscle needed to be elucidated. The work in Chapter 4 is a new working model for regulation of the mevalonate pathway by autophagy and provides a framework for investigating autophagy’s

contribution to cholesterol homeostasis in aging muscle. In cells associated with skeletal muscle, it was observed that autophagy inhibition increased cholesterol abundance and decreased the expression of cholesterol synthesis genes, despite accumulation of cholesterol synthesis proteins. We report that ATG7 knockdown impacts gene expression and protein abundance in the mevalonate pathway and that increased cholesterol abundance and impaired autophagy are key factors in mediating these effects. Prior to this study, the regulation of cholesterol synthesis by autophagy was completely unexplored in cells associated with skeletal muscle.

In conclusion, this thesis advances the technical capability of individual organelle measurement and furthermore advances the understanding of the role of autophagy in maintaining lipid homeostasis. CE-LIF of individual autophagy organelles in tissue is the first step toward measuring macrolipophagy in aging muscle. Measurement of lipid droplets by NTA revealed a smaller lipid droplet size distribution in geriatric mouse liver, suggesting decreased cholesterol storage and changes in lipid droplet composition. Because autophagy plays a key role in mediating mevalonate pathway gene expression and protein abundance, it serves as a framework for further investigation into the contribution of macrolipophagy to cholesterol abundance in aging skeletal muscle.

2. Current Understanding of Autophagy and Cholesterol Homeostasis

2A. Autophagy

Autophagy is a cellular degradation process that involves individual organelles that ingest, transport, and break down cellular material. Autophagy, working in coordination with the ubiquitin-proteosome pathway,[10,11] is responsible for degradation of large cellular components, including misfolded protein aggregates, dysfunctional organelles, and microorganisms.[12] Autophagy is extremely important in the maintenance of overall cellular homeostasis, including growth, differentiation, development, and survival.[13] There are three forms of autophagy: microautophagy, chaperone mediated autophagy, and macroautophagy.[14] The macroautophagy process (referred to hereafter as "autophagy") results in the sequestration of bulk cellular components into double membrane vesicles called autophagosomes, which undergo subsequent fusion with lysosomes for cargo degradation.[15] Autophagy (Figure 1) is an evolutionarily conserved process and involves several specialized organelle types, including phagophores, autophagosomes, and autolysosomes.[14]

Autophagosome formation in mammals is controlled by the function of ATG (autophagy related) proteins in ubiquitin-like conjugation systems.[16] While there are many ATG protein complexes involved in autophagosome formation, the work in this thesis focused on E1-like enzyme ATG7 and LC3, the most commonly employed autophagosome marker. LC3 is activated by ATG7[17,18] and

LC3-II is formed when cytosolic LC3-I is conjugated to phosphatidylethanolamine.[19] Activated LC3-II localizes to phagophores, autophagosomes, and autolysosomes and is required for autophagosome maturation.[20] Autophagy flux can be considered the rate of degradation activity through the autophagy pathway[21] and includes the formation of LC3-II positive autophagosomes, fusion with lysosomes, and subsequent cargo release.[22]

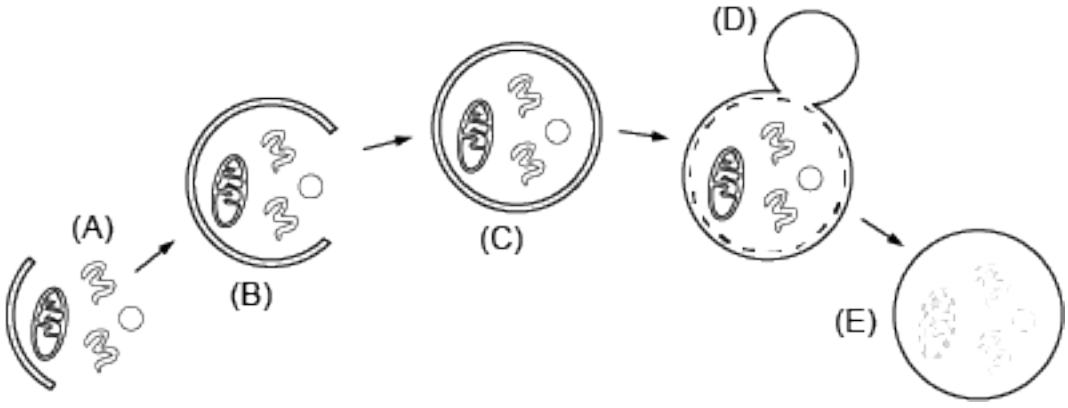

Figure 1. Organelles Involved in Autophagy. The morphology of autophagy organelles is sketched above. Cytoplasmic components (A), including other organelles, are engulfed by the phagophore membrane (B) to form the double membrane autophagosome (C). The autophagosome subsequently fuses a lysosome (D) to enable degradation of cellular components by lysosomal enzymes in an autolysosome (E).

Currently available techniques for monitoring autophagy include western blot, transmission electron microscopy (TEM), fluorescent microscopy, and flow cytometry.[23] Western blots are commonly used to measure the formation of autophagosome marker LC3-II, but a bulk increase in LC3-II is inadequate to determine flux through the autophagy pathway.[23–25] However, the measurement of LC3-I and LC3-II in the presence of lysosomal inhibitors by western blot is a suitable method for determining autophagy flux.[24,25] An increase in LC3-II on a western blot could suggest more autophagy organelles containing that marker, or an increase in LC3-II density on the surface of existing autophagy organelles.

Multiple techniques have been developed to monitor autophagy. Autophagy organelles can be visualized by both TEM[26–28] and fluorescent microscopy,[29,30] but these techniques have significant limitations. TEM is labor intensive and distinguishing among the organelles involved in autophagy can be limited by user interpretation bias.[31] Visualization of individual GFP-LC3-II positive organelles in microscopy images is not a high-throughput process. Individual cell[32–34] and individual organelle[33,35,36] flow cytometry autophagy assays have been reported, but these methods are either contingent on the overexpression of GFP-LC3 fluorophore conjugates, pH-sensitive lysosomal probes, or fluorophore conjugated secondary antibodies. The requirement of GFP-LC3 fluorophore conjugate expression limits the applicability of the technique to genetically

modified cell lines and animal models, while lysosomal probes are only capable of labeling autophagosomes that have fused with lysosomes.

A method capable of measuring individual autophagy organelles isolated from tissues would greatly complement existing bulk methodologies for measuring autophagy and address the limitations of flow cytometry-based autophagy measurements. A method based on individual autophagy organelle measurements will enable further development of methods to determine what type of cargo is being degraded in each autophagy organelle and measure changes that occur in co-existing forms of selective autophagy. A method for measurement of individual autophagy organelles is described in Chapter 2.

2B. Selective Autophagy of Lipid Droplets

There are selective forms of autophagy that are capable of breaking down specific substrates, including other organelles, such as lipid droplets. Age-related decreases in autophagic activity result in an accumulation of dysfunctional organelles and proteins and a decrease in overall protein turnover, contributing to age related malfunctioning of numerous biological processes.[37] These specialized forms of autophagy may be affected differently by aging.

Macrolipophagy is a form of selective autophagy in which autophagy related organelles deliver intact or portions of lipid droplets (referred to hereafter as

"LDs") to lysosomes for degradation.[8,38,39] LDs (Figure 2) are specialized organelles that consist of a core of lipid esters and cholesterol esters, surrounded by a phospholipid monolayer surface that is coated by proteins known as perlipins.[40] LDs function as both cellular energy reserves and provide building blocks for membrane synthesis.[41] Although large LDs are characteristic of adipocytes, LDs are also found in all cells and range in sizes from 0.1 to 10μm.[8] Macrolipophagy[8,38,39] and cytosolic LD-associated lipases[42] both work to mobilize fatty acids and cholesterol from LDs.

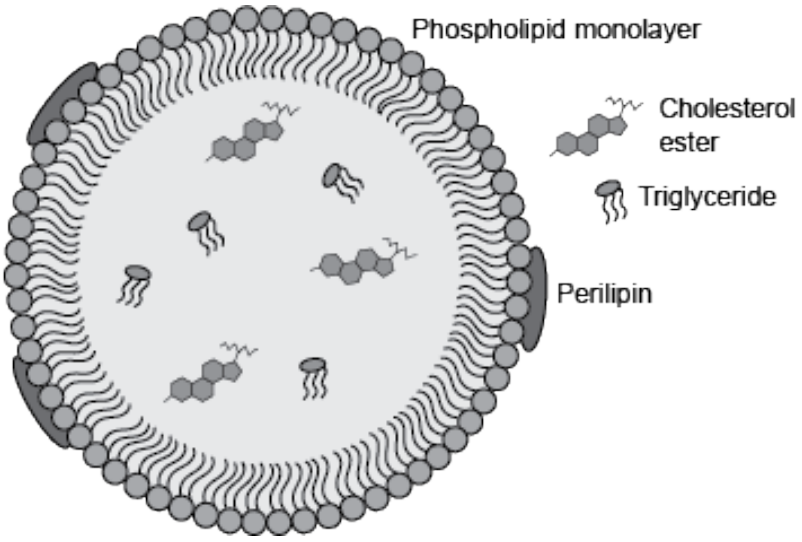

Figure 2. Basic Morphology of Lipid Droplets. A phospholipid monolayer surrounds a core of neutral lipids, including cholesterol esters and triglycerides. Perlipins, lipid droplet associated proteins, are present at the surface.

Dysregulation of lipid droplet size and number is associated with a multitude of lipid storage associated disorders, including lipodystrophies, obesity, cachexia, atherosclerosis, and non-alcoholic fatty liver disease (NAFLD).[43] Thus, measuring LD size is necessary to advance the understanding of the basic mechanisms governing diseases associated with dysregulation of lipid droplet sizes.

Confocal fluorescent microscopy is the method most often used for measuring lipid droplet size.[44–46] Numerous commercially available lipophilic dyes, including Oil Red O, Nile Red, and BODIPY, enable visualization of LDs in both cells and tissues[47–50] and allow the lipid droplet size to be quantified via image analysis software.[51] These techniques are not high throughput, and because lipophilic dyes can be incorporated into all lipid rich structures, microscopy images must be interpreted with caution. To be certain of lipid droplet identification, colocalization experiments with *bona-fide* lipid droplet markers (such as LD surface protein PLIN-2[52]) are required. While staining of LD in fixed cells is relatively straightforward, tissues must be embedded, sectioned, and stained prior to visualization by confocal microscopy,[49] a significant time investment. In addition, confocal microscopy has an optical resolution of 180nm in the x-y direction,[53] further limiting its use for size measurements of LDs in non-adipocytes.

LDs can also be imaged in cells by anti-Stokes Raman Scattering[54] and Stimulated Raman Scattering.[55] These label free methods are a technical improvement over fluorophore based visualization, but they require a sophisticated instrumental setup and are limited by the relatively low signal intensity, poor reproducibility, and long acquisition time associated with all Raman-based imaging techniques.

Dynamic light scattering (DLS) has been used for ensemble measurement of lipid droplet size distribution.[44] This method is incapable of resolving the sizes of individual particles and the obtained size distribution is greatly affected by the presence of aggregates or large particles in the sample. A non-destructive method capable of measuring individual lipid droplet size distributions from isolated lipid droplet populations would greatly complement existing methods for LD size measurement, and enable size measurements to be taken prior to LD analysis by mass spectrometry or proteomics. A method for individual LD size measurements is described in Chapter 2.

2C. Cholesterol Homeostasis

Cholesterol is an essential part of cell membranes. It determines membrane fluidity, participates in cellular signaling and trafficking, and creates a semi-permeable barrier between subcellular compartments.[56] Abnormal levels of cellular cholesterol contribute to several human diseases.[57,58] Therefore, the abundance and distribution of cholesterol in cells, known as cholesterol homeostasis, must be carefully controlled.[56]

Free cholesterol refers to cholesterol in the cell that has not undergone further transformation into cholesterol esters. Mammalian cells obtain free cholesterol from two known sources, *de novo* synthesis or uptake of dietary cholesterol mediated by a low-density lipoprotein (LDL) receptor.[59] Dietary cholesterol is transported in the mammalian bloodstream by lipoprotein particles, and the LDL receptor mediates the endocytosis of cholesterol containing LDL into the cells of peripheral tissues (Figure 3).[60]

Cholesterol synthesis begins with the mevalonate pathway, in which coenzyme A is assembled into isoprenoid intermediates that subsequently combine to form lanosterol. Cholesterol is subsequently synthesized from lanosterol via the Bloch or Kandutsch-Russell pathways (Figure 4). Isoprenoid intermediates are also the substrates of a post-translational modification known as protein prenylation,

which serves to covalently attach isoprenoid groups to C-terminal cysteine residues of proteins.

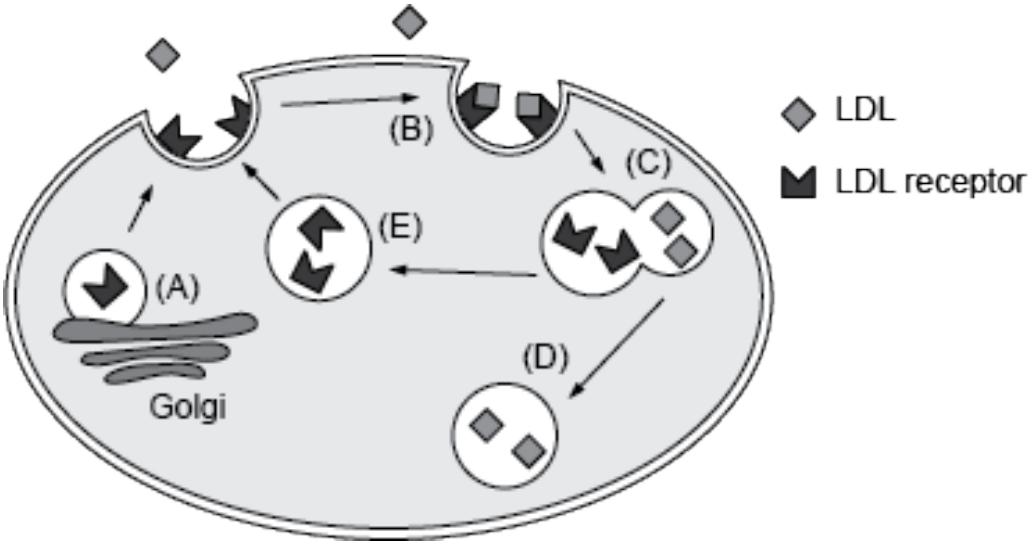

Figure 3. LDL Receptor Mediated Cholesterol Uptake. (A) In the Golgi, LDL receptors are synthesized and incorporated into vesicles. The vesicles fuse with the plasma membrane and cluster within clathrin coated pits. (B) Cholesterol containing circulating LDL binds the LDL receptor and complexes are internalized. (C) Vesicles containing complexes fuse with lysosomes to dissociate the LDL receptor from the cholesterol containing LDL and (D) are subsequently degraded into free cholesterol and amino acids. (E) LDL receptors are recycled to the surface.

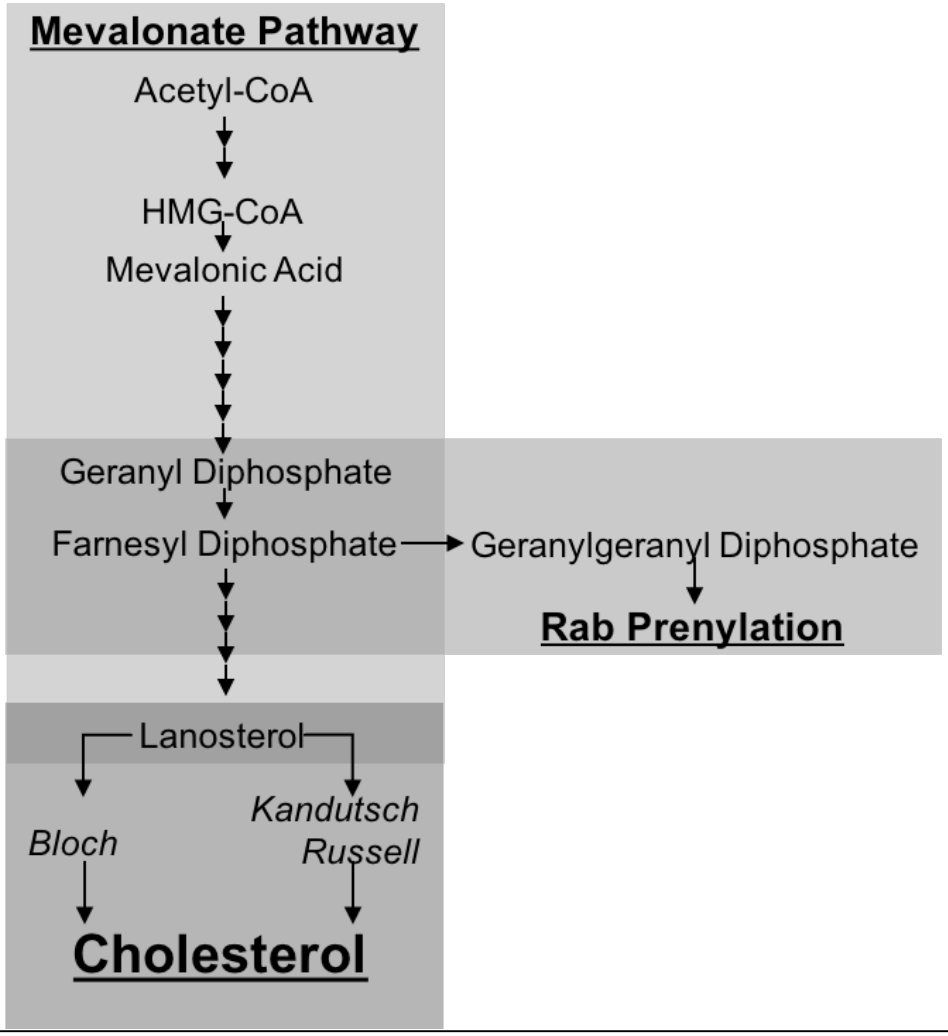

Figure 4. Cholesterol Synthesis. Acetyl CoA is converted to lanosterol through isoprenoid intermediates. Cholesterol is synthesized from lanosterol though the Bloch pathway or the Kandutsch Russell pathway. The mevalonate pathway also branches to produce additional isoprenoids farnesyl pyrophosphate and geranylgeranyl diphosphate, substrates for protein prenylation.

Both cholesterol synthesis and uptake are subject to end-product feedback regulation though of a family of cholesterol sensing transcription factors known as Sterol Regulatory Element Binding Proteins (SREBPs).[61] SREBP-1A, SREBP-1C, and SREBP-2 are membrane bound transcription factors that activate over 30 genes involved in lipid homeostasis, and SREBP-2 selectively activates cholesterol uptake and synthesis genes.[62] SREBPs undergo two subsequent cleavages, the first of which is mediated by free cholesterol, prior to release from the ER and transcriptional activation in the ER.[63]

Prior to storage in lipid droplets or efflux in lipoprotein complexes, free cholesterol is fatty acylated by acyl-CoA:acyltransferase (ACAT) to form cholesterol esters.[63] ACAT activity is responsive to cellular free cholesterol levels. High free cholesterol levels result in allosteric activity of ACAT and storage of cholesterol esters, while low free cholesterol levels decrease cytosolic hydrolysis of cholesterol esters stored in lipid droplets.[57] ACAT1, the first of two homologs of this enzyme, is expressed in all tissues and is responsible for esterifying cholesterol for storage in LDs.[64] ACAT2, the second homolog, expresses predominately in liver and small intestine, and is responsible for esterifying cholesterol prior to packaging in high density lipoprotein (HDL) complexes for reverse cholesterol transport.[65]

Release of excess cholesterol from extrahepatic cells and tissues to HDL, known as reverse cholesterol transport, is critical to prevent cellular cholesterol overloading.[56,66] The first step in cholesterol release occurs through ABC transporter A1, which binds to apolipoprotein A1 in order to facilitate the transfer of cholesterol esters to nascent HDL particles.[67,68] Maturation of HDL particles occurs when the ABC transporter G1 cooperates with the ABC transporter A1 to complete the addition of cellular lipids to the HDL particle prior to its entry into circulation.[56]

As described above, the mevalonate pathway, cholesterol uptake, cholesterol storage, and reverse cholesterol transport are relatively well understood. A current gap in knowledge is the contribution of macrolipophagy to cholesterol homeostasis. Upon completion of macrolipophagy, lysosomal acid lipases release free fatty acids and free cholesterol from the engulfed LDs. Therefore, macrolipophagy may contribute to cholesterol homeostasis, and investigation into this relationship would greatly add to current understanding of cholesterol homeostasis. Chapter 4 describes an investigation into the regulation of the mevalonate pathway by autophagy.

3. Advancing Understanding of Autophagy and Cholesterol Homeostasis

The central hypothesis of this thesis is that autophagy contributes to cholesterol abundance through macrolipophagy and regulation of cholesterol synthesis in aging muscle. Within the scope of this broad hypothesis, the objectives of this thesis are focused on the development of new methods for individual organelle analysis of macrolipophagy, lipid droplet size, and clarification of the role of autophagy in regulating cholesterol synthesis in cells associated with skeletal muscle. Background for these three critical aspects of the hypothesis is provided below.

3A. Capillary Electrophoresis with Laser Induced Fluorescent Detection of Autophagy Organelles

The work described in Chapter 2 reports the first analysis of immunolabeled autophagy organelles isolated from tissues by Capillary Electrophoresis with Laser Induced Fluorescent detection (CE-LIF). This method can be applied to any tissue or cell model of interest, and can be applied to human patient samples in the future. CE-LIF has been previously used by the Arriaga group to determine the surface heterogeneity of individual mitochondria,[69–72] liposomes,[73] nuclei,[74] acidic organelles,[75–77] and autophagy organelles from GFP-LC3 constitutively expressing C2C12 mouse myoblasts.[78] CE-LIF is an analytical technique that separates charged particles under the application of an electric field in submillimeter diameter tubes (known as capillaries). A home-built CE-LIF

instrument (Figure 5) was used to measure the properties of autophagy organelles in Chapter 2.

For organelle analysis, individual organelles are delivered to the capillary via pressure-driven injection and separation is primarily dependent on their surface charge. Individual organelles subsequently exit the capillary and are detected by laser induced fluorescence. CE-LIF is capable of measuring individual organelle electrophoretic mobility, and the low (2 zmol) limit of detection associated with CE-LIF enables the detection of individual fluorescently labeled organelles.[72,78,79] Individual organelles have been labeled for CE-LIF analysis with organelle specific dyes[72,80] and organelle marker-GFP fusion proteins.[78] Both of those labeling strategies have limited applicability in tissues. The work in Chapter 2 represents the first use of antibodies to label organelles for CE-LIF analysis.

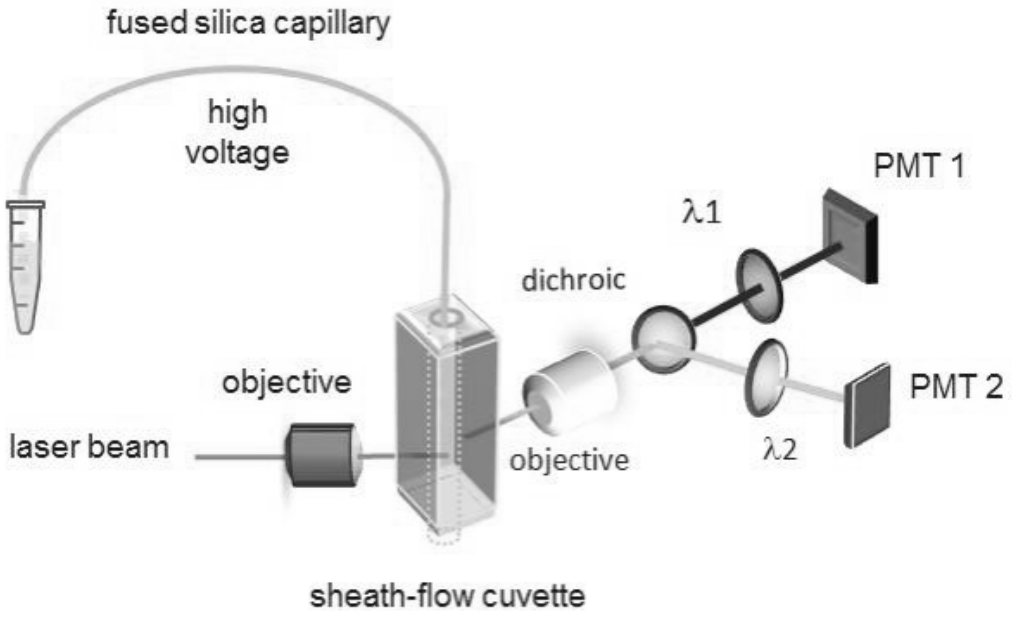

Figure 5. Diagram of Home-Built CE-LIF instrument. Organelles are hydrodynamically injected via siphoning into a fused silica capillary and separated under the application of an electric field. The organelles exit the capillary in a quartz sheath flow cuvette and excitation of the fluorophores labeling the organelles occurs. The emitted photons are focused by an objective and spectrally selected by bandpass filters and detected by photomultiplier tube. The optics configuration shown above includes a dichroic mirror to enable simultaneous detection of two fluorophores.

3B. Nanoparticle Tracking Analysis of Lipid Droplets

The work described in Chapter 3 reports the first measurement of lipid droplet size by Nanoparticle Tracking Analysis. Nanoparticle Tracking Analysis (referred to hereafter as “NTA”) enables measurement of individual particle size in a given sample. Individual particles scatter light from a laser excitation source, and the motion of each particle is individually recorded by a camera and tracked from frame to frame. The diffusion constant of each particle, calculated from two-dimensional Brownian motion, is used to subsequently calculate the particle’s sphere equivalent hydrodynamic radius (Figure 4).

In contrast to ensemble measurement techniques, NTA reveals direct visual information for each particle in the sample, providing a detailed particle distribution description of non-uniform samples. NTA is capable of measuring particles between 20 and 1000nm in diameter has been used previously to determine the size and concentration of biological particles, including exosomes,[81–84] virus particles,[85] and gold nanoparticle protein conjugates.[86] The work in Chapter 3 describes the first application of NTA to measure the size of LDs isolated from murine liver tissue and the first investigation of LD size in a comparative aging study.

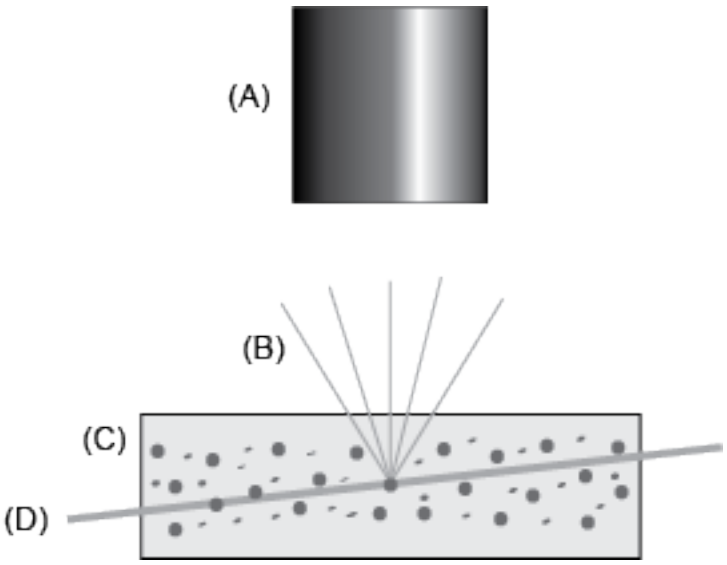

Figure 6. Schematic of NTA Optical Configuration. The 432nm laser (D) illuminates the individual particles undergoing Brownian motion in the measurement chamber (C). The microscope enables a high-frame rate camera (A) to record dispersed light from each particle (B). The particle motion paths are individually tracked by the NTA software, enabling calculation of individual particle size and a particle size distribution is subsequently reported.

3C. Investigation of Mevalonate Pathway Regulation by Autophagy

Chapter 4 reports the first demonstration of autophagy regulating the mevalonate pathway and introduces a new avenue for investigation into the basic mechanisms governing the relationship between cholesterol homeostasis and autophagy. Since the seminal discovery of the ability of autophagy machinery to mobilize neutral lipids stored in liver lipid droplets, known as macrolipophagy,[7] a role for the mevalonate pathway in the regulation of autophagy has started to surface.

Several studies have linked the mevalonate pathway to the regulation of autophagy. The mevalonate pathway is known to control autophagy through Rab prenylation, which is required for autophagy in several model systems.[87–90] Free cholesterol is obtained from de novo synthesis via the mevalonate pathway and LDL receptor mediated uptake.[7–9] Autophagy (specifically macrolipophagy of lipid droplets) is likely a third source of cholesterol, working together with the mevalonate and uptake pathways to regulate cholesterol levels.

Despite the above advancements in knowledge, the regulation of cholesterol synthesis by autophagy has not been investigated, Prior to the work in Chapter 4, this relationship was completely unexplored in cells associated with skeletal muscle. The experiments described in Chapter 4 followed the observation that knockdown of autophagy-related gene ATG7 resulted in an increased free

cholesterol level and incorporation of prenyl modifications in L6 rat myoblasts. The effect of ATG7 knockdown on the regulation of the mevalonate pathway was subsequently investigated, resulting in a new working model for autophagy in the regulation of the mevalonate pathway.

The model is summarized as follows. Free cholesterol has a steady state pool maintained by uptake, synthesis through the mevalonate pathway and autophagy of lipid droplets. Autophagy inhibition results in a higher steady state pool of free cholesterol, and accumulation of proteins involved in the mevalonate pathway, fatty acid synthesis, and nucleotide synthesis. The increased free cholesterol level subsequently triggers negative feedback of cholesterol synthesis genes in order to reduce overall flux though the mevalonate pathway. In summary, the data suggest that autophagy inhibition decreases mevalonate pathway flux. We believe the working model presented in Chapter 4 serves as a framework for future investigation into the contribution of autophagy to cholesterol homeostasis.

Chapter 2: Capillary Electrophoresis with Laser Induced Fluorescent Detection of Individual Autophagy Organelles Isolated From Liver Tissue

Heather M. Brown (Grundhofer) performed quantitative PCR gene expression analysis (see Appendix 1, Supplementary information to this Chapter). Dr. M. Kyba from the Department of Pediatrics and Dr. D. Lowe from the Department of Physiology at the University of Minnesota provided mice for the autophagy organelle isolation. We thank Dr. N. Mizushima from the University of Tokyo for the generous gift of ATG5 (-/-) and (+/+) MEF cells, provided to us by Dr. D. Kim from the Department of Biochemistry, Molecular Biology, and Biophysics at the University of Minnesota. This work was supported by the National Institutes of Health (Grants RO1-AG020866, T32-GM008700 and T32-AG029796).

Summary

Macroautophagy is a cellular degradation process responsible for the clearance of excess intracellular cargo. Existing methods for bulk quantification of autophagy rely on organelle markers that bind to multiple autophagy organelle types, making it difficult to tease apart the subcellular mechanisms implicated in autophagy dysfunction in liver and other pathologies. To address this issue, methods based on individual organelle measurements are needed. Capillary electrophoresis with laser induced fluorescent detection (CE-LIF) was previously used to count and determine properties of individual autophagy organelles isolated from an LC3-GFP expressing cell line, but has never been used on autophagy organelles originating from a tissue sample. Here, we used DyLight488-labeled anti-LC3 antibodies to label endogenous LC3 present on organelles isolated from murine liver tissue prior to CE-LIF analysis. We evaluated the ability of this method to detect changes in a known model system of altered autophagy, as well as confirmed the specificity and reproducibility of the antibody in the labeling of autophagy organelles from liver tissue. This is both the first demonstration of CE-LIF to analyze individual organelles labeled with fluorophore-conjugated antibodies, and the first application of individual organelle CE-LIF to measure the properties of autophagy organelles isolated from tissue. The observations described here demonstrate that CE-LIF of immunolabeled autophagy organelles is a powerful technique useful to investigate the complexity of autophagy in any tissue sample of interest.

Introduction

Macroautophagy (referred hereafter as autophagy) is cellular degradation pathway that is critical in the maintenance of cellular homeostasis.[11,91,92] Loss of autophagy function is implicated in aging[37,93] and numerous liver pathologies, including liver cancer, non-alcoholic and alcoholic fatty liver disease, and viral hepatitis.[94,95] Because these conditions decrease health span, there is a pressing need for reliable and quantitative measurements of autophagy in tissue samples. While there are existing methods for quantifying bulk markers present on autophagy organelles, a method based on individual organelle measurements would reduce bias, by reporting across distributions of properties of organelles in the multiple organelle types present in a given tissue sample.

Current methods for monitoring autophagy are western blot, transmission electron microscopy (TEM), fluorescent microscopy, and flow cytometry.[23] The most common is a western blot to monitor the formation of LC3-II, but this method is notorious for incorrect identification of autophagy induction[23–25]. Also, it is impossible to determine from a western blot whether an increase in LC3-II is indicative of more organelles containing that marker, or an increase in marker density on the surface of existing organelles. TEM enables visualization of autophagy organelle structures[26–28], but it requires an expert eye for their correct identification.[31] Individual autophagy organelles can be visualized with fluorescent microscopy,[29,30] but counting of individual LC3-II is not high-

throughput and requires colocalization experiments to determine which autophagy organelles are present. Flow cytometry is a well-defined method for characterizing heterogeneity among individual cells or particles, but its use in detecting individual organelles has been somewhat limited due to high limits of detection. Individual cell[32–34] flow cytometry autophagy assays have been reported, but these methods are contingent on the overexpression of fluorophore-LC3 fusion proteins, which can form aggregates independent of autophagy organelle formation[96] and cannot describe how the reporter distributes among the various autophagy organelle types. Fluorescently labeled primary antibodies have been used to detect individual mitochondria by flow cytometry[97] and capillary cytometry,[79] which is a form of flow cytometry, but these methods have not yet been applied to autophagy organelles and report only individual organelle fluorescence intensities. Other reports have applied flow cytometry to measure individual autophagy organelles also labeled with fluorophore-LC3 conjugates,[33] acidotropic chemical probes,[35] and fluorescently labeled secondary antibodies.[36] In addition to the drawback associated with GFP-fluorophore fusion proteins, acidotropic probes only label acidic autophagy organelles that have fused with lysosomes. Due to the high limit of detection associated with flow cytometry, detection of immunolabeled autophagy organelles has been limited to those labeled with secondary antibodies.[24] Methods based on immunolabeling with primary antibodies for labeling of individual autophagy organelle analysis have not been reported so far.

Capillary electrophoresis with laser-induced fluorescent detection (CE-LIF) has been used to monitor bulk conversion of GFP-LC3-I to GFP-LC3-II in cell extracts[98] as well as individual GFP-LC3-II positive autophagy organelles isolated from C2C12 mouse myoblasts.[78] In addition to autophagy organelles, CE-LIF has been used extensively to determine the numbers and properties of individual mitochondria,[99] liposomes,[73] nuclei[74] and acidic organelles.[100] Advantages of CE-LIF include low limits of detection, which enables the detection of individual fluorescently labeled organelles and the ability to measure individual organelle electrophoretic mobility which enables the investigation of surface heterogeneity among a population of organelles.[73,74,78,99,100]

This paper introduces a new method for monitoring autophagy in tissues using primary antibody labeling and CE-LIF. This technique has been used to analyze immunolabeled peptide hormones,[101] proteins,[102–104] and bacteria,[105] but there has been no report thus far of the application of CE-LIF to analyze immunolabeled organelles. Fluorophore-conjugated primary antibodies have not been used to label individual organelles for CE-LIF analysis, and this technique is capable of measuring the electrophoretic mobility of individual autophagy organelles. In this report, we describe a method based on labeling of LC3-II with a primary antibody. We first used an established biological model of disrupted autophagy to investigate the sensitivity of the method to changes in autophagy function. Then, we applied the method to quantify properties of individual

autophagy organelles isolated from murine liver tissues. Future applications of CE-LIF combined with primary antibody labeling could be used to examine autophagy organelles from tissues obtained from animal models of liver disorders and aging, as well as human tissue biopsies.

Experimental Section

Materials, reagents, buffers, and solutions. Sucrose, fluorescein, 4-(2-hydroxyethyl)-1-piperazineethanesulfonic acid (HEPES), mannitol, ethaminetetraacetic acid (EDTA), poly(vinyl alcohol) (99%+ hydrated, molecular weight 89,000-980,000), dimethyl sulfoxide (DMSO), ethylene-bis(oxyethylenenitrilo)tetraacetic acid (EGTA) were obtained from Sigma-Aldrich (St. Louis, MO). Tris base, 4-morpholine-propanesulfonic acid (MOPs), sodium chloride, 10,000 units penicillin, 10mg streptomycin/ml, Dulbecco's Modified Eagle Medium (DMEM) high glucose solution, fetal bovine serum, 0.5% trypsin-EDTA (10× solution), AlignFlow flow cytometry beads (2.5μm), and 200mM L-glutamine solution (1000×) were obtained from Thermo Fisher Scientific (Waltham, MA). Phosphate buffered saline (PBS, 10× concentration, 1.37M NaCl, 27mM KCl, 80mM Na_2HPO_4, and 20mM KH_2PO_4, pH 7.4) was obtained from Bio-Rad (Hercules, CA). A polyclonal Dylight488 conjugated rabbit anti-LC3 antibody, was obtained from Novus Biologicals (Littleton, CO). Dylight-488 conjugated rabbit isotype control was obtained from Abcam (Cambridge, UK).

Water was purified with a Millipore Synergy UV system (18.2mΩ/cm, Bedford, MA). Cell homogenization buffer consisted of 70mM sucrose, 215mM mannitol, 4.31mM HEPES, and 4.94mM EDTA, pH 7.4. CE buffer consisted of 250mM Sucrose, 10mM HEPES, pH 7.4. PBS was diluted 1:10 in purified water.

Autophagy organelle isolation from cultured cells and subsequent antibody labeling. ATG5 (-/-) and (+/+) mouse embryonic fibroblasts (MEFs) were a generous gift of Dr. Noboru Mizushima (The University of Toyko, Japan). MEFs were maintained at 37°C, 5% CO_2 in high glucose DMEM supplemented with 10% fetal bovine serum, 200μM glutamine, 1000 units penicillin, and 10μg/ml streptomycin. For propagation, cells were lifted with 0.5% Trypsin-EDTA in PBS and split 1:20 (v/v) into new flasks every 48 hours. For autophagy organelle isolation, MEFs were expanded into two 75cm flasks 48 hours prior to experiment day. Cells were harvested, resuspended in 1ml cell homogenization buffer and disrupted in an ice cold nitrogen cavitation chamber (Parr Instrument Co., Moline, IL). Cells were kept in the chamber at 600psi for 15 minutes prior to depressurization and release. All subsequent steps were performed on ice or at 4°C. The cell lysate was collected in a 50ml conical tube and centrifuged at 600g for 10 minutes to pellet unbroken cells and nuclei. The supernatant (post-nuclear fraction) was removed to a clean microcentrifuge tube and spun at 10,000g for 10 minutes to pellet autophagy organelles. The organelles were resuspended in 100μl CE buffer and incubated with 300nM DyLight488 anti-LC3 antibody for 1

hour on a microcentrifuge tube rotator in a 4°C cold room. The labeled autophagy organelles were centrifuged at 10,000g for 10 minutes to remove unbound antibody and were resuspended in 200ul CE buffer prior to CE-LIF analysis. Protein content of the organelle suspensions was measured by the Pierce BCA Protein Assay Kit (Thermo Fisher Scientific) in accordance with the manufacturer's instructions.

Autophagy organelle isolation from liver and subsequent antibody labeling. All mice were housed in a designated clean facility and treated in accordance with protocols approved by the Institutional Animal Care and Use Committee at the University of Minnesota. Autophagy organelles were prepared from the livers of male and female adult mice, using a procedure adapted from a published mitochondrial isolation method.[106] Each CE-LIF experiment was performed on autophagy organelles isolated from a single mouse liver. The mouse was euthanized and the liver was removed and placed into 10ml liver homogenization buffer (10mM Tris, 1mM EGTA, 10mM MOPS, 200mM Sucrose) on ice. The liver remained on ice or at 4°C unless otherwise noted. The liver was moved to a small petri dish and sliced into 1mm pieces using a flat razor blade. The liver pieces were rinsed with liver homogenization buffer until free of blood and resuspended in fresh liver homogenization buffer at 1:5 (w/v) and transferred to a 15ml glass homogenization tube (Wheaton, Millville, NJ). The liver suspension was homogenized in a tight-fitting motor driven Teflon pestle (Wheaton) operated

at 2200rpm for four strokes. The homogenate was centrifuged at 600g for 10 minutes and the cloudy supernatant (post-nuclear fraction), containing autophagy organelles, was transferred to clean 1mL microcentrifuge tubes. The post nuclear fractions were centrifuged at 10,000g for 10 minutes to pellet autophagy organelles. Each pellet was resuspended in in 500µl CE buffer and combined into a 15ml conical tube. This step served to concentrate the sample prior to organelle labeling.

For antibody labeling, the organelle suspension was separated in to 100ul aliquots and incubated with DyLight488 labeled anti-LC3 antibody or DyLight488 isotype control at concentrations ranging from 5-300nM for 1 hour on a microcentrifuge tube rotator in the 4°C cold room. The labeled autophagy organelles were centrifuged at 10,000g for 10 minutes to remove unbound antibody and were resuspended in 100µl CE buffer, and diluted 1:50 (v/v) in CE-buffer prior to CE-LIF analysis or diluted 1:2500 (v/v) in CE buffer prior to capillary cytometry analysis.

Instrumentation and Alignment. A previously described, home-built instrument[73] with post capillary sheath flow LIF detection was used to determine numbers of autophagy organelles, DyLight488 intensity of each organelle, and electrophoretic mobility of each organelle. To align the optics for consistent fluorescent response, the optics were adjusted until the fluorescence intensities

of individual alignment beads (AlignFlow, Molecular Probes, Thermo Fisher Scientific) maintained a relative standard deviation within the manufacturers specifications (~30%).[78,79] Excitation of all samples resulted from a 488nm 12mW argon-ion laser (JDS Uniphase, San Jose, CA). Dylight488 emission was selected by a 525±25nm band pass filter (Omega Optical, Brattleboro, VT). Emitted photons were detected by photomultiplier tube (R1477, Hamamatsu, Bridgewater, NJ) and the output was digitized at 200hz with a NiDaq I/O board (PCI-MIO-16XE-50, National Instruments, Austin, TX), collected with customized LabVIEW 5.1 software (National Instruments) and stored as binary files.

For CE-LIF analysis, a sample volume containing organelles was introduced into a 30μm inner-diameter fused silica glass capillary (Polymicro, Phoenix AZ) via siphoning (104cm height, 10s injection). Capillaries were coated in-house with poly-vinyl alcohol to decrease electro osmotic flow and prevent absorption of organelles into capillary walls.[69] Capillary electrophoresis separations were performed at -300 V/cm for 30 minutes for liver samples and 40 minutes for MEF samples.

For capillary cytometry analysis, organelles were passed through 30μM inner-diameter uncoated fused silica glass capillary (Polymicro) at a rate of 20nL/min maintained by the application of external pressure (10 ± 1kPA) provided by a nitrogen pressurized Erlenmeyer flask, as described previously.[79] Unlike CE-LIF,

capillary cytometry does not provide the electrophoretic mobility of individual organelles. Constant introduction of organelles into the capillary by application of external pressure allows a larger number of organelles to be analyzed in a shorter time than CE-LIF analysis. Thus, capillary cytometry was used to evaluate multiple antibody concentrations on a single day, as our measures of antibody labeling were only dependent on event intensity. Capillary cytometry analyses were performed for 20 minutes.

To eliminate carryover between samples in both CE-LIF and capillary cytometry experiments, methanol was passed through the capillary for 5 minutes to remove biological material and CE buffer was passed through the capillary for 5 minutes to re-equilibrate the capillary. At the end of each experiment, methanol was passed the capillary for 5 minutes to remove biological material and air was passed through the capillary to dry it prior to storage.

Data analysis. Peak time, peak width, and peak intensity of all organelle events was obtained as previously described from the binary files using IgorPro software (WaveMetrics, Oswego, Oregon), with in-house written algorithms.[100] The program selected peaks with signal intensities higher than a given threshold. As previously reported,[100,107] the threshold, expressed as multiple of the standard deviation of the background, was adjusted so that no more than 5% of detected events were false positives. The threshold selection was as follows: Initially, the

threshold was set to 3 times the standard deviation of the background. The electropherogram (CE-LIF) or flowgram (capillary cytometry) was subsequently divided into “premigration” and “collection” windows. Only false positives are detected in the premigration window, while both false and true positives are detected in the collection window. The threshold was adjusted until the rate of false (events/s) was 5% of the rate of total events (events/s) detected in the collection window. After selection of a final threshold, the total number of organelle events observed in the collection window was corrected for false positive rate in the premigration window using the following equation:

Equation 1 $$O_c = O_T - \left(\frac{N}{P}\right) W$$

Where O_T is the total number of organelles observed in the collection window, N is the number of false positive events in the premigration window, P is the length of the premigration window in seconds, and W is the length of the collection window in seconds.

To account for variations in the amount of protein in organelles prepared from ATG5 (-/-) MEFs and ATG5 (+/+) MEFs, peak numbers were normalized to the nanograms of protein injected, as described previously.[78] The calculated electrophoretic mobilities of individual organelles are affected by run-to-run fluctuations. Thus, a fluorescein standard was injected with each organelle

separation, and the previously reported (-3.0+/-0.1 x 10^{-4} cm^2 V^{-1} s^{-1})[108] and observed mobilities of fluorescein were used to correct the mobilities of observed organelle events, as described before.[78] To eliminate day-to-day variations in detector sensitivity, each experiment was performed on a single day.

The coupling of fluorophores to antibodies is variable and the Fluorophore/Protein (F/P) molar ratios can differ between antibody lots. To account for variations in between DyLight488 labeled anti-LC3 and DyLight488 labeled isotype control antibodies compared in a single experiment, intensity values were normalized to the F/P ratio. The corresponding F/P ratio for each antibody used was calculated as

Equation 2 $$\frac{F}{P} = \frac{A_{max}DyLight488}{\varepsilon' DyLight488 \times [I_g G]}$$

Where A_{max}Dylight488 is the absorbance of the dye measured at its wavelength maximum (493nm), ε' Dylight 488 is the extinction coefficient of the dye (70,000$M^{-1}cm^{-1}$), and [IgG] is the concentration of the antibody, measured from absorbance at 280nm, corrected for the contribution of DyLight488. The normalized intensity values, $I_{N,}$ were corrected to the F/P ratio using the following equation:

Equation 3 $$I_N = \begin{cases} I \times \frac{F2/P2}{F1/P1}, & \frac{F2}{P2} < \frac{F1}{P1} \\ I \times \frac{F1/P1}{F2/P2}, & \frac{F1}{P1} > \frac{F2}{P2} \end{cases}$$

Where I represents the DyLight488 intensity measured in arbitrary units (A.U), and the two antibodies used in the experiment have F/P ratios F1/P1 and F2/P2.

Histograms and Quantile-Quantile (QQ) plots were used to compare distributions of organelle electrophoretic mobilities and DyLight488 intensities. QQ plots are created by plotting the 5th through 95th percentiles from two sample distributions. If the two distributions are similar, their QQ plot approaches an X=Y line. Three technical replicate separations of autophagy organelles labeled with DyLight 488 anti-LC3 and Dylight488 isotype control were performed in alternating order on a single day over a period of 6 hours. For visual evaluation of distribution reproducibility amongst technical replicates, the QQ plot was produced by graphing the 5th through 95th percentiles of each individual replicate distribution vs the 5th through 95th percentile of the pooled distribution. Linear regression also was used for quantitative evaluation of distribution reproducibility amongst technical replicates. Confidence intervals were constructed for hypothesis testing.

Statistical Overlap Theory (SOT) was applied to predict the overlap of individual events[109] and determine whether the number of observed peaks was an

adequate representation of the number of organelles present in the sample. This technique was previously used to predict overlap of individual mitochondria[79,80,110] and autophagy-related organelles.[78] Briefly, the peaks in each electropherogram or flowgram were partitioned into bins. A maximum number of peaks allowed per bin, $m_{critical}$, was calculated based on the bin length (X) and the standard deviation of peak widths in the bin (σ).[80] If the number of observed peaks, p, exceeds $m_{critical}$, then overlap precluded an accurate count of events. If p is less than $m_{critical}$, then the peaks in the bin have a 90% probability of falling within a 95% confidence interval of representing a single event. In bins where p exceeded $m_{critical}$, we used $m_{critical}$ as a conservative measure of the number of organelle events present in that bin. As there is no relationship between event time and event intensity, events from bins in large overlap were eliminated prior to comparison of intensity distributions. As electrophoretic mobility is calculated from event time, we were unable to remove events from bins in large overlap prior to comparison of electrophoretic mobility distributions.

Safety Information. Biosafety level 1 procedures were followed when working with MEFs and murine liver tissue. Appropriate PPE included a lab coat, safety glasses, and gloves. All biological waste was treated with 10% bleach prior to disposal in the laboratory sink with copious amounts of water.

Results and Discussion

Analysis of individual organelles labeled with anti-LC3 antibodies. Most methods to monitor autophagy rely on the use of anti-LC3 antibodies for the measurement of LC3-II, which is the lipidated form of microtubule-associated protein 1A/1B-light chain 3 (LC3), which is required for the formation of mammalian autophagosomes.[19] Similarly, a method for immunolabeling endogenous LC3 present on individual autophagy organelles would enable CE-LIF of individual autophagy organelles possible in any tissue or cell line that is amenable to organelle isolation, making it possible to compare the properties of LC3 positive individual organelles.

The first focus of this report was to determine the suitability of antibodies as organelle labels for CE-LIF analysis, and to detect changes in distributions of individual organelle electrophoretic mobility and DyLight488 anti-LC3 levels in a model system of altered autophagy. Prior work demonstrated the use of CE-LIF to measure the numbers of GFP-LC3 containing autophagy organelles and determine their properties[78]. The major limitation of such method was its reliance on overexpression of LC3-GFP conjugates, which make the technique not applicable to tissues.

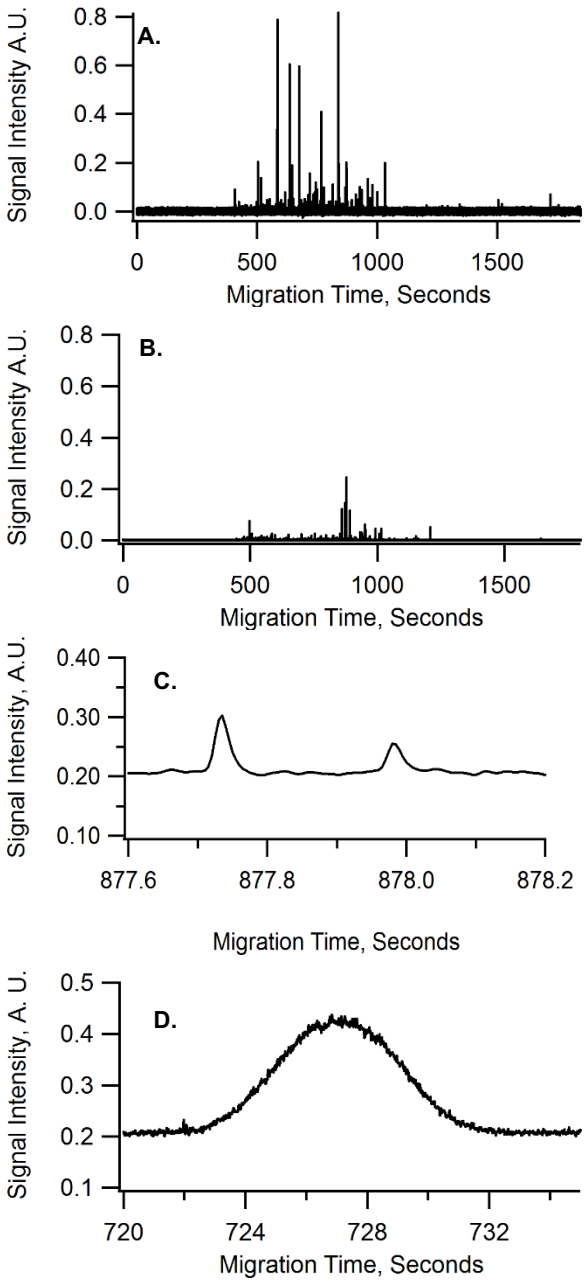

Figure 1. Representative electropherograms of individual autophagy organelles. (A) Autophagy organelles labeled with 50nM DyLight-488 anti-LC3, n=208 peaks. (B) Organelle fraction labeled with 50nM DyLight488 isotype control, n=30 peaks. Samples are from murine mouse liver. Organelles appeared as individual peaks after a premigration window of ~ 400 seconds. Threshold was set to 4σ. Buffer was 250mM Sucrose, 10mM HEPES pH 7.2. Excitation was from a 12-mW 488-nm argon-ion laser. Fluorescence detection, 525df25 band pass filter. Hydrodynamic injection, 10 seconds, 11.11 kPa pressure drop. Capillary ID, 30μm. (C) Expansion of Part (A) showing individual organelle peaks. (D). Fluorescein peak (9.6-s wide), resulting from co-injection of internal standard, processed after removal of individual peaks from electropherogram using a median filter.

Labeling of organelle preparation from mouse liver with DyLight488 anti-LC3, followed by CE-LIF analysis, showed that individual organelles appeared in electropherograms as individual peaks (Figure 1A) with their width determined by the time the organelle was crossed the laser beam in the LIF detector. The average peak width (15 ± 3ms; avg +/- std deviation, n=819 peaks) is compatible with the travel time through the laser beam and in agreement with our previous report on the analysis of GFP-LC3 labeled autophagy organelles (peak width 36 ± 16ms; avg +/- std deviation, n=12,567 peaks).[25] That individual autophagy organelles appear as narrow peaks (Figure 1C) when labeled with DyLight488 anti-LC3, is consistent with the fact that such label is bound to a particle and not free in solution. Because the DyLight488 anti-LC3 antibody also binds to LC3-I free in the cytosol, the antibody-LC3 complex could have been detected as a wide peak, similar to what we observe for fluorescein, which was co-injected with the organelle sample as a standard (Figure 1D). It is worth mentioning that a band for DyLight488 labeled LC3-I was not detected, because cytosolic proteins are removed in the organelle isolation procedure. Thus, the signal intensity of each peak event refers to the amount of DyLight488 present on an individual organelle.

On the other hand, not all organelles detected correspond to autophagy organelles. Antibodies may display non-specific binding to different epitopes other than the one it was raised against.[111] To correct for non-specific binding,

isotype controls do not recognize the epitope of interest have been used in flow cytometry.[112] In this study, we selected a DyLight488-labeled isotype as control for non-specific binding. When the organelle sample was treated with DyLight488 isotype antibody that does not bind to LC3, a few events were detected (30 events), suggesting that some organelles are labeled due to non-specific binding (Figure 1B). This is a small fraction relative to labeling with anti-LC3 antibodies (~ 14%) that can be easily corrected through data processing as described below.

A unique aspect of the analysis of individual autophagy organelles by CE-LIF is the determination of their electrophoretic mobilities. As described below each organelle has a unique electrophoretic mobility, which is heavily influenced by its surface composition,[73] and results in a different migration time (Figure 1A). Thus, the results shown indicate that antibody labeling of autophagy organelles enables measurement not only of the number of organelles, and their individual fluorescence intensities resulting from immunolabeling, but also their electrophoretic mobilities.

To determine if this new method could detect differences in the properties of autophagy organelles in a well-characterized biological system, we analyzed cells deficient in autophagy (ATG5 (-/-) MEFs) and an appropriate control (ATG5 (+/+) MEFs). LC3 is recruited to the autophagosome membrane in an ATG5 dependent manner[16,113], and cells deficient in ATG5 will have a decrease in

autophagosome formation. To validate this cell system, western blot analysis indicated that ATG5 (-/-) cells ATG5 protein levels were below the limit of detection of the method (~15 fg, Figure S1). Quantitative reverse-transcriptase polymerase-chain reaction (q-RT-PCR) indicated that ATG5 (-/-) cells had a 99.960 +/- 0.001% (mean ± SEM) reduction in ATG5 gene expression (Figure S1). CE-LIF analysis of organelles isolated from ATG5 (-/-) MEFs and ATG5 (+/+) MEFs and labeled with DyLight488 anti-LC3 provided: (1) the number of organelles in the sample (2) the distribution of organelle intensities and (3) the distributions of organelle electrophoretic mobilities.

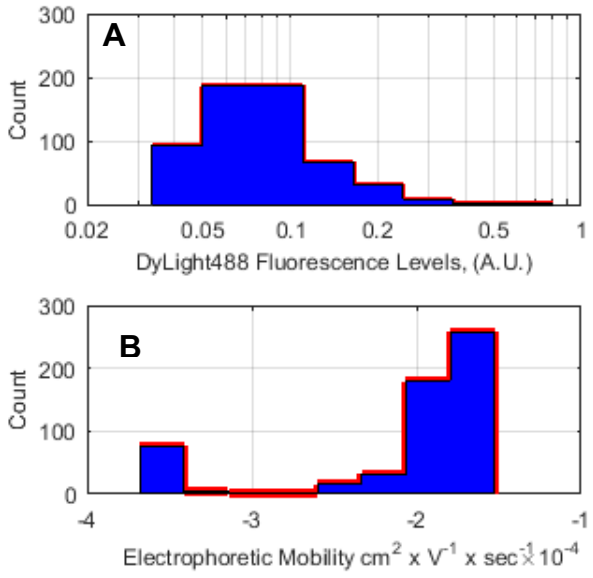

Figure 2. Autophagy organelle DyLight488 intensity and electrophoretic mobility distributions from ATG5 (+/+) MEFs. (A). Intensity distribution from ATG5 (+/+) MEFs, n=745 events. (B) Electrophoretic mobility distribution from ATG5 (+/+) MEFs, n=745 events. Data were acquired using conditions described in Figure 1. Data from ATG (-/-) MEFs were subtracted bin by bin in both distributions.

Application of the statistical overlap theory (SOT) to the separations of organelles isolated from ATG5 (+/+) or (-/-) MEFs (Figure S2), indicated that it was feasible to estimate organelle counts in each sample. As expected, samples from ATG5 (+/+) cells had a higher number of total autophagy organelles than ATG5 (-/-) cells (745 and 22 events, respectively) when normalized to sample protein content. Correction for false positive rate (Equation 1), resulted in 729 organelles for ATG5 (+/+) and 0 for ATG5 (-/-) cells. This is in agreement with previously reported phenotype of ATG5 (-/-) mouse embryonic stem cells that have impaired autophagosome formation, and an approximate 2.5 fold decrease in LC3-II formation.[114]

Histograms were used to visualize distributions of individual organelle intensities (Figure 2A) and individual organelle electrophoretic mobilities (Figure 2B) from ATG5 (+/+) MEFs. As the corrected number of autophagy organelles in ATG5 (-/-) MEFs was 0, the distribution of events observed in that sample (false positives), were subtracted from the ATG5 (+/+) the MEFs distributions. The range in the intensity distribution (Figure 2A) illustrates the heterogeneity in LC3-II contents in autophagy organelles. Similarly, the distribution of electrophoretic mobilities is representative of the surface composition of autophagy organelles, primarily determined by the proteins and lipids that are present in their surface.[78] Thus, the CE-LIF results of the analysis of organelles isolated from ATG (+/+)

MEFs and ATG5 (-/-) MEFs provide clear differences in heterogeneity of a biologically relevant model system of altered autophagy.

Immunolabeling specificity toward individual organelles isolated from murine liver tissue. Next, we investigated the effect of non-specific labeling on the CE-LIF analysis of autophagy organelles isolated from murine liver tissue. Organelles were labeled with 300nM DyLight488-conjugated anti-LC3 antibody or DyLight488-conjugated isotype control prior to CE-LIF analysis. This relatively high concentration of antibodies ensured detection of a sufficiently high number of events for each of the antibodies. After normalizing for amount of protein contents in each sample, correcting for false positives (Equation 1), adjusting peak intensities for F/P ratios (Equations 2 and 3), and confirming that peak overlap was not an issue (Figure S3), the numbers of detected events were 773 and 726 in the samples treated with DyLight488-conjugated anti-LC3 antibody and the DyLight 488-conjugated isotype control, respectively. These high numbers of events detected, made possible comparisons of individual organelle intensity and electrophoretic mobility distributions.

The distributions of event intensities were compared using a QQ plot (Figure 3A). The quantiles were represented as markers at 5^{th}, 10^{th}, 15^{th}, … percentiles. As expected, the general trend was positive deviation from the diagonal, indicating that non-specific binding events are overall less intense than organelles labeled

with the specific antibody. Furthermore, the clear deviation from the diagonal for events falling in the 65th-100th percentiles suggest that such events represent specific binding of the DyLight488 anti-LC3 antibody.

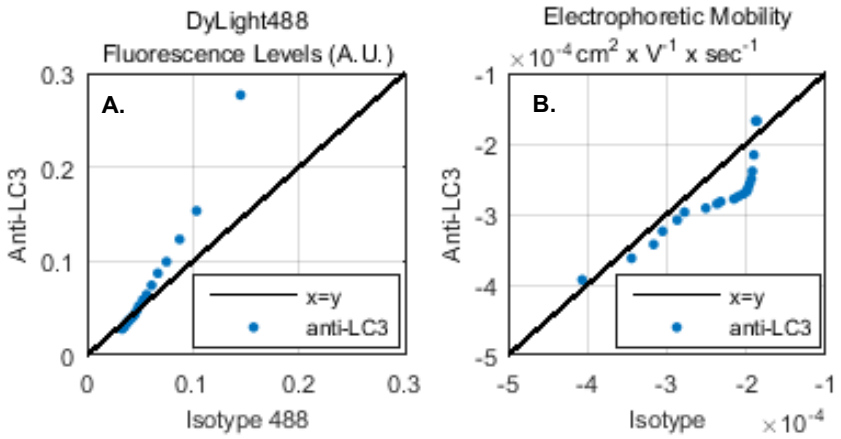

Figure 3. **Comparison of intensity and electrophoretic mobility distributions of organelles labeled with DyLight488 Anti-LC3 or Isotype control.** (A) QQ plot of individual organelle DyLight488 fluorescent intensity distributions. (B) QQ plot of individual organelle electrophoretic mobility distributions. DyLight488 conjugated anti-LC3 antibody (y-axis) versus DyLight488 conjugated isotype control (x-axis). Markers represent the 5th-95th percentiles. Data were acquired using conditions described in Figure1.

Because the specific binding of the DyLight488 anti-LC3 and the non-specific binding of the DyLight488 isotype represent different organelle populations, we also anticipated different electrophoretic mobility distributions of the detected individual events. The organelles detected due to the specific binding of the DyLight488 anti-LC3 are associated with the autophagy process and include other organelles such as phagophores and autolysosomes that have LC3-II in their membranes.[14,25,115] In contrast, DyLight488 isotype labeling does not represent anyparticular organelle type. Indeed, the QQ of electrophoretic mobility distributions suggested that the electrophoretic mobility (i.e. surface charge density) of the autophagy organelles is predominantly more negative than that non-specific binding events over the 10^{th}- 90^{th} percentile range ((Figure 3B). Because antibodies are likely protonated (positive charge) during the separation, (isoelectric points of antibodies are typically between 8 and 11[116] and the pH of the separation buffer was 7.4), binding of DyLight488 anti-LC3 antibodies to autophagy organelles cannot explain the unique negative surface charge density we observed for such organelles.

In summary, comparisons of individual event intensities and electrophoretic mobilities distributions confirm that DyLight488 anti-LC3 antibody and the DyLight488 isotype represent different organelle populations. However, the high number of non-specific binding events required optimization of the antibody concentrations used in labeling.

Titration of antibody concentration to maximize differences between anti-LC3 and isotype labeled organelles. The polyclonal anti-LC3 antibody used here (undefined K_D), which is the most commonly used antibody for LC3 detection, required empirical optimization. Capillary cytometry was used to investigate differences in numbers and intensity of individual organelles labeled with four different DyLight488-conjugated anti-LC3 antibody and Dylight488-conjugated isotype control concentrations. Although capillary cytometry does not provide electrophoretic mobility values, it reduces the analysis time per sample from 30-40 min to 20 min, which made possible analysis of organelles labeled with 5nM, 50nM, 150nM, and 300nM DyLight488-conjugated anti-LC3 antibody or DyLight488-conjugated isotype control on one day.

The corrected number of organelle events (c.f. Equations 1, 2 and 3) tended to increase with anti-LC3 concentration, but remained relatively low among the various isotype concentrations tested (Figure 4A). Except for 5 nM, the number of observed organelle events were higher for labeling with the anti-LC3 antibody than that of labeling with the isotype control suggesting that any of these concentrations could be adequate for subsequent experiments. Upon closer examination, it became apparent that numbers of observed events at 150nM and 300nM anti-LC3 concentrations displayed peak overlap (Figure S4). Furthermore, the number of non-specific binding events are relatively significant when labeling with antibodies at the high end of the concentration range (see

previous subsection) and there may be unwanted formation of antibody aggregates. Thus, although labeling with a high concentration of anti-LC3 antibody would favor detection of autophagy organelles with low LC3-II copies on their surface, the comparison of the number of organelles favored selection of 50nM anti-LC3 antibody and isotype concentrations in subsequent studies.

Comparison of intensities of organelles labeled with the anti-LC3 and isotype control at the concentrations described above also suggested that 50nM antibody concentrations were adequate. The differences in median intensities of individual organelles labeled with the anti-LC3 and the isotype control show that the maximum difference is at this concentration (Figure 4B). QQ plots comparing their respective intensity distributions also show the same (Figure 4C and S4). It is important to note that such plots show no difference for 5nM antibody concentrations (Figure S4E) and that the plots become unreliable when there is significant peak overlap as determined by SOT (Figures S4C, S4D, S4F, and S4G). Thus, it is clear that a 50nM antibody concentration results in a large positive shift in overall intensity distribution between the anti-LC3 antibody and isotype control (Figure 4C). Thus, comparisons of event numbers and individual peak intensities suggest that 50nM was the most suitable antibody concentration for evaluating specific binding of the DyLight488-conjugated anti LC3 antibody.

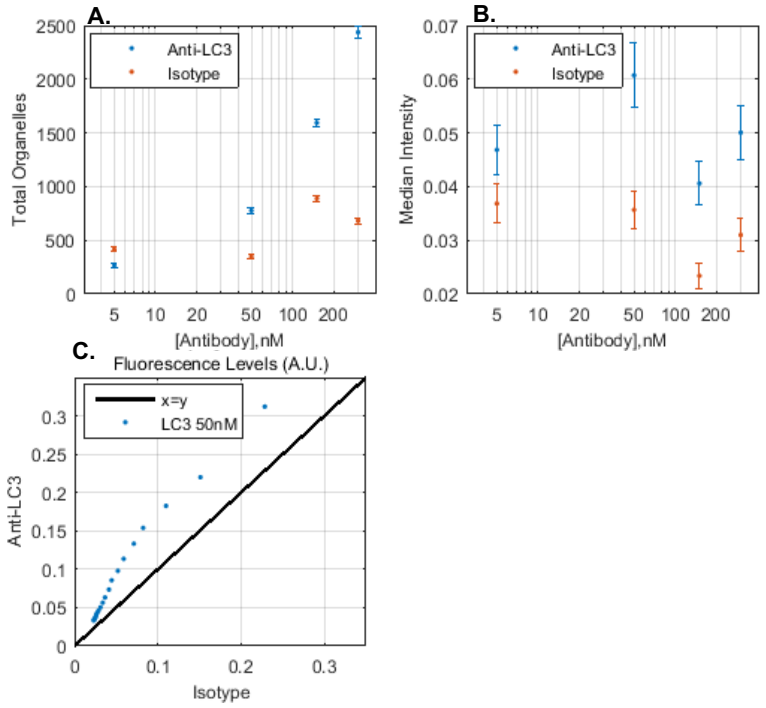

Figure 4. Selection of DyLight488-conjugated anti LC3 antibody concentration for analysis of autophagy organelles from tissue samples. (A) Total organelle events versus antibody concentration. Error bars represent the Poisson distribution standard error, sqrt(n). (B) Median intensity versus antibody concentration. Error bars represent the boundaries of the 40th and 60th percentiles. (C) QQ plot to assess the specificity of 50 nM antibody concentration. DyLight488-conjugated anti-LC3 antibody (y-axis) versus DyLight488-conjugated isotype control (x-axis). Markers represent the 5th-95th percentiles. Data were acquired using capillary cytometry.

Reproducibility of CE-LIF analysis of tissue organelles using optimized antibody concentrations. To investigate reproducibility of CE-LIF analysis we compared the number of events, individual organelle intensity distributions, and individual organelle electrophoretic mobility distributions resulting from replicate injections of a single preparation of organelles that were labeled with 50nM DyLight488 anti-LC3 or 50nM DyLight488 isotype control.

After correction for false positive rate (Equation 1), F/P ratios (Equations 2 and 3) and confirming that there was no peak overlap (Figure S5) there were 283 ± 76 and 26 ±8 organelle events (mean ± std dev; n = 3 injections) when labeled with DyLight488-conjugated anti-LC3 antibody and DyLight488-conjugated isotype control, respectively. Based on these results non-specific binding is ~ 9% relative to specific binding, when using 50nM antibody concentration.

Reproducibility of individual organelle intensity and electrophoretic mobility distributions were assessed using QQ plots (Figures 5A and B, respectively). The percentiles of each technical replicate (y-axis) were visually similar to the replicates pooled (x-axis). If two given distributions of two technical replicates were identical, the slope of a linear fit of their QQ plot should be ~ 1. To investigate if this was the case, we applied linear regression analysis and made pairwise comparisons of the slopes (Figure S6). The mean slopes were 0.8 ± 0.1 and 1.20 ± 0.08 (mean ± std dev; n = 3 comparisons) for the QQ plots of intensity

and electrophoretic mobility distributions, respectively. The differences between slopes were statistically significant only for the intensity distributions and not for the electrophoretic mobility distributions (Figure S6). This is representative of the variability expected for CE-LIF analysis of organelles conducted over 6 hours in which the labeling is done through chemical probes or genetically engineered proteins. Thus, labeling of 50nM DyLight488 anti-LC3 was adequate for the CE-LIF analysis of autophagy organelles isolated from liver tissue, thereby establishing a new method for immunolabeling of organelles for individual organelle analysis by CE-LIF.

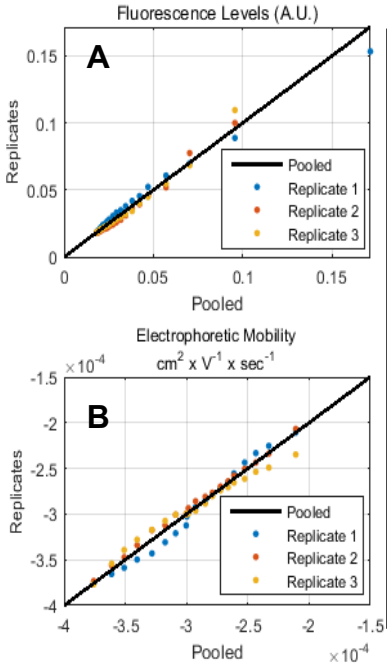

Figure 5. Reproducibility of technical replicates. (A) DyLight488-conjugated anti-LC3 antibody fluorescence (A.U.) for each technical replicate (y-axis) versus the pooled data (x-axis). (B) Electrophoretic mobility ($cm^2 \times V^{-1} \times sec^{-1}$) for each technical replicate versus the pooled data (y-axis). Markers represent the 5th-95th percentiles. Data were acquired using conditions described in Figure 1.

Concluding Remarks

While CE-LIF has been successfully applied to immunolabeled peptide hormones[101], proteins[102–104], and bacteria[105], here we introduce the use of immunolabeling for analysis of individual organelles by CE-LIF. To our knowledge, primary antibodies have never been used to label individual organelles for subsequent analysis by CE-LIF or flow cytometry. Because the antibody is specific molecular target (e.g. LC3), this method is capable of reporting on the heterogeneity on the abundance of such target in individual organelles and should be amenable to analysis of other murine tissue samples. The electrophoretic mobility provides a glimpse at the complex mixture of organelles having LC3-II at their surface. Future work using multiple labeling with other antibodies specific for various autophagy-organelle types and detection in multi-channel LIF detectors[117] would enable further identification of autophagy organelles with LC3-II at their surface. After proper selection and validation of antibodies, the method could also be easily extended to investigate the distribution of other molecular targets in organelles isolated including those from human tissue biopsies. Future methodological developments could include the characterization of K_D values of other organelle-specific ligands including monoclonal antibodies, recombinant antibodies and aptamers.

Chapter 3: Sizing Lipid Droplets from Adult and Geriatric Mouse Liver Tissue Via Nanoparticle Tracking Analysis

Katherine A. Muratore, Charles P. Najt, Nicholas M. Livezey, James Marti, Douglas G. Mashek, and Edgar A. Arriaga. *In preparation for submission to Analytical and Bioanalytical Chemistry.*

Charles P. Najt performed Western blotting of subcellular fractions (See Appendix 2, supplementary information to this Chapter). Nicholas M. Livezey performed TEM of polystyrene latex nanospheres (See Appendix 2, supplementary information to this Chapter). The University of Minnesota Doctoral Dissertation Fellowship and National Instituites of Health (NIH) AG029796 supported K.A.M. This work was supported by NIH AG020866 to E.A.A, DK114401 to D.G.M, and AG055452 to D. G. M. NIH GM008700 supported N.M.L and NIH DK007203 supported C.P.N. A portion of this work was carried out in the Minnesota Nano Center, which receives partial support from the National Science Foundation (NSF) through the NNCI program. A portion of this work was carried out in the Characterization Facility, University of Minnesota, which receives partial support from NSF through the MRSEC program.

Summary

The significance of lipid droplets in lipid metabolism, cell signaling, and regulating longevity is increasingly recognized, yet the unique properties and architecture of lipid droplets make them difficult to size and study using conventional methods. To begin to address this issue, we demonstrate for the first time nanoparticle tracking analysis (NTA) for size measurements of lipid droplets. NTA was found to be adequate to assess lipid droplet stability over time, indicating that lipid droplet preparations are stable for up to 24 hours. NTA had the ability to compare the size distributions of lipid droplets from adult and geriatric mouse liver tissue, suggesting an age-related decrease in lipid droplet size. NTA is suitable for future studies on the complexity of lipid droplet size in order to advance understanding of human disorders associated with improper lipid storage.

Introduction

Intracellular lipid droplets, composed of a neutral lipid core surrounded by a phospholipid monolayer, are found in most cell types. These dynamic organelles play roles in many cellular processes including lipid metabolism, cell signaling, immune function, membrane trafficking, and regulation of longevity[118,119]. Larger triacylglycerol rich lipid droplets (10-200 μm diameter) are present in adipocytes [120,121] while smaller lipid droplets (1 μm diameter or less) enriched in cholesteryl esters exist in brown adipose tissue, liver, muscle, heart, and connective tissues [122]. The accumulation of excess lipids in lipid droplets is associated with a multitude of lipid storage associated disorders, including lipodystrophies, obesity, cachexia, atherosclerosis, and non-alcoholic fatty liver disease (NAFLD)[43]. In these disease states, the accumulation of lipid droplets is both a hallmark and etiological factor in disease development and progression[123,124]. Although numerous studies have defined the molecular and physiological changes that occur in the progression of these diseases, techniques to study individual lipid droplets are limited. To begin to address this, it is imperative to investigate new methods that enable the measurement of individual lipid droplets.

The most commonly employed method of measuring lipid droplet size is confocal fluorescent microscopy [44–46]. Lipid droplets in cells and tissue sections are visualized by a number of commercially available lipophilic dyes [47–50] and the area and number of lipid droplets in the field of view are quantified using image

analysis software [51]. Measuring the size of individual lipid droplets from microscopy images is not high-throughput and microscopy experiments with lipophilic dyes must be interpreted with caution, as the fluorescence signal is influenced by variations in the cellular distribution of the dye and its incorporation into other lipid rich structures. Colocalization experiments with *bona-fide* lipid droplet markers are required for correct identification of lipid droplets, but often these lipid droplet proteins do not coat all lipid droplets. Further, in order to evaluate lipid droplets in tissues by microscopy, the sample of interest must be embedded, sectioned, and stained prior to visualization [49], requiring a major time investment. Recently developed anti-Stokes Raman Scattering (CARS) [54] and Stimulated Raman Scattering (SERS) [55] imaging methods have been used to size lipid droplets in cells. While these label-free methods represent an improvement over fluorescent microscopy, a sophisticated instrumental setup is required and these methods are further limited by the relatively low signal intensity and long acquisition time required for Raman-based imaging techniques. Despite existing imaging methods for measuring lipid droplet size in cells and tissues, a label free method based on individual lipid droplet size measurements would reduce the bias introduced by limited throughput, alleviate the necessity of complex instrumental setup and the use of lipophilic dyes, and allow the lipid droplets to be recovered for downstream analysis.

Flow cytometry and capillary cytometry are well-defined methods for determining heterogeneity among individual organelles[35,79,125]. To our knowledge, there has been no report size measurements of lipid droplets by flow cytometry, possibly due to their unique physiochemical properties including low specific gravity and tendency to adsorb to surfaces. Size distribution of individual lipid droplets isolated from cells and tissues has been measured by dynamic light scattering (DLS) [44], but this method is an ensemble technique based on the assumption that dispersed particles are uniform in composition, making it inappropriate for heterogeneous biological samples. Furthermore, DLS measurements are highly influenced by the presence of large particles or aggregates in the particle suspension.

Nanoparticle tracking analysis (NTA) is a single-particle measurement technique, as opposed to the ensemble approach of DLS, enabling it to measure individual nanoparticle size and concentration in a given sample[126]. In NTA, a particle dispersion is placed within an optical cell and irradiated with an intense laser source. The light scattered by individual particles within the cell is collected using a microscope objective and recorded with a camera. While the particles are too small to image optically, their scattered light reveals the position and Brownian motion of each particle in the field of view. The recorded motion is analyzed to derive the two-dimensional diffusion constant of each particle, which is then used to calculate the particle's sphere equivalent hydrodynamic radius. Unlike DLS,

NTA provides a direct number-weighted particle size distribution and increased size resolution for non-uniform samples. NTA has been used previously to determine the size and concentration of biological particles, including exosomes [81–84], virus particles[85] and gold nanoparticle protein conjugates,[86] but has never been used to measure the size of lipid droplets.

This article introduces a new method for monitoring lipid droplet size in tissues using NTA. Analysis of isolated lipid droplet dispersions via NTA takes less than ten minutes, and can be applied to lipid droplets isolated from any tissue or cell of interest. Further, NTA is non-destructive, and the lipid droplets can be recovered after measurement for downstream analysis. We assessed the ability of a Nanosight LM-10 instrument to measure size and determined its suitability to measure lipid droplets isolated from mouse liver. We also applied the method to monitor lipid droplet preparation stability over time and measure the lipid droplet size distributions in adult and geriatric mice. This work represents the first size measurements of isolated lipid droplets. In the future, NTA of lipid droplets could be used to examine lipid droplets obtained from tissue and cell lines of any model system, model organism, or clinical sample of interest.

Experimental Section

Materials, Reagents, Buffers, and Solutions. Sucrose and ethaminetetraacetic acid (EDTA) were obtained from Sigma Aldrich (St. Louis, MO). Tris base was obtained from Thermo Fisher (Waltham, MA). Water was purified with a Millipore Synergy UV system (18.2mΩ/cm, Bedford MA). Liver homogenization buffer (Buffer H) consisted of 250mM sucrose, 10mM Tris, pH 7.0. Buffer A, 2X concentration, consisted of 500mM Sucrose, 2mM EDTA, and 40mM Tris-base, pH 7.8. Sucrose gradient step solutions (25% and 35% sucrose v/v) were mixed with Millipore water to a final concentration of 1X Buffer A. Pierce Protease Inhibitor Mini Tablets (AEBSF, aprotinin, bestatin, E-64, leupeptin and pepstatin A, Thermo Fisher, Waltham MA) were added to all buffers in accordance with manufacturer's instructions.

Human and Animal Rights Statement. All mice were housed in a designated clean facility and treated in accordance with protocols approved by the University of Minnesota Insitutional Animal Care and Use Committee.

Lipid droplet isolation from mouse liver. Lipid droplets were prepared from the livers of C57BL6 female mice, as described previously [127,128]. Mice were euthanized by intraperitoneal injection of pentobarbital (200 mg/Kg) and the liver was excised. All isolation steps were done at 4°C. The liver was weighed and

minced in a petri dish into small (1mm) pieces using a flat razor blade and resuspended in 3mL of Buffer H. The liver homogenate was transferred into a nitrogen cavitation chamber and charged to 200 psi. After 15 minutes on ice, the cell lysate was released from the nitrogen cavitation chamber into a 50 mL conical tube and centrifuged at 1,000g for 10 minutes. The post nuclear supernatant was loaded onto a sucrose step gradient (4mL 35% sucrose/Buffer A, 4mL 25% sucrose/Buffer A) and centrifuged at 36,000 rpm in a Beckman SW 41 swinging bucket rotor for four hours. The lipid droplet fraction appeared as a white film at the top of the tube, and was then removed with a glass Pasteur pipette. The lipid droplet suspension was mixed by pipetting and diluted 1:90 in Buffer H prior to loading into the Nanosight LM-10 analysis chamber.

For stability measurements, lipid droplets were isolated from a 9-month-old C57BL/6 mouse. The lipid droplet sample was measured initially after isolation using NTA (Day 0). The lipid droplet suspension was stored in an microcentrifuge tube on a rotator in a 4°C cold room. The lipid droplet suspension was sampled at 24 hours, 48 hours, and one week later (samples designated Day 1, Day 2, and Day 7). To investigate the differences in lipid droplet size distributions between geriatric mice and adult mice, lipid droplets were isolated from n=3 livers from geriatric mice and n=3 livers from adult mice prior to NTA. Mice in the adult group were 9 months and mice in the geriatric group were 28 months.

Nanoparticle Tracking Analysis. The size distributions of lipid droplets, along with those of particle size standards, were measured using a Nanosight LM-10 Nanoparticle Tracking Analyzer (Malvern, Salisbury, UK). The instrument was equipped with a 405nm laser and a high sensitivity CMOS camera. Quadruplicate videos of each sample were captured for 60 seconds in static mode. The frame rate was 25 frames per second, and up to 1,500 frames were captured per video. The chamber temperature was controlled at 25°C, the camera gain was set to "automatic" and the viscosity was set to "water". Videos were analyzed with NTA 3.2 Dev Build 3.2.16 software to yield a number-weighted size distribution in the size range of interest (between about 30 and 1000nm), along with several statistical measures of that distribution, including its median, mean, and standard deviation. To verify particle size accuracy, polystyrene latex nanosphere standards were also measured at three sizes: 203nm ± 6 nm standard deviation (#3K-200), 102nm ± 8 nm standard deviation (#3K-100), and 31nm (#3030A). All particle standards were obtained from Thermo Fisher Scientific (Waltham, MA) and dilutions were made in sterile filtered distilled water.

Data Analysis. Each particle's motion is tracked individually from frame to frame during the 60 second measurement period. The NTA software examines each track to determine if it meets the quality criterion, i.e., staying within the field of view for a sufficient number of frames to accurately reconstruct the particle

motion. Using the subset of the raw track data that meets this criterion, the NTA software calculates the particle's diffusion constant (D, m^2/s) resulting from Brownian motion. The diffusion coefficient is subsequently used to calculate a sphere equivalent hydrodynamic radius (r_h), through the Stokes-Einstein relationship (Equation 1)

Equation 1 $$D = \frac{K_B T}{6\pi\eta r_h}$$

where K_B is Boltzmann's constant (1.38064852 × 10^{-23} m^2 kg s^{-2} K^{-1}), T is temperature (25°C), and η is viscosity of water (0.89 N s/m^2 at 25°C). While Brownian motion occurs in three dimensions, the Nanosight observes the individual particles in two dimensions and the NTA software derives D using the equation below (Equation 2)

Equation 2 $$D = \frac{\overline{(x,y)}^2}{4t}$$

where t is time and x and y are distance on two orthogonal axes. As diffusion is isotropic in space and occurs independently in all directions, 2D measurement of movement is an accurate representation of 3D Brownian motion [129,130]. Size distribution (number weighting), size percentiles, summary statistics and videos were exported from NTA 3.2.

Raw lipid droplet size measurements were corrected using particle standard data via the procedure described below. The % error (*e*) in NTA measurement was calculated using Equation 3:

Equation 3 $$e = \frac{\mu - \bar{x}}{\mu} * 100$$

Where μ is the mean particle size reported by TEM, and $\bar{x}$ is is the mean size of the particle standard reported by NTA. The % error *e* at each lipid droplet size was calculated from the particle standard measurements using the approach described in Supplementary Data Analysis.

As each error in measurement was in the positive direction, a correction factor for each size was calculated using Equation 4:

Equation 4) $$c = 1 - e/100$$

The corrected LD particle size (LD_1) was calculated using Equation 5.

Equation 5) $$LD_1 = LD_0 * c$$

where LD_0 is the observed LD particle size and c is the correction factor.

Histograms and quantile-quantile (QQ plots) were used to compare distributions of lipid droplet sizes. QQ plots were created by plotting the fifth through 95th percentiles from two sample distributions. If the two distributions are similar in shape, their QQ plot approaches an X=Y line. A single preparation of lipid droplets was measured at days 0, 1, 2, and 7. For visual evaluation of the stability of the preparation, the QQ plot was produced by plotting 19 quantiles (representing the 5th-95th percentiles) of the size distributions from days 1, 2, and 7 versus the respective 5th through 95th percentiles of the size distributions from day 0. For visual analysis of the difference in LD size distribution between old and young mice, the QQ plot was produced by plotting each of the 5th-95th percentiles (avg ± SEM) of three biological replicate old mice versus the respective percentile (avg ± standard error of measurement, referred hereafter as "SEM") of three biological replicate young mice. ANOVA and Tukey post-hoc testing was done in Prism 7 (GraphPad, San Diego, CA). Wilcoxan Rank Sum test, linear regression, size data correction, and data plotting was done in MATLAB 2016b (MathWorks, Natick, MA).

Results and Discussion

Figures of Merit. In order to evaluate the suitability of the Nanosight LM-10 in lipid droplet analysis, we assessed the ability to determine size accurately over the size ranges expected to be found in lipid droplets. According to the manufacturer's specifications, the Nanosight LM-10 is suitable to measure

concentrations of ~106 to ~109 particles/ml in the size range from 10nm to 2000nm. These values are dependent on the nature of the particles being measured. We selected polystyrene latex nanospheres (refractive index (1.615) [26]) over metallic nanoparticles (refractive index > 2.0) because the former's refractive index is similar to that of individual organelles, such as mitochondria (1.41) [27], and triglycerides (1.43-1.48) [28], the main component of lipid droplets.

We used polystyrene latex nanospheres of different sizes to determine the size accuracy of measuring biological particles on the Nanosight LM-10 (Table 1). The expected mean size of the smallest polystyrene latex nanoparticles used in this study, determined by the manufacturer using DLS, was 31 nm. At a particle concentration of (1.66 ± 0.08) x 10^9 particles/mL, the mean particle size as measured by NTA was 38 ± 1 nm (± SEM). The size distributions of the particle standards obtained via NTA can be visualized in a histogram, Figure 1A. We sized the nominal 31nm particles by TEM (Supplementary Figure 1) to provide individual particle size measurements to compare with NTA measurement. TEM analysis indicated that the mean diameter of the 31 nm standards was 25 nm ± 5 nm (± SEM). Therefore, at a 25 nm polystyrene nanosphere size, NTA reports a 52% higher mean particle size than TEM. We subsequently measured the 102 nm ± 8 nm (± SEM) and 203 nm ± 5 nm (± SEM) particle standards by NTA (Figures 1B and 1C). The Nanosight reported a 5% higher mean particle size

than TEM at 102 nm, and was is in agreement with the TEM measurement at 203 nm. We used the measurement of these three standards to correct the sizes of lipid droplets reported by NTA. The correction factor was different for each size and was calculated using Equations 3 and Equation 4.

We also measured a dilution series of the 203nm polystyrene latex nanospheres to establish a low concentration limit for biological particles on the Nanosight LM-10. The results from measurements of the dilution series is summarized in Table 2. At the highest particle concentration measured, 1.59×10^9 particles/mL, the mean particle size was 203 ± 1 nm (± SEM). At the lowest particle concentration measured, $(1.43 \pm 0.66) \times 10^7$ particles/mL, the mean particle size was 174 ± 24 nm. The tabulated data suggest that NTA decreases in measurement accuracy at concentrations below $(2.58 \pm 0.18) \times 10^8$ particles/mL. While the manufacturer indicates the Nanosight LM-10 can accurately size measure ~10^6 to ~10^9 particles/mL, our data suggests that NTA is only appropriate for biological particle concentrations near the high end of the manufacturer's recommended range.

	Size Measurement		
Mean Particles/ml	NTA	TEM	DLS
(1.66 ± 0.08) x 10^9	38 ± 1 nm	25 +/- 5 nm*	31nm
(2.13 ± 0.07) x 10^9	108 ± 1 nm	102 +/- 8 nm	N/A
(1.59 ± 0.01) x 10^9	203 ± 1 nm	203 +/- 5 nm	N/A

Table 1. Analysis of Polystyrene Latex Nanosphere Standards. Values are represented as mean ± SEM. NTA measurements had n=5 technical replicates. *indicates TEM done in this study, n=60 nanospheres. TEM measurements for additional standards are as reported by the manufacturer (Thermo Fisher, Waltham, MA).

Mean Particles/ml	Mean Particle Size, nm	Mean Particles/frame
(1.59 ± 0.01) x 10^9	203 ± 1	81 ± 1
(2.58 ± 0.18) x 10^8	218 ± 2	13 ± 1
(1.60 ± 0.07) x 10^8	218 ± 1	8 ± 0.4
(1.43 ± 0.66) x 10^7	174 ± 24	1 ± 0.3

Table 2. Dilution series of 203nm standard polystyrene latex nanospheres. Values are represented as mean ± SEM, n=5 technical replicates. The second column gives the mean number of particles tracked by NTA software per frame of recorded video.

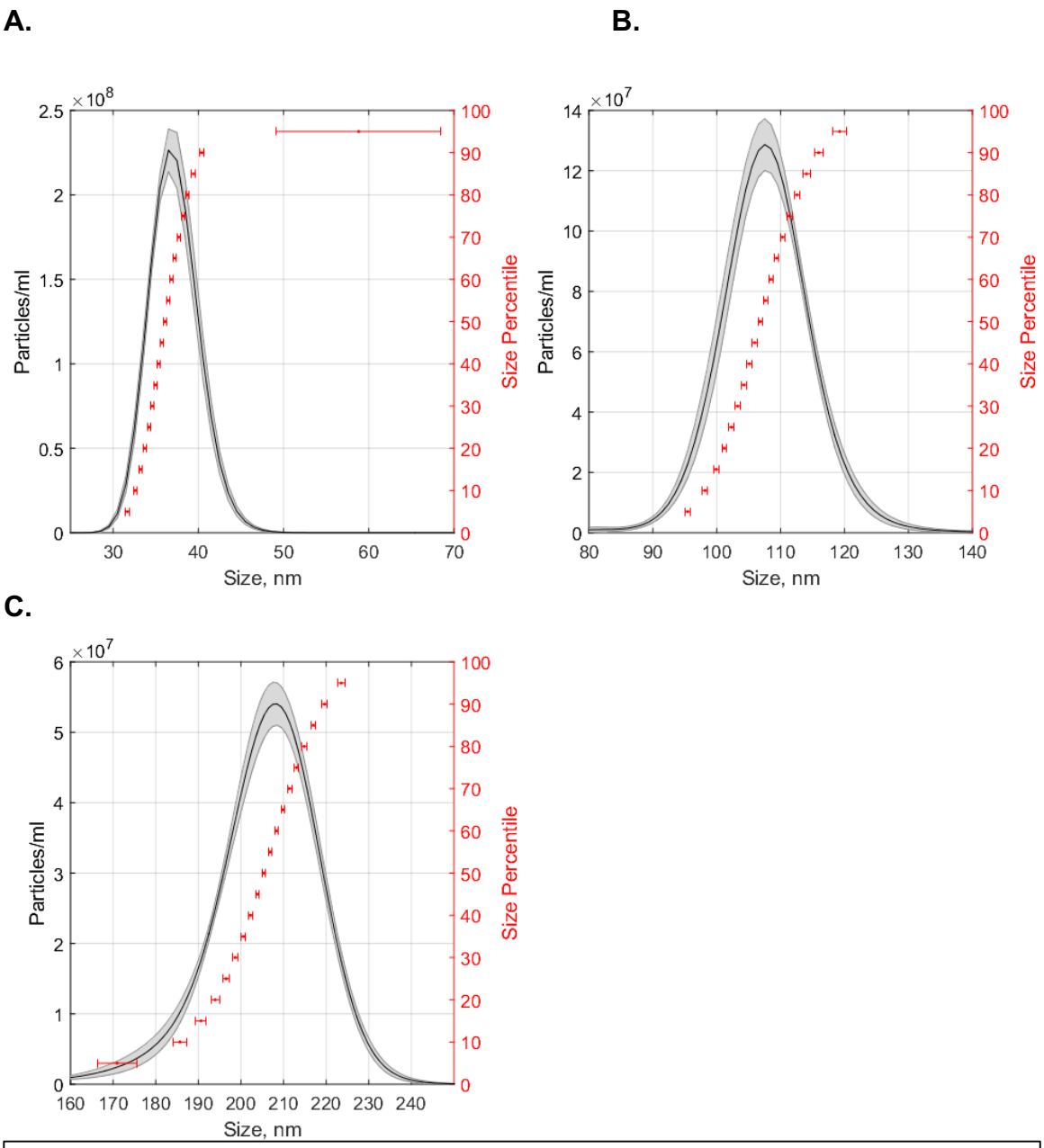

Figure 1. Histograms and size percentiles (5^{th}-95^{th}) of polystyrene latex nanosphere standard size distributions as reported by NTA, A. 31nm B. 102nm C. 203nm. Shaded area of histogram represents ± SEM, n=5 technical replicates. Error bars represent ± SEM, n=5 technical replicates.

Nanoparticle Tracking Analysis of Individual Lipid Droplets. The next focus of this report was to determine the suitability of NTA for measuring the size distributions of lipid droplets. Prior work demonstrated the use of NTA to measure size distributions of biological particles, most notably exosomes (20-100nm in size),[81–84] but has not been done in conjunction with determining measurement error using size standards and subsequent correction of the raw data. Furthermore, NTA has never been applied to lipid droplets.

Lipid droplets were isolated from mouse liver tissue and the purity of the cellular fractions were validated by Western blot (Supplementary Figure 2). In the Nanosight chamber, lipid droplets act as individual point scatterers when illuminated with 405nm light. Therefore, the lipid droplets appeared as small points of light undergoing random, Brownian motion (Supplementary Movie 1) from which their individual motion paths could be tracked with a high frame rate CCD camera (30 fps). The diameter of the individual particles can be calculated from their diffusion constant using Equation 1 and Equation 2 in Nanosight NTA software, and corrected using the standard particle measurements as described in the Supplementary Data Analysis.

A histogram was used to visualize the corrected size distribution of lipid droplets isolated from mouse liver tissue (Figure 2). The mean corrected particle size was 168 ± 2 nm (mean ± SEM, n=5 technical replicates) and the particle

concentration was (2.13 ± 0.14) x 10^9 particles/ml (mean ± SEM, n=5 technical replicates). In non-adipocytes, lipid droplets do not exceed 1um in diameter.[131] The liver lipid droplet sizes ranged from 105 to 295nm (5^{th}-95^{th} percentiles) in diameter, which was representative of the lipid droplet size heterogeneity present in this particular tissue.

Lipid Droplet Stability Analysis. To investigate the stability of lipid droplets during storage, we compared the individual lipid droplet size distributions resulting from uncorrected measurements of a single preparation of lipid droplets over the course of a week. The mean lipid droplet size and mean lipid droplet concentration for each day are summarized in Table 3. The shift in distribution shape apparent on each day can be further appreciated by histograms (Supplementary Figure 3). One way ANOVA analysis indicated statistically significant differences in mean LD size (Supplementary Table 1A) and mean LD concentration (Supplementary Table 2A) sampled on all four days. This suggests that the lipid droplet preparation was not stable over the one week period. Tukey post-hoc testing indicated that mean LD size on Day 7 is significantly different from Day 0, Day 1, and Day 2 (Supplementary Table 1A, $p < 0.0001$) and there was no significant difference between pairs Day0-Day1, Day0-Day2, and Day1-Day2. Furthermore, the mean LD concentration on Day 2 is significantly different from Day 0, Day 1, and Day 7 (Supplementary Table 1B, $p = 0.0001$) but there

was no significant difference between pairs Day0-Day1, Day0-Day7 and Day1-Day-7.

While the ANOVA and Tukey analysis demonstrated changes in the population mean, we chose to use a QQ plot to make individual comparisons of the LD size distributions of each Day 1, Day 2, and Day 7 versus Day 0 (Figure 3). The percentiles of Day 1 and Day 2 (y axis) were visually similar to Day 0, while the percentiles of Day 7 shifted in the positive y-direction. If two distributions are similar in shape, a QQ plot comparing them approaches an X=Y line. Thus, the slope of the linear fit of their QQ plot will be ~1. To investigate if this was the case, we applied linear regression analysis and made pairwise comparisons of the slopes. The distributions between slopes were not statistically significant for Day 1 vs Day 0. The statistical significant difference between the Day 2 vs Day 0 slope is indicative of changes in the lipid droplet size distribution. Not surprisingly, the comparison of Day 7 vs Day 0 displayed the largest changes and cannot be fit to a linear model. Thus, based on the ANOVA, post-hoc Tukey, QQ plots and linear regression analysis, lipid droplets maintain their stability for 24 hours. These results suggest size analysis of isolated lipid droplets must be completed within 24 hours to ensure accurate representation of the lipid droplet distribution isolated from the sample of interest.

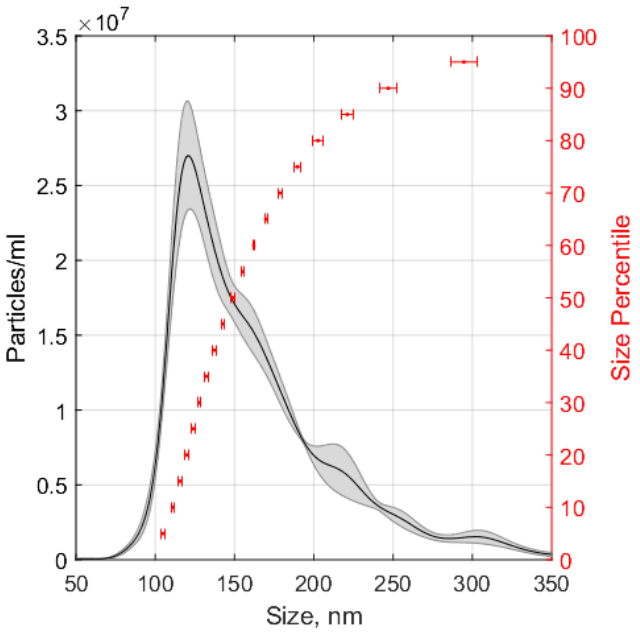

Figure 2. Histogram and percentiles (5^{th}-95^{th}) of corrected mouse liver lipid droplet size distribution. Shaded area of histogram represents ± SEM, n=5 technical replicates. Error bars represent ± SEM, n=5 technical replicates. The particle concentration was (2.13 ± 0.14) x 10^9 particles/mL (mean ± SEM, n=5 technical replicates).

Day	Mean LD Concentration particles/ml	Mean LD size, nm
0	(2.13 ± 0.14) x 10^9	170 ± 2
1	(2.11 ± 0.09) x 10^9	167 ± 4
2	(1.38 ± 0.07) x 10^9	180 ± 3
7	(2.35 ± 0.14) x 10^9	221 ± 3

Table 3. Lipid Droplet Stability Study. Each row represents the average LD concentration (particles/ml) and mean raw LD size (nm) as given by NTA, n=5 technical replicates, mean ± SEM.

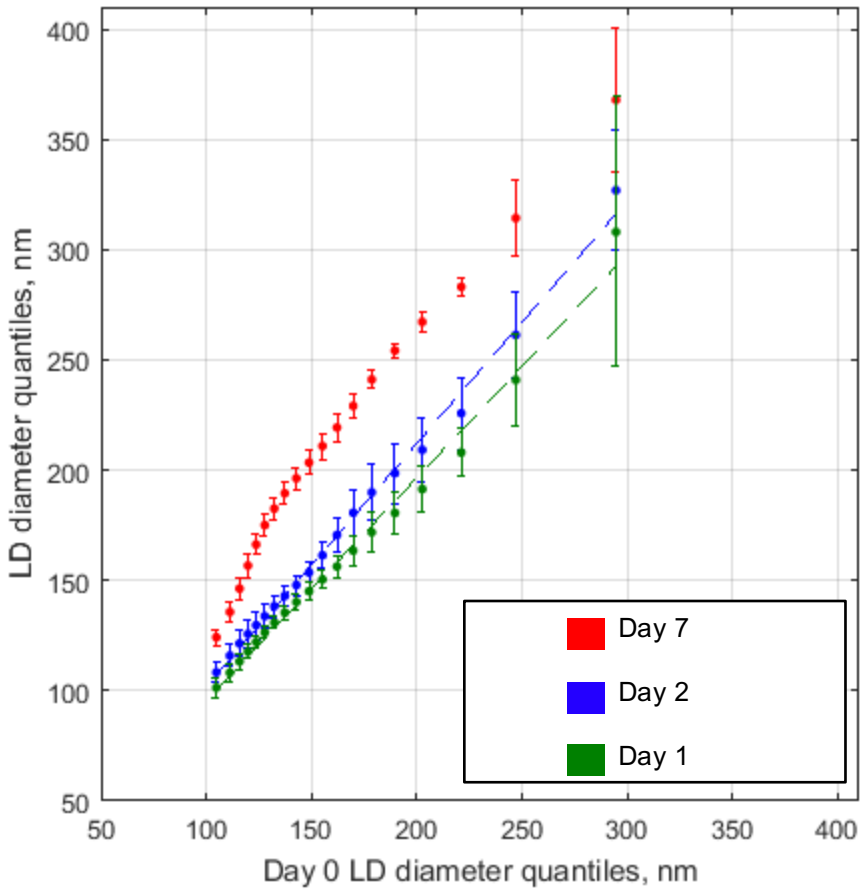

Figure 3. Stability of uncorrected lipid droplet size distribution. LD diameter (nm) for Days 1, 2, and 7 (y axis) vs Day 0 (x-axis). Markers represent the 5^{th}-95^{th} percentiles. Dotted lines represent linear regression of each Day vs Day 0. Day 1 vs Day 0 slope confidence interval is [0.96 1.1] and Day 2 vs Day 0 slope confidence interval is [1.1 1.2]. R^2 is 1.0 for both fits. Day 7 vs Day 0 fit was non-linear and not represented in the plot. Linear regression analysis was further investigated by graphing of the residuals (Supplementary Figure 3).

Lipid Droplet Size Analysis in Adult and Geriatric Mice. The population of lipid droplets in any given cell is size heterogeneous, and evidence suggests that LDs of various sizes differ in in lipid composition and the recruitment of cytosolic proteins[132]. Lipid droplet size changes resulting from different membrane composition and protein recruitment have been reported previously[133], but have never been described in a comparative aging study. Aging is associated with lipid accumulation in multiple tissues, including the liver[4,134], but the effect of age-related lipid accumulation on lipid droplet size or number has not yet been investigated. This work represents the first measurements of lipid droplet size distribution in geriatric mice.

The mean corrected LD size is summarized in Table 4. It indicates a larger variation in mean lipid droplet size among the geriatric mice. The distributions in corrected lipid droplet sizes were further compared using a QQ plot (Figure 4A). The general trend of the geriatric quantiles was a shift towards the x-axis from the adult quantiles, which is indicative of a smaller size. Furthermore, the clear deviation from the 5^{th}-65^{th} percentiles suggested an increased abundance of smaller lipid droplet sizes in the geriatric mouse samples. The uniqueness in the distribution of each aging mouse is captured by plotting the lipid droplet size distribution from each geriatric mouse versus the average lipid droplet size distribution from the adult mice (Supplementary Figure 5). The relative variation beginning at the 70^{th} percentile among animals is illustrated by plotting the

relative uncertainty of each quantile versus the quantile values (Supplementary Figure 6).

A statistical significance profile was necessary to ascertain the average size distribution disparities that exist in the geriatric mice as compared to the adult mice (Figure 4B). Statistically significant ($p<0.05$) differences existed in all regions except for the last 10% of the distribution (representing 90^{th}-99^{th} percentiles, 302nm-528nm for geriatric mice and 322-619nm for adult mice). The most significant area of the distribution was the first 10% (representing 1^{st}-9^{th} percentiles, 14-19nm for geriatric mice and 86-109nm for adult mice), indicating that the widest disparity between the average distributions existed at the lowest end of the distribution, representing the smallest lipid droplets. Thus, geriatric mice have a statistically significant different distribution of lipid droplet sizes than the adult mice, with the direction of the shift being toward the smaller size.

Mouse	Mean LD size, nm
Geriatric 1	149 ± 20
Geriatric 2	184 ± 6
Geriatric 3	84 ± 6
Adult 1	168 ± 2
Adult 2	240 ± 7
Adult 3	227 ± 4

Table 4. Lipid Droplets from Adult and Geriatric Mice. Each row represents the mean corrected LD size (nm), n=5 technical replicates, mean ± SEM.

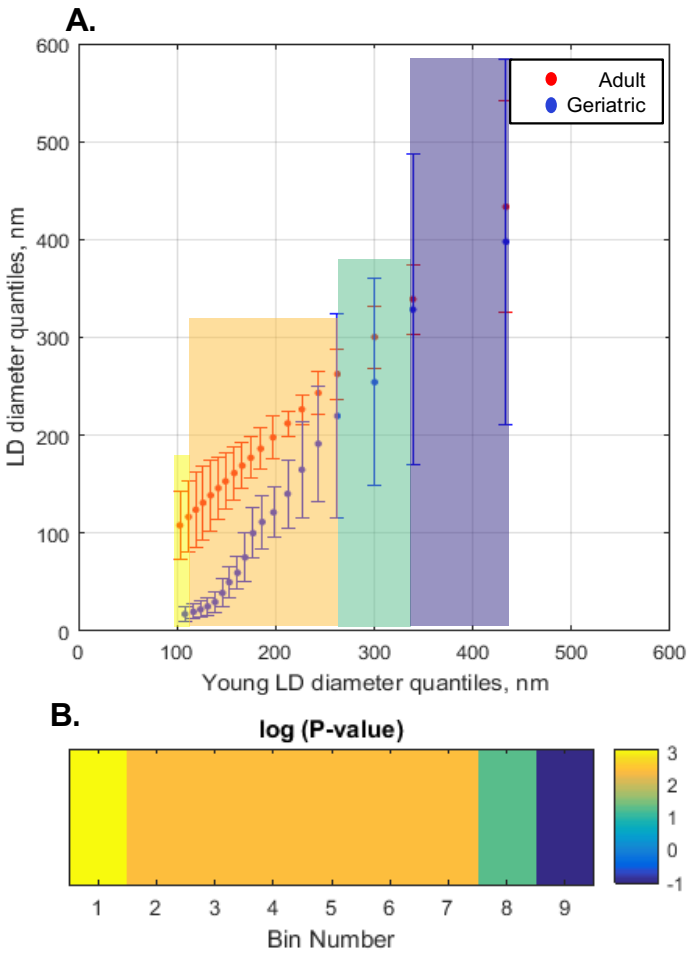

Figure 4. QQ plot of Adult and Geriatric Mice. (a) Lipid droplets were isolated from n=3 livers from geriatric mice and n=3 livers from adult mice prior to NTA. Mice in the adult group were ~35 weeks and mice in the geriatric group were ~115 weeks. LD diameter (nm) geriatric (y axis, blue) and adult (y axis, red) vs adult (x-axis). Markers represent the average 5^{th}-95^{th} percentiles ± SEM, n=3 mice per group. The areas of the significance plot corresponding to the quantiles are shaded on the plot. (b) Significance plot from hypothesis testing of average adult and average geriatric LD size distributions. A Wilcoxan Rank Sum test was calculated for between the percentiles of each distribution (for each 10% of the data set, Bins 1-9) from 1% to 99%. Each p-value was transformed by calculating $-1.3\text{-}\log_{10}$(P-value). This was done for ease of visualization, such that all P-values <0.05 are transformed as above 0 and all P-values that are >0.05 are transformed as below zero[181].

Concluding Remarks

While NTA has been successfully applied to exosomes,[81–84] virus particles[85] and gold nanoparticle protein conjugates,[86] here we introduce NTA for the size measurements of lipid droplets isolated from tissues. To our knowledge, lipid droplets have not been sized in isolation. This method is capable of measuring the size distributions of lipid droplets from any tissue or cell type amenable to lipid droplet isolation, including human tissue biopsies. The complete procedure from tissue excision, organelle isolation and NTA analysis can be completed in approximately 6 hours, and the lipid droplet sample can be recovered and used in downstream analysis. This represents a vast improvement over the time consuming and low throughput imaging based lipid droplet size measurements.

Chapter 4: Defining the Inter-Regulation of Autophagy and Cholesterol Homeostasis

Katherine A. Muratore, Michelle M. Kuhns, Gregory G. Wolken, Joshua D. Ochocki, Vratislav Kostal, Mark D. Distefano, and Edgar A. Arriaga. *In preparation for submission, journal TBD.*

Michelle M. Kuhns designed, conducted, and analyzed the unbiased proteomics project. Gregory G. Wolken conducted one replicate of the unbiased proteomics project. Joshua D. Ochocki conducted prenylation experiments. Vratislav Kostal conducted imaging experiments on siRNA treated cells. Katherine Muratore designed, conducted and analyzed the rest of the experiments. Mark D. Distefano was Joshua D. Ochocki's advisor. This work was supported by NIH R01AG020866 to E.A.A. The University of Minnesota Doctoral Dissertation Fellowship and NIH T32AG029796 supported K.A.M.

Summary

Autophagy plays a key role in regulating lipid homeostasis, but it is not known if autophagy works with the mevalonate pathway to maintain cholesterol abundance. Here, we investigated how autophagy related gene ATG7 controls two mevalonate pathway products, protein prenylation and cholesterol. We found that ATG7 gene knockdown decreased mevalonate pathway gene expression, and increased mevalonate pathway protein abundance, cholesterol abundance, and protein prenylation. These results suggest autophagy inhibition reduces flux through the mevalonate pathway, which serves as a framework for further investigation into the contribution of macrolipophagy to cholesterol abundance.

Introduction

Macroautophagy (referred hereafter as “autophagy”) is an intracellular degradation process, conserved in all eukaryotes, that is critical in the maintenance of cellular homeostasis.[135] Autophagy is responsible for the degradation of large cellular components, including misfolded protein aggregates, dysfunctional organelles, and microorganisms.[12] The autophagy process results in the sequestration of bulk cellular components into double membrane vesicles called autophagosomes, which undergo subsequent fusion with lysosomes for cargo degradation.[15] In the liver, cholesterol is obtained from lipid droplets via selective autophagy.[7–9]

In addition to selective autophagy, cholesterol is also obtained from *de novo* synthesis via the mevalonate pathway, which suggests that autophagy works in conjunction with the mevalonate pathway to maintain cholesterol homeostasis. The mevalonate pathway is responsible for converting acetyl coenzyme A to cholesterol through isoprenoid intermediates. Isoprenoids can be converted to squalene, the first committed step in cholesterol synthesis, or used as substrates for protein prenylation (Figure 1). The mevalonate pathway regulates autophagy through Rab prenylation in mammalian cells, drosophila, and yeast.[87–90] Despite the evidence suggesting a role for the mevalonate pathway in controlling autophagy through Rab prenylation, the regulation of cholesterol synthesis by autophagy has not been investigated. Prior to this study, the relationship

between autophagy and the mevalonate pathway was completely unexplored in L6 rat myoblasts, which are immortalized mononucleated muscle precursor cells.[136]

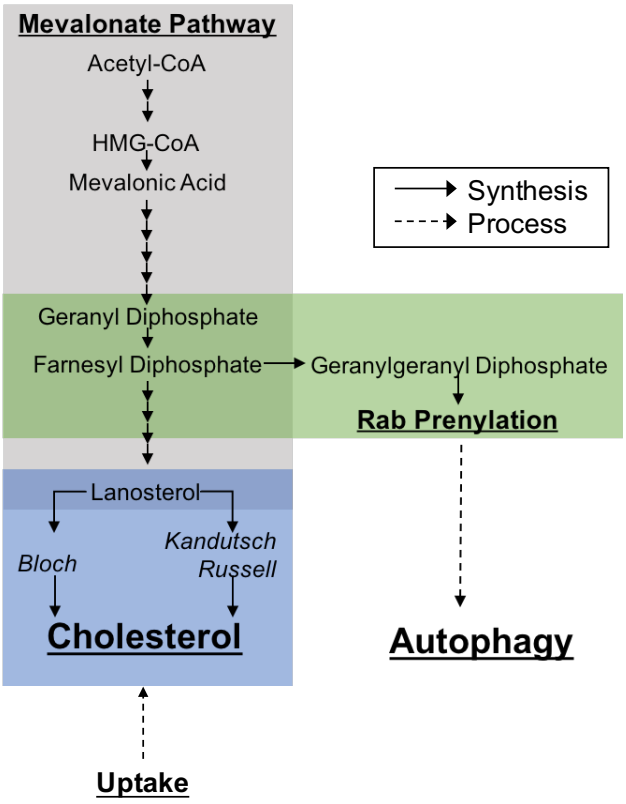

Figure 1. The mevalonate pathway synthesizes cholesterol through isoprenoid intermediates. Steady state free cholesterol is maintained by three sources: (i) mevalonate pathway synthesis, (ii) breakdown of lipid droplets and organelles by autophagy, and (iii) uptake. Acetyl CoA is converted to isoprenoids geranyl diphosphate and farnesyl diphosphate. These isoprenoids can either be converted to squalene, the first committed step in cholesterol synthesis or used as substrates for protein prenylation (green box). Cholesterol synthesis from squalene occurs via the Bloch or Kandutsch Russell pathways (blue box). Rab prenylation is required for autophagy, but it is not yet known how autophagy regulates cholesterol synthesis.

In this work, we investigated how an autophagy related gene, ATG7, controls two products of the mevalonate pathway, cholesterol and protein prenylation. We measured changes that occurred in the mevalonate pathway in conjunction with knockdown of autophagy-related gene ATG7 in L6 rat myoblasts. ATG7 is a protein required for autophagy initiation and its gene expression has been modified in vitro[137–139] and in mice[140] to inhibit autophagy. ATG7 knockdown results in impaired autophagy, an increase in free cholesterol, and an increase in incorporation of prenyl modifications. Further investigation into the regulation of the mevalonate pathway revealed that ATG7 knockdown increased the abundance of cholesterol synthesis proteins, and decreased the expression of cholesterol synthesis genes. Here we report that ATG7 knockdown affects gene expression and protein abundance in the mevalonate pathway and that increased cholesterol abundance and impaired autophagy are key in mediating these effects.

Materials and Methods

Cell Culture. L6 rat myoblasts (American Tissue Culture Collection, Manassas, VA) were maintained at 37°C, 5% CO2, in high glucose Dulbecco's Modified Eagle Medium (Thermo Fisher, Waltham MA) supplemented with 10% fetal bovine serum, 200μM glutamine, 1000 units penicillin, and 10μg/μl streptomycin. For propagation, cells were lifted with 0.5% Trypsin-Ethylenediaminetetraacetic acid in phosphate buffered saline (Thermo Fisher, Waltham MA) and split 1:20

(v/v) every 48 hours. Unless otherwise indicated, the cells were maintained for a maximum of ten passages.

siRNA transfection. Unless otherwise noted in Supplementary Information, siRNA transfection proceeded as follows. Silencer Select siRNA (ATG7 #s161901 and negative control #4390843), Lipofectamine RNAiMAX and Opti-MEM serum free media were obtained from Thermo Fisher (Waltham, MA). RNA-lipid complexes were prepared in Opti-MEM, allowed to incubate at room temperature for 20 minutes and delivered to cells at a final siRNA concentration of 10nM. The cells were cultured for 48 hours prior to harvest, in agreement with literature precedence.[137–139] Unless otherwise noted, biological replicates are multiple transfections in independent flasks or plate wells, seeded from the same source of cells.

Free Cholesterol Measurement. The Amplex Red Cholesterol Assay Kit (Thermo Fisher, Waltham MA) was modified as follows to measure free cholesterol in cell lysates. Lysis buffer consisted of 150mM sodium chloride (Sigma Aldrich, St. Louis, MO) 1.0% Nonidet P-40 (Merck Millipore, Billerica, MA), 0.5% sodium deoxycholate (Sigma Aldrich, St. Louis, MO), and 0.1% sodium dodecyl sulfate (Bio-Rad, Hercules, CA), pH 7.2. Cells were resuspended at 10^6 cells/ml and lysed in lysis buffer. 50ul of modified working reagent (300uM Amplex Red, 2U/ml cholesterol oxidase, and 2U/ml horseradish peroxidase in

manufacturer provided Reaction Buffer) was dispensed into a black plastic 96 well plate containing 50ul cell lysate per well using a Synergy 2 (Bio-Tek, Winooski, VT) plate reader. The plate was incubated at 37°C temperature inside the plate reader, shaken every five minutes and was read at 525nm excitation and 590nm emission. The omission of the cholesterol esterase included in the Amplex Red kit enabled the measurement of free cholesterol alone (Supplementary Figure 1).

Cholesterol Synthesis Measurement. For cholesterol synthesis measurements in complete media, cells were transfected as described above in a six well plate and allowed to incubate for 48 hours. The media was replaced with complete media containing 12μCi ^{14}C acetate and the cells were pulsed for three hours. The lipids were subsequently extracted using a methanol:chloroform:water ratio of 1:2:0.65, separated by thin-layer chromatography (mobile phase 80:20:2 hexanes:ether:acetic acid), and quantified using a radioscanner. To determine which spot on the TLC plate represented free cholesterol, a free cholesterol standard was run on each plate and was visualized in an iodine chamber. For cholesterol synthesis measurements using charcoal stripped media, the method was as above except the pulse media contained charcoal stripped fetal bovine serum (Thermo Fisher, Waltham, MA) and 6μCi ^{14}C acetate.

Prenylation probe incorporation. To measure the incorporation of prenyl modifications, we incubated cells with a C15 alkyne isoprenoid that is a substrate of prenylation enzymes FTase and GGTase[141,142]. We subsequently used "click" chemistry to covalently attach a fluorescent reporter to the alkyne moiety and analyzed the samples by flow cytometry. Cells were incubated with 50 μM of the alkyne isoprenoid (C15)[141,142], in 2 mL of complete Dulbecco's Modified Eagle Medium for 24 hours. After incubation, cells were harvested, rinsed twice with phosphate buffered saline and fixed in 4% paraformaldehyde/PBS for 10 minutes at room temperature. Cells were permeabilized with 0.1% Triton X-100 in phosphate buffered saline for two minutes at room temperature followed by several PBS rinses. Cells were then suspended in a final volume of 100 μL in phosphate buffered saline containing 5-Fam-PEG-N3 (0.1 mM), tris(2-carboxyethyl)phosphine (TCEP, 1 mM), tris[(1-benzyl-1H-1,2,3-triazol-4-yl)methyl] amine (TBTA, 0.2 mM), $CuSO_4$ (1 mM). The cells were incubated with this mixture for one hour at room temperature. The cells were then washed with PBS and resuspended in 1.5mL of phosphate buffered saline for flow cytometry analysis. Ten thousand events (cell counts) were analyzed for each sample (performed in triplicate) using a BD FACSCalibur (BD Biosciences, Franklin Lakes, NJ). FlowJo (www.flowjo.com) was used to analyze and graph the data. To determine if ATG7 siRNA treated cells had a significantly higher median FITC intensity than negative control siRNA treated cells, a 95% confidence interval (p=0.05) for each median was calculated in R. Two medians are considered

significantly different if the 95% confidence intervals containing the two medians do not overlap.

Quantitative PCR. Total RNA was isolated using Trizol (Thermo Fisher, Waltham MA) as previously described.[143] Total RNA concentration was determined by absorbance measurement at 260nm on a NanoDrop 2000c (Thermo Fisher, Waltham, MA). cDNA was synthesized from 1µg total RNA using a Super Script Vilo kit (Thermo Fisher, Waltham MA). Real-time analysis was performed using the Applied Biosystems Step One qPCR System (Thermo Fisher, Waltham MA) and the Applied Biosystems SYBR Green PCR Master Mix (Thermo Fisher, Waltham MA). Quantification of the specific mRNA levels was calculated relative to the reference gene RPL32, using the $\Delta\Delta$CT method.[144] Primer sequences are listed in Supplementary Methods, Table 1.

SILAC labeling. An adapted procedure by Harsha *et al.* was used for this study.[145] SILAC media (Thermo Fisher, Waltham, MA) devoid of the essential amino acids lysine and arginine was supplemented with either the light (Thermo Fisher, Waltham, MA) or heavy (Sigma-Aldrich, St. Louis, MO) isotopic form of these amino acids (L-Lysine HCl, $^{13}C_6$, $^{15}N_2$ and L-Arginine, $^{13}C_6$, $^{15}N_4$; final concentration = 100µg/mL) to create light and heavy SILAC cultures, respectively. Dialyzed fetal bovine serum (Thermo Fisher, Waltham, MA) and the antibiotic gentamicin (Sigma-Aldrich, St. Louis, MO) were added to a final

concentration of 10% and 0.02%, respectively. Although five doubling times is considered to be sufficient for total incorporation of the SILAC amino acids[146] cells were cultured in SILAC media for approximately six to eight doubling times (three passages). The incorporation efficiency of SILAC amino acids was 99%.

To increase the number of identifications, this study included three separate and independent biological replicates of L6 rat myoblasts metabolically labeled using light and heavy SILAC cultures. In two of the three total biological replicates, the negative control siRNA treated cells were cultured in the light SILAC media and the ATG7 siRNA treated cells were cultured in the heavy SILAC media. For the third biological replicate, the labeling state was reversed.

Proteomics sample preparation and in-gel digestion. To reduce sample complexity and increase the number of protein identifications, cell lysates were subjected to subcellular fractionation to prepare a nuclear-enriched, organelle-enriched, and cytosolic fractions as follows. About 2,000,000 cells (confluency ~ 65%) of each SILAC-labeled cell culture were harvested and analyzed for protein content with a BCA assay (done according to manufacturer's instructions, Thermo Fisher, Waltham MA). The heavy and light SILAC-labeled cells were combined in a 1:1 protein ratio (a typical experiment yielded ~0.4 mg of protein). The cells were then resuspended in ice-cold isolation buffer (220mM mannitol, 70mM sucrose, 0.5mM EGTA, 2mM HEPES, pH 7.4, Acros Organics, Rockford,

IL) containing Halt Protease Inhibitor cocktail (#78425, Thermo Fisher, Waltham MA) before mechanical homogenization with a tight-fitting dounce homogenizer (clearance 0.0005-0.0025 inches). The cell homogenates were centrifuged at 600g for 10 minutes at 4°C. The pellet was collected as the nuclear-enriched fraction and the supernatant centrifuged at 10,000g for 10 minutes at 4°C, to produce a pelleted, organelle-enriched fraction. The supernatant was then concentrated in a YM-30 Micron centrifugal ultrafiltration device (30,000 NMWL, #42409, Millipore, Billerica, MA) and saved as the cytosolic fraction. The organelle-enriched pellet was incubated on ice for 10 minutes in 0.1 mg/mL trypsin in an isolation buffer devoid of protease inhibitor to decrease the level of cytoskeleton attached to the organelles[147] and then centrifuged at 10,000g for 10 minutes at 4°C. This pellet was the final organelle-enriched fraction.

Each fraction was denatured with Laemmli buffer (62.5mM Tris-HCl pH 6.8, 25% glycerol, 2% SDS, 0.01% Bromophenol Blue; #161-0737, Bio-Rad, Hercules, CA) and then separated by 1D SDS-PAGE (one lane per fraction) on a 12.5% Tris-HCl Criterion gel at a constant voltage of 200V (#345-0014, Bio-Rad, Hercules, CA). The proteins were stained with Coomassie blue according to manufacturer's instructions (#1610436, 1610438, Bio-Rad, Hercules, CA) followed by excision of 1mm wide bands (approximately 10 bands per lane) for subsequent in-gel digestion. The in-gel digestion protocol by Shevchenko *et al.*[148] was used with minor modifications. After concentration to dryness (Centrivap, Labconco,

Kansas City, MO), the peptides were reconstituted in a 5% acetonitrile solution with 0.5% formic acid.

LC-MS procedures. A modified method by Graumann *et al.* was used for LC-MS analysis.[149] The peptides were analyzed by an Eksigent nanoHPLC system (Dublin, CA) coupled to an Orbitrap Velos (Thermo Fisher, Waltham, MA) mass spectrometer. Eight microliters of each sample were loaded onto a Waters Symmetry C18 pre-column (Milford, MA) and subsequently eluted onto a fused silica capillary column (75 µm i.d., 10.5 cm length, packed in house with a C18 packing material). A PicoTipTM emitter was used (tip = 15±1 µm, #PF360-75-15-N-5, New Objective, Woburn, MA) for electrospray ionization. The peptides were eluted at a constant flow of 300 nL/min in a 140-minute linear gradient (5-60% acetonitrile with 0.1% formic acid), holding at 60% acetonitrile + 0.1% formic acid for 15 minutes at the end of the gradient. The spray voltage was set to 1.6 kV and the capillary temperature set to 300°C. Full survey scans (*m/z* 300-2000) were acquired in the Orbitrap (resolution of 60,000). The eight most intense ions from the survey scan were fragmented by collision-induced dissociation (normalized collision energy of 35.0) in the LTQ after accumulation of 10,000 ions in the Orbitrap full-scan acquisition (ITMS, minimum signal set to 500). The dynamic exclusion time was 30s and the lock mass calibration was enabled for the survey scans (lock masses were 371.101233 m/z and 445.120024 m/z). All data was acquired using Xcalibur software (Thermo, v2.1.0.1139).

Protein quantification and pathway analysis. Xcalibur (.raw format) files were submitted to MaxQuant (V1.4.1.2)[150] with the Andromeda search engine[151] for preprocessing (feature detection, generation of peak lists, and peptide quantification), protein identification (rat UniprotKB, 11,893 entries, release 2014_04 version), and protein quantification and validation to determine the heavy-to-light ratio (referred to hereafter as "H/L") of each SILAC-labeled protein (the protein ratio is the median of the peptide intensity ratios). For proteins identified in the replicate in which the labeling state was reversed, the inverse of the normalized H/L ratio was determined. To identify and correct for potential artifacts, proteins that had an inverse H/L ratio that was in the opposite direction from the H/L ratio found in other replicates were removed from further analysis. Parameters were set as follows: (i) the multiplicity was set to 2 with Arg10 and Lys8 set as the heavy labels, (ii) the enzyme was trypsin, (iii) carbamidomethyl was a fixed modification, (iv) oxidation of methionine and the loss of ammonia from the N-terminus of glutamine and asparagine were variable modifications, (v) the acceptable number of missed cleavages was 2, (vi) the mass deviation for monoisotopic precursor ions was 20 ppm, and (vii) the allowable mass deviation for MS/MS peaks was 0.5 Da. The false discovery rate (referred hereafter as "FDR") was set to 0.01 for both peptide and protein identification. Using a minimum of two peptides per protein, each protein was quantified with a peptide FDR of approximately 1% (Supplementary Table 2). When plotted against the

normalized H/L ratios, the variabilities of these proteins were largely random - there was no trend between variability and heavy/light ratio (data not shown). Normalization was done automatically in MaxQuant by setting the median of their logarithms to zero to correct for uneven protein loading in each LC-MS run. This correction assumes that the majority of proteins do not change in abundance between the control and treatment groups.[150] The posterior error probability (referred hereafter as "PEP") score for each protein was obtained from the product of peptide PEP scores, and is the probability that the peptide-spectra matches are incorrect.[152] Low PEP scores indicate a high certainty of peptide and protein identification. Searching against a decoy database allowed for the removal of contaminant proteins, but manual inspection of the peptide identifications revealed that a few non-contaminant proteins still contained contaminant peptides (see Supplementary Tables 1A, 1B, 1C for peptide information for each biological replicate). These proteins were eliminated as peptide contaminants would have skewed the quantification of such proteins. Benjamini-Hochberg analysis, with FDR <0.05 using protein Significance B (calculated using Perseus version 1.5.0.0), identified proteins with significant expression level changes with ATG7 siRNA treatment. The Significance B value serves as a ranked p-value taking into account the differences in protein abundances. Low abundance proteins were deemed less significant than highly abundant proteins with the same H/L ratio due to a higher statistical spread. Binning low abundance and high abundance proteins of similar H/L ratios

together to calculate significance (i.e. Significance B) narrows the statistical spread of the low abundance proteins.[150] These significantly changed proteins were then analyzed with IPA (Ingenuity® systems, www.ingenuity.com). The canonical pathways best represented by those proteins with a significant change in abundance were identified as those pathways with the highest p-scores.

Results

ATG7 knockdown increases free cholesterol level and conjugation of a prenylation probe. Transient knockdown of the ATG7 gene by siRNA transfection was used to inhibit autophagy and autophagy function was assessed using qPCR, visualization of giant mitochondria, and western blot. ATG7 siRNA treatment resulted in a significant 5-fold decrease in ATG7 mRNA (Supplementary Figure 2A). Giant mitochondria, a morphological marker of autophagy inhibition,[153,154] were observed in ATG7 siRNA treated cells (Supplementary Figure 2D), which suggests that autophagy is impaired in ATG7 siRNA treated cells. Autophagy flux is defined as the rate of degradation activity through the autophagy pathway[21], including the formation of LC3-II positive autophagosomes, fusion with lysosomes, and subsequent cargo release.[22] Autophagy flux is often quantified by monitoring the accumulation of LC3-II over time following treatment with inhibitors of autophagosome-lysosome fusion[21,22]. While treatment with bafilomycin A-1 resulted in accumulation of LC3-II in negative control siRNA treated cells (Supplementary Figure 2C), there was no

accumulation of LC3-II in ATG7 siRNA treated cells. This result suggests that ATG7 siRNA treatment inhibits autophagy flux.

To investigate whether ATG7 knockdown has an effect on the mevalonate pathway, we measured two products of the mevalonate pathway in cell lysates: free cholesterol level and protein prenylation. Free cholesterol refers to cholesterol in the cell that has not undergone further transformation into cholesterol esters. ATG7 siRNA treatment significantly increased the free cholesterol when compared with cells treated with the negative control siRNA (Figure 2A). In addition, the conjugation of prenyl groups to molecular targets was measured by flow cytometry to determine whether ATG7 knockdown leads to changes in protein prenylation. After incorporation of a C15 alkyne isoprenoid, click chemistry was used to label the C15 probe with a fluorophore and enable detection by flow cytometry (Supplementary Figure 3). ATG7 siRNA treated cells have a statistically significant increase in median fluorescent intensity compared to negative control siRNA-treated cells (Figure 2B). These findings point to increased conjugation of the prenylation probe on proteins when ATG7 is knocked down. Increased incorporation of the prenylation probe may suggest an increase in prenylation activity or insufficient endogenous pool of isoprenoids. An insufficient endogenous pool of isoprenoids may result from an overall decrease in the mevalonate pathway or from isoprenoids being diverted from protein prenylation to synthesize more cholesterol.

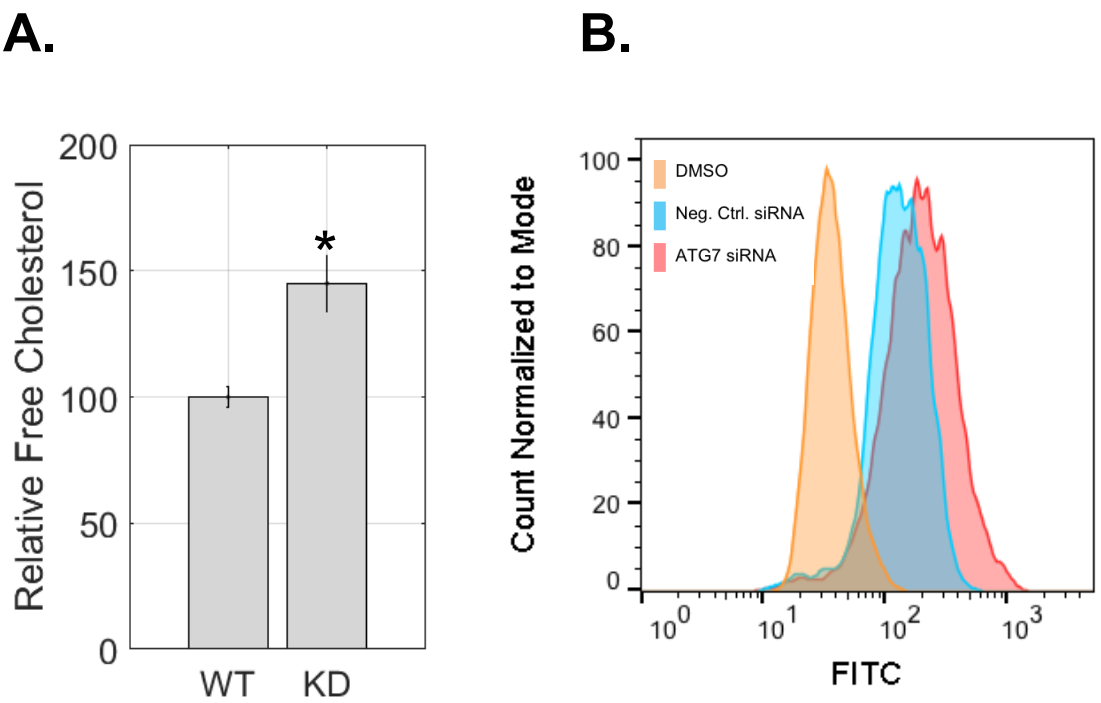

Figure 2. (A) Relative free cholesterol level in ATG7 siRNA treated (KD) and negative control siRNA treated (WT) cells. KD cells had an average 1.42 fold significant increase in free cholesterol compared to WT cells, p=0.043, n=3 biological replicates, error bars represent +/- SEM. **(B) Protein prenylation measurement in ATG7 siRNA treated and negative control siRNA treated cells.** The median fluorescent intensity in Atg7 siRNA treated L6 cells is significantly increased relative to that of negative control siRNA treated L6 cells. The 95% confidence intervals for median FITC intensity are [188, 193] for ATG7 siRNA treated cells and [127, 130] for negative control siRNA treated cells. This suggests ATG7 siRNA treatment results in an increase in incorporation of the prenylation probe (Supplementary Figure 3). Transfection was done as described in Supplementary Methods. *Data collected by Josh Ochocki.*

ATG7 knockdown changes cholesterol synthesis, dependent on dominant cholesterol source. From the free cholesterol and prenylation measurements only, it is unclear whether changes in the cholesterol synthesis pathway are responsible for the increase in cholesterol abundance and increase in conjugation of prenyl groups. Therefore, we sought to measure cholesterol synthesis in ATG7 siRNA treated cells. We quantified cholesterol synthesis in ATG7 siRNA and negative control siRNA treated cells by following the incorporation of ^{14}C acetate into synthesized cholesterol. ATG7 siRNA treatment significantly decreased the incorporation of ^{14}C acetate into synthesized cholesterol when compared with cells treated with the negative control siRNA (Figure 3A). We subsequently measured cholesterol synthesis in the absence of cholesterol in the media. In charcoal stripped media, the addition of ATG7 siRNA significantly increased the incorporation of ^{14}C acetate into synthesized cholesterol when compared with cells treated with the negative control siRNA (Figure 3B).

The free cholesterol measurements (Figure 2A) and cholesterol synthesis measurements (Figures 3A and 3B) together suggest that cholesterol abundance follows the opposite trend to cholesterol synthesis, suggesting additional regulation of the mevalonate pathway at the post transcriptional level. If increased incorporation of the C15 alkyne prenylation probe is a result of increased prenylation activity, endogenous isoprenoids may be directed towards

protein prenylation instead of squalene, which is consistent with the observed decrease in cholesterol synthesis. Alternatively, the decrease in cholesterol synthesis in complete media suggests an overall decrease in the mevalonate pathway, which would suppress availability of isoprenoids for protein prenylation, enabling increased incorporation of the C15 alkyne prenylation probe in ATG7 siRNA treated cells (Figure 2B).

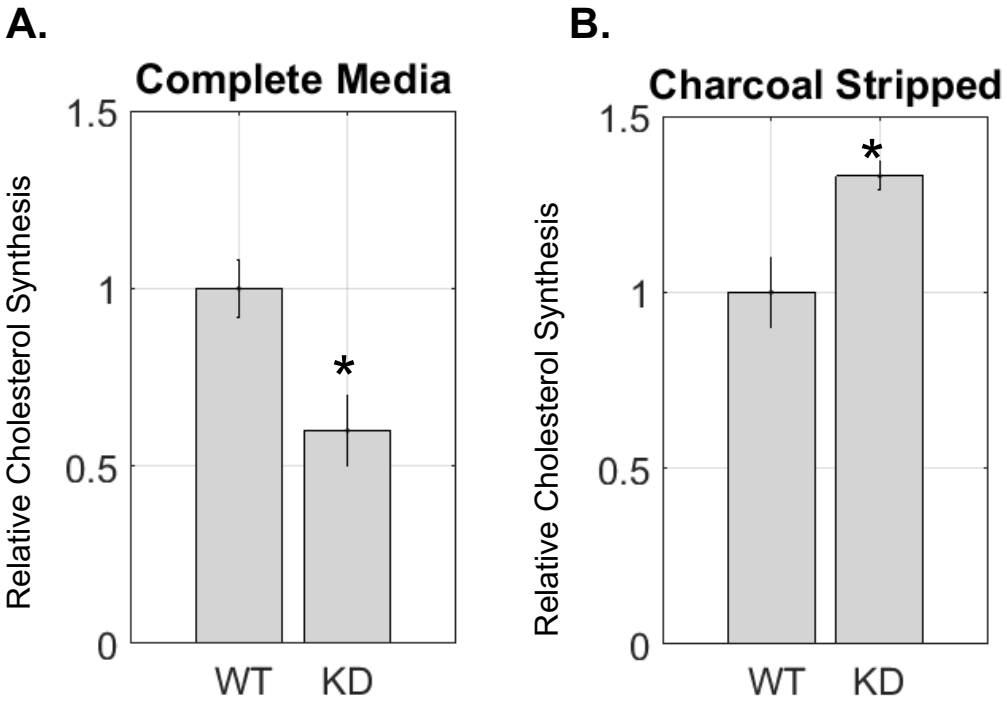

Figure 3. (A) Relative cholesterol synthesis in ATG7 siRNA treated (KD) and negative control siRNA treated (WT) cells, complete media. KD cells had an average 1.6 fold significant decrease in relative cholesterol synthesis compared to WT cells, p=0.036, n=3 biological replicates, error bars represent +/- SEM. **(B) Relative cholesterol synthesis in ATG7 siRNA treated (KD) and negative control siRNA treated (WT) cells, charcoal stripped media.** KD cells had an average 1.3 fold significant increase in relative cholesterol synthesis compared to WT cells, p=0.042, n=3 biological replicates, error bars represent +/- SEM.

ATG7 knockdown changes regulation of cholesterol synthesis genes. To determine whether conversion to squalene or the overall mevalonate pathway was decreased, we sought to determine the changes in the expression of the cholesterol synthesis genes responsible for and upstream of squalene formation. We measured the expression of HMG-CoA reductase (HMGCR), farnesyl diphosphate synthase (FDPS), and farnesyl diphosphate transferase type 1 (FDFT) using qPCR. Both HMGCR and FDPS are upstream of FDFT, and the location of each of these proteins in the cholesterol synthesis pathway is illustrated in Figure 1. HMGCR encodes for HMG-CoA Reductase (HMGCR), which catalyzes the rate limiting step in cholesterol synthesis.[155] FDPS encodes for farnesyl pyrophosphate synthase (FPPS), the protein responsible for catalyzing the formation of farnesyl pyrophosphate, which is a substrate for protein prenylation. FDFT encodes for squalene synthase (SQS), which catalyzes the formation of squalene, representing the first committed step of cholesterol synthesis. In complete media, ATG7 siRNA treatment significantly lowered the mRNA abundance of the genes FDPS and HMGCR, and ATG7 siRNA treatment did not change the mRNA abundance of FDFT (Figure 4). If decreased gene expression is reflected in a decrease in the activity of their respective proteins, the reduction in HMGCR expression reduces overall flux through the mevalonate pathway and the reduction in FDPS expression reduces the synthesis of isoprenoids. FDFT expression was not changed, thus suggesting that the conversion of isoprenoids to squalene was not changed. Consistent with

decreased cholesterol synthesis, (Figure 3A) these results support the scenario that an insufficient endogenous isoprenoid pool is causing the increased incorporation of the C15 alkyne isoprenoid observed in the ATG7 siRNA treated cells (Figure 3B).

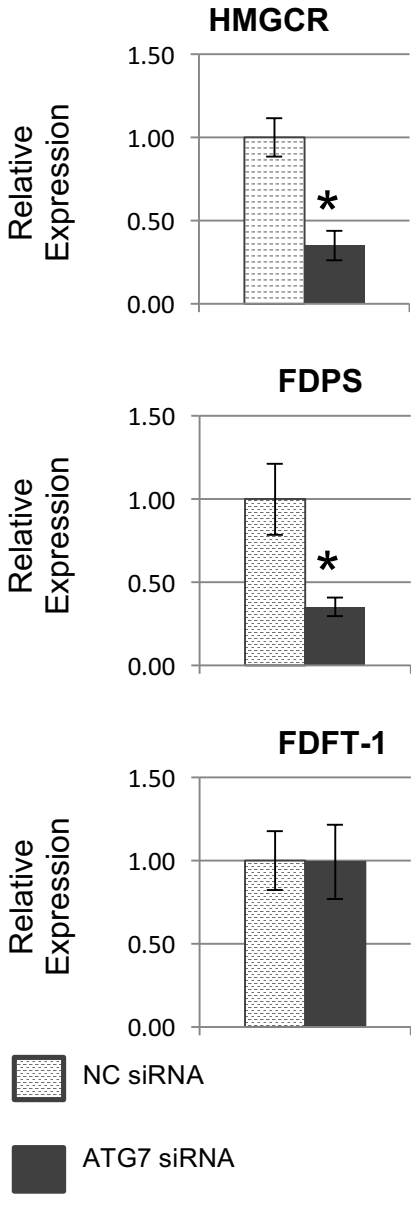

*p < 0.05

Figure 4. Relative cholesterol synthesis gene expression in ATG7 siRNA treated and negative control siRNA treated cells. ATG7 siRNA treated cells had a 2.8 fold significant decrease in HMGCR gene expression compared to negative control siRNA treated cells, p=0.018. ATG7 siRNA treated cells had a 2.9 fold significant decrease in FDPS gene expression compared to negative control siRNA treated cells, p=0.026. ATG7 siRNA treated cells had no significant change in FDFT gene expression compared to negative control siRNA treated cells. Each plot includes data from n=3 biological replicates, and error bars represent +/- SEM.

Unbiased quantitative proteomics indicates that cholesterol synthesis proteins are increased in abundance with ATG7 siRNA treatment. From the observations presented above, it appears that that overall flux through the mevalonate pathway was decreased upon ATG7 siRNA treatment in complete media, despite an increased cellular free cholesterol level, suggesting additional regulation of the mevalonate pathway at the post transcriptional level. In order to clarify whether the mevalonate pathway gene expression levels are reflected in mevalonate pathway protein abundance and function, we sought to quantify the abundance of proteins in the cholesterol biosynthesis pathway. Knowing the limitations of western blots,[156,157] we decided to pursue a unbiased proteomics study.

We quantified the proteomes from ATG7 siRNA treated and negative control siRNA treated cells in biological triplicate using SILAC (Stable Isotope Labeling with Amino Acids in Cell Culture). We quantified 4,451 total proteins across all three biological replicates, and 1,898 of the total proteins were quantified in all three biological replicates, resulting in ~57% overlap in identifications between the three data sets (Supplementary Figure 4). After performing a Benjamini-Hochberg adjustment,[158] we found that 95 non-redundant proteins were significantly changed in abundance in ATG7 siRNA treated cells relative to negative control siRNA treated samples (Supplementary Table 3). Validation of

the data is demonstrated by the shape of the distribution of H/L ratios for all proteins that were quantified (Supplementary Figure 5). A second validation of the data is a volcano plot of statistical significance (Significance B) values versus H/L ratios (Supplementary Figure 6).

We used Ingenuity Pathways Knowledge Base (Ingenuity® Systems, www.ingenuity.com) to discern possible associations of metabolic pathways with the ATG7 siRNA treatment. Mapping of proteins with significantly changed abundance upon Atg7 siRNA treatment (Supplementary Table 3) to canonical pathways with Ingenuity Pathway Analysis (IPA) yielded 17 canonical pathways and sub-pathways with high statistical significance (Table 1 and Supplementary Table 5). The most significant pathways were related to cholesterol synthesis through the mevalonate pathway, fatty acid synthesis, and nucleotide synthesis. Several pathways directly represent the synthesis of cholesterol (Superpathway of Cholesterol Biosynthesis, Cholesterol Biosynthesis I-III), or the synthesis of mevalonate pathway intermediates upstream of cholesterol (Mevalonate Pathway 1, Trans-Trans-Farnesyl Diphosphate Biosynthesis, Superpathway of Geranylgeranyldiphosphate Biosynthesis 1, Epoxysqualene Biosynthesis, Zymosterol Biosynthesis). Taken together, the significantly increased proteins involved in these pathways represent sixteen of the twenty-four enzymes in the mevalonate pathway that are responsible for the synthesis of cholesterol from acetyl-CoA (Figure 5 and Table 2). While protein abundance measurements do

not indicate function, the cholesterol synthesis assay shows the opposite trend. The increased abundance of proteins involved in cholesterol synthesis and the decrease in cholesterol synthesis (Figure 3A) together suggest that impaired autophagy results in the accumulation of subcellular components where these key proteins reside.

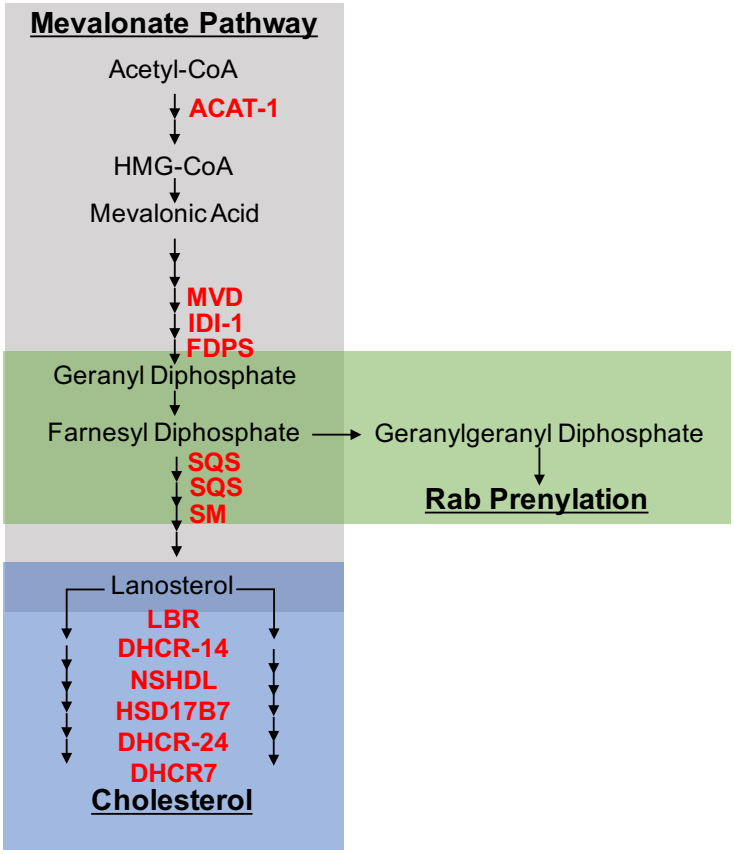

Figure 5. Significantly changed proteins mapped to a diagram of the mevalonate pathway. Protein names written in red were those found significantly increased in abundance in the unbiased proteomics study, representing 16 of the 24 proteins involved in this pathway. Transfections prior to MS analysis was performed as described in Supplementary Methods. *Data collected by Michelle Kuhns.*

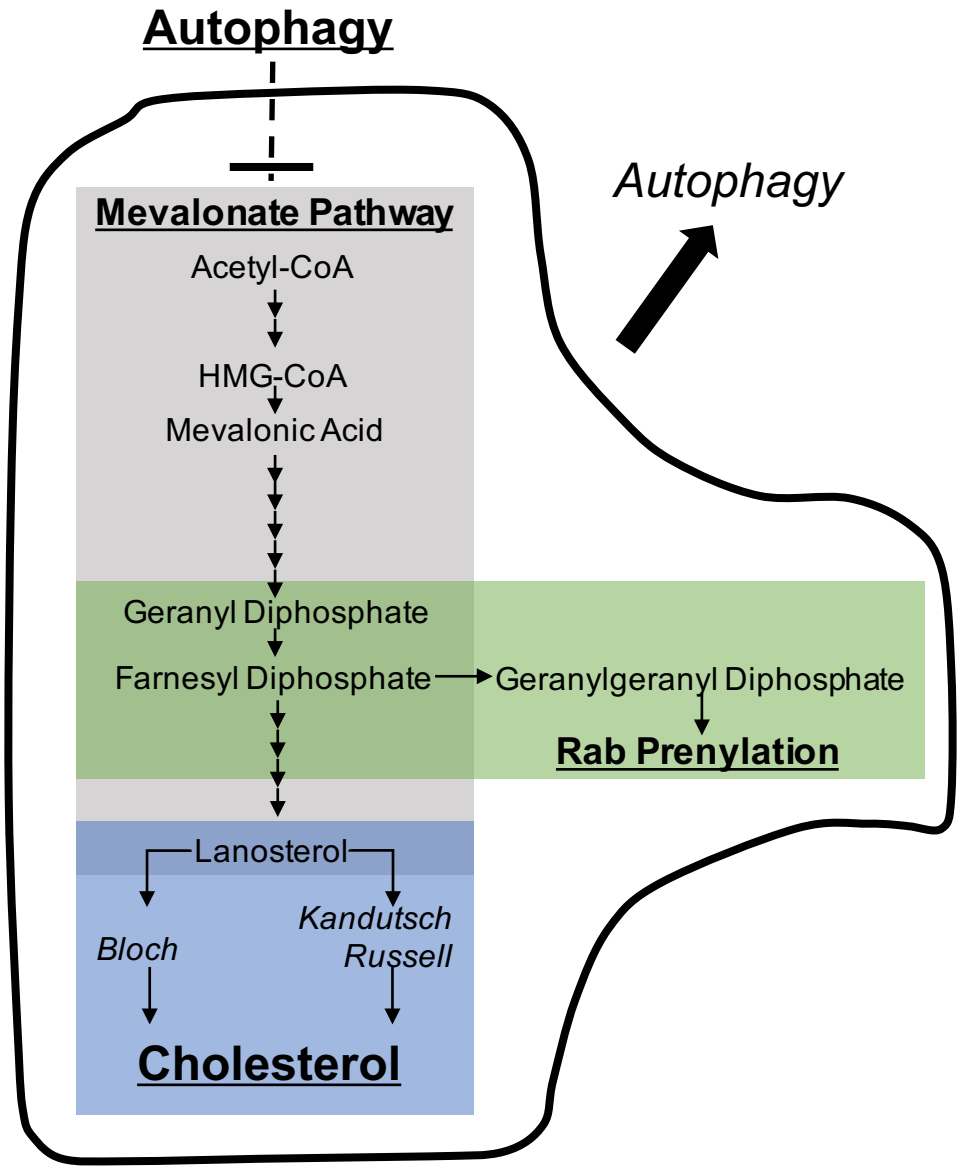

Figure 6. Working model of mevalonate pathway regulation by autophagy.

TABLE 1

Canonical Pathway	-log (p-value)	Genes in Network
Superpathway of Cholesterol Biosynthesis	23	FDPS,MVD,FDFT1,SQLE,DHCR7,NSDHL,ACAT2,DHCR24,IDI1,HSD17B7,MSMO1,CYP51A1,LBR
Cholesterol Biosynthesis I, II, III	18.2	SQLE,FDFT1,NSDHL,DHCR7,DHCR24,HSD17B7,MSMO1,CYP51A1,LBR
Zymosterol Biosynthesis	10.9	NSDHL,HSD17B7,MSMO1,CYP51A1,LBR
Oleate Biosynthesis II (Animals)	6.47	SCD,Scd2,FADS2,FADS1
Superpathway of Geranylgeranyldiphosphate Biosynthesis I (via Mevalonate)	5.96	MVD,FDPS,ACAT2,IDI1
Epoxysqualene Biosynthesis	4.65	SQLE,FDFT1
Mevalonate Pathway I	4.54	MVD,ACAT2,IDI1
γ-linolenate Biosynthesis II	4.17	FADS2,ACSL1,FADS1
Pyrimidine Deoxyribonucleotides De Novo Biosynthesis I	3.82	TYMS,DUT,RRM2
Trans, trans-farnesyl Diphosphate Biosynthesis	3.65	FDPS,IDI1

Table 1. Summary of canonical pathways significantly affected by ATG7 siRNA treatment. The canonical pathways listed above set forth the molecules with significant changes in abundance and that were determined to be significantly affected by Atg7 siRNA treatment ($p < 0.0002$ or -log(p-value) > 3.65). These and additional significant pathways ($p < 0.01$ or -log(p-value) > 2) are listed in Supplementary Table 5. *Data collected by Michelle Kuhns.*

TABLE 2

Protein IDs	Protein Names	Gene Names	H/L Normalized	PEP	Peptides
Q5XI22	Acetyl-CoA acetyltransferase, cytosolic (ACAT2)	Acat2	1.61	3.1E-118	13
Q64654	Lanosterol 14-alpha demethylase (LDM)	Cyp51a1	1.79	5.5E-122	13
Q5BQE6	Delta(24)-sterol reductase (DHCR24)	Dhcr24	2.02	2.5E-09	3
Q9Z2Z8	7-dehydrocholesterol reductase (DHCR7)	Dhcr7	1.88	3.2E-33	5
Q02769	Squalene synthase (SQS)	Fdft1	2.56	2.6E-41	7
P05369	Farnesyl pyrophosphate synthase(FPPS)	Fdps	1.75	4.4E-110	14
Q62904	3-keto-steroid reductase (HSD17B7)	Hsd17b7	1.98	5.2E-73	7
O35760	Isopentenyl-diphosphate Delta-isomerase 1 (IDI-1)	Idi1	2.28	7.3E-30	3
O35532	Methylsterol monooxygenase 1 (MSMO-1)	Msmo1	1.79	3.2E-43	6
Q62967	Diphosphomevalonate decarboxylase (MVD)	Mvd	1.71	8.1E-28	5
Q5PPL3	Sterol-4-alpha-carboxylate 3-dehydrogenase, decarboxylating (NSDHL)	Nsdhl	2.19	1.7E-50	10
P52020	Squalene monooxygenase (SM)	Sqle	1.94	5.3E-28	4

Table 2. ATG7 siRNA treatment resulted in increased abundance of proteins involved in the mevalonate pathway. Proteins listed above had a significant change in abundance in at least one of the three replicates (Benjamini-Hochberg method, p = 0.05). Their corresponding protein names and abbreviations, gene names, H/L ratios, PEP scores, and number of assigned peptides are also listed. For proteins that were identified as significantly changed in more than one biological replicate (ACAT2, FPPS, IDI-1), only the most significant change in abundance is reported here. All significantly changed proteins with Atg7 siRNA autophagy inhibition appears in the Supplementary Table 2. *Data collected by Michelle Kuhns.*

Discussion

The goal of this work was to investigate how autophagy controls two products of the mevalonate pathway, cholesterol and protein prenylation. The best characterized role for the mevalonate pathway in controlling autophagy is through Rab prenylation, which is required for autophagy in several model systems.[87–90] In addition to *de novo* synthesis via the mevalonate pathway, free cholesterol can be obtained from liver lipid droplets via selective autophagy.[7–9] We hypothesize that autophagy, the mevalonate pathway, and cholesterol uptake work in conjunction to regulate free cholesterol levels. Despite Rab prenylation and selective autophagy of lipid droplets, and the known connections between the mevalonate pathway and autophagy highlighted above, there was no investigation into the regulation of cholesterol synthesis by autophagy prior to this study.

In-vitro[137–139] and mouse[140] models of decreased ATG7 expression have been used to investigate inhibited autophagy. ATG7 gene expression has been modified in vitro[137–139] and in mice[140] to perturb autophagy. Myoblasts are immortalized mononucleated muscle precursor cells that have the ability to differentiate into myotubes and form single muscle fibers.[136] Myoblasts also provide an in-vitro model system associated with skeletal muscle in which gene expression can be altered by siRNA[159,160] or CRISPR/Cas9.[161] As the goal of this study was to investigate how autophagy controls cholesterol and protein

prenylation, we found that ATG7 siRNA treatment resulted in an increased free cholesterol level in L6 rat myoblasts, and we subsequently investigated the effect of ATG7 knockdown on the regulation of the mevalonate pathway.

We assessed autophagy flux in ATG7 siRNA treated and negative control treated cells at the genetic, morphological, and protein levels. We observed a 5.0 fold decrease in ATG7 mRNA and accumulation of giant mitochondria in cells treated with ATG7 siRNA compared to negative control treated cells. Both of these observations provided strong evidence for inhibited autophagy in our model system. The measurement of LC3-I and LC3-II in the presence of lysosomal inhibitors by western blot is a suitable method for determining whether or not flux is occurring through the autophagy pathway.[24] Treatment with bafilomycin A-1, and assessment of LC3-II formation over time, indicated that autophagy flux is impaired with ATG7 siRNA treatment. Taken together, the qPCR, giant mitochondria, and western blotting presented conclusive evidence that ATG7 is required for autophagy in L6 myoblasts. This interpretation is also consistent with previous reported phenotypes resulting from ATG7 perturbation.[137–140]

On the basis of ATG7 knockdown inhibiting autophagy flux, we propose a modified working model for regulation of the mevalonate pathway by autophagy in L6 rat myoblasts (Figure 6). Free cholesterol has a steady state pool maintained by uptake, synthesis through the mevalonate pathway and autophagy

of lipid droplets. Autophagy is a third source of cellular cholesterol, and autophagy inhibition results in a higher steady state pool of free cholesterol. This turn triggers negative feedback of cholesterol synthesis genes through SREBP-2 thus reducing overall flux though the mevalonate pathway. Decreased flux through the mevalonate pathway enables increased incorporation of the probe used to monitor prenylation, while inhibition of the autophagy machinery also results in the accumulation of proteins involved in the mevalonate pathway, fatty acid synthesis, and nucleotide synthesis. In summary, our data suggest that autophagy plays a role in mediating cholesterol homeostasis.

The decreased FDPS and HMGCR gene expression seen with ATG7 siRNA treatment may be a result of the increased free cholesterol pool seen in ATG7 knockdown cells. This is consistent with prior knowledge of SREBP mediated negative feedback of the mevalonate pathway. Negative feedback regulation of the cholesterol synthesis pathway, in which free cholesterol inhibits transcription of cholesterol synthesis genes, proceeds through sterol regulatory element binding protein (SREBP) transcription factors.[61,162] FDPS, HMGCR, and FDFT are targets of the sterol regulatory element binding protein 2 (SREBP-2), a sterol-sensing transcription factor that has been well documented as a master regulator of cholesterol synthesis.[62] The lack of change in FDFT-1 expression is inconsistent with SREBP-2 mediated negative feedback of the mevalonate pathway. Unlike FDPS and HMGCR, FDFT has two binding sites for SREBP-2,

requiring two transcription factors to bind and strongly activate this gene in order to commit to cholesterol synthesis.[163,164] As FDFT encodes for squalene synthase (SQS), the protein responsible for the first committed step in cholesterol synthesis, our gene expression observations suggest that genes downstream of this control point are subject to an additional level of regulation beyond SREBP-2 in cells associated with skeletal muscle.

We hypothesize that the increased incorporation of the prenylation probe in ATG7 siRNA treated cells is the result of an insufficient endogenous isoprenoid pool (Figure 6). We saw a significantly higher incorporation of the prenylation probe in ATG7 siRNA treated cells compared to the negative control treated cells. Typically, treatment with the C15 alkyne probe is done in the presence of a statin to suppress endogenous isoprenoid production in order to favor incorporation of the C15 alkyne as prenylation modifications.[141,142,165] However, the ability of statins to induce autophagy has been documented in multiple model systems.[166–169] Thus we did not include a statin in this study. We observed significantly higher incorporation of the prenylation probe without suppressing the endogenous pool of isoprenoids with statin treatment. This supports our hypothesis that ATG7 siRNA treated cells have an insufficient endogenous pool of isoprenoids.

The gene expression changes suggest that the mevalonate pathway is downregulated, despite increased abundance of cholesterol synthesis proteins and increased free cholesterol abundance. This suggests that the increased abundance of proteins in the mevalonate pathway is not dictated by gene expression changes. If the proteins in the mevalonate pathway were functional, we would have seen an increase in cholesterol synthesis (Figure 2A). If increased protein abundance is reflective of stimulation of metabolic pathways, the increased abundance in proteins involved in the mevalonate pathway reported in the unbiased proteomics study may be reflective of a stimulation in the mevalonate pathway, causing the increased free cholesterol pool we observed in the ATG7 siRNA treated cells.

Several scenarios could account for the increased protein abundances seen in this study. One explanation is that ATG7 siRNA impairs bulk protein degradation, resulting in accumulation of proteins from a diverse set of metabolic pathways. This is consistent with our finding of the increased abundance of proteins involved in a number of pathways, including the mevalonate pathway, fatty acid synthesis, and nucleotide synthesis. Proteins involved in the mevalonate and associated pathways are located at the ER, which is the site of cholesterol synthesis[170] and the ability of autophagy to turn over the ER is known as ER-phagy.[171–174] Therefore, our observations support a decrease in the selective autophagy machinery normally employed to break down ER resident mevalonate

pathway proteins. The proteomics observations also support the idea that proteins in the mevalonate pathway are non-functional, or that there is regulation in the limiting step of the mevalonate pathway.

Overall, our work is the first demonstration of ATG7 knockdown regulating the mevalonate pathway and introduces a new avenue for investigation into the basic mechanisms governing cholesterol homeostasis in cell model systems associated with skeletal muscle. Additional investigations are needed to confirm our working model of how autophagy regulates the mevalonate pathway. The model should be refined to include other components that regulate free cholesterol abundance, including cholesterol uptake, reverse cholesterol transport, and cholesterol esterification. Assessment of SREBP-2 activity will confirm negative feedback in the regulation of cholesterol synthesis genes. To confirm that ATG7 siRNA treatment decreases mevalonate pathway flux and an insufficient level of endogenous isoprenoids enhances incorporation of prenyl modifications, flux through the mevalonate pathway and endogenous isoprenoid pool should be quantified using targeted metabolomics. To further elucidate the effect of ATG7 knockdown on autophagy and protein turnover, selective macrolipophagy and ER-phagy measurements are needed. Future studies will help further refine autophagy's contribution to cholesterol homeostasis in cells associated with skeletal muscle.

Chapter 5: Conclusions and Future Directions

Katherine Muratore wrote this chapter and illustrated all figures.

1. Overall Conclusions

The work described in this thesis investigated the central hypothesis that autophagy contributes to cholesterol abundance through macrolipophagy and regulation of cholesterol synthesis in aging muscle tissue. The objectives of this work were to develop new methods for individual macrolipophagy organelle analysis in tissues, to determine age associated changes in lipid droplet size, and to determine the role of autophagy in regulating cholesterol synthesis.

At the onset of this work, there were no suitable techniques to measure macrolipophagy. Such a technique was required to investigate the central hypothesis. In order to address this issue, the work described in Chapter 2 resulted in a new method to analyze individual autophagy organelles from tissues by using capillary electrophoresis with laser induced fluorescent detection (CE-LIF). Fluorophore conjugated anti-LC3 antibodies were used to label endogenous LC3 on autophagy organelles isolated from murine liver tissue prior to CE-LIF analysis. Antibody labeling was reproducible and specific to autophagy organelles, which provided a method that is capable of detecting changes in a known model system of impaired autophagy. This method is both the first demonstration of fluorophore conjugated antibodies as individual organelle labels for CE-LIF, and the first application of individual organelle CE-LIF to measure the properties of autophagy organelles isolated from tissue. This method can be expanded in the future with labels for lipid droplets in order to selectively monitor

macrolipophagy (Future work, Section 2C), and to determine the contribution of macrolipophagy to cholesterol abundance.

The available techniques to work with lipid droplets are limited. As described in the central hypothesis, regulation of lipid droplet size plays a critical role in cholesterol abundance through macrolipophagy. To address this issue, the work described in Chapter 3 is the application of Nanoparticle Tracking Analysis (NTA) to measure lipid droplet size. An NTA instrument was suitable for lipid droplet size measurements. It was used to evaluate lipid droplet preparation stability and compare the relative size distributions of lipid droplets from adult and geriatric mouse liver tissues. The work described in Chapter 3 revealed age-related decreases in lipid droplet size, and is the first measurement of lipid droplet size within a model system of aging. Size regulation of cholesterol depots in lipid droplets may be a contributing third source of cellular cholesterol, and NTA can be used for future studies on the regulation of lipid droplet size in any cell or tissue model system of interest.

To determine if autophagy contributes to cholesterol abundance through macrolipophagy in aging muscle, the effect of altered autophagy on cholesterol synthesis in myoblasts was investigated. Chapter 4 reviewed the existing working model for regulation of the mevalonate pathway by autophagy in myoblasts (Chapter 4, Figure 6). In the proposed model, the steady state pool of free

cholesterol, maintained by synthesis though the mevalonate pathway, uptake, and macroliophagy, is increased upon autophagy inhibition. According to the revised working model, the higher steady state pool of free cholesterol subsequently triggers negative feedback of cholesterol synthesis genes. This has the effect of reducing overall flux though the mevalonate pathway and increasing incorporation of prenylation modifications. Inhibition of the autophagy machinery also resulted in the accumulation of proteins involved in the mevalonate pathway, fatty acid synthesis, and nucleotide synthesis. Overall, Chapter 4 clarified the contribution of autophagy to cholesterol abundance and provided a basis for subsequent study into the role of macrolipophagy in cholesterol homeostasis. Future work will investigate changes to the cholesterol uptake, mevalonate pathway intermediates and ER-phagy that occur with the inhibition or blockage of autophagy (Future Work, Section 2D).

In conclusion, this thesis provides new evidence of the contribution of autophagy to cholesterol abundance at the subcellular level. Further development of the individual organelle measurements described in this work will need to be expanded to measure autophagy flux and macrolipophagy flux in aging tissue. The current working model for regulation of the mevalonate pathway by autophagy will be further refined by future investigations that study the effects of the additional inputs that foster cholesterol abundance and regulate the mevalonate pathway. The results of those studies will clarify the contribution of

macrolipophagy to overall cholesterol homeostasis in aging tissue. This thesis suggests for the first time that autophagy contributes to cholesterol abundance through macrolipophagy and regulation of cholesterol synthesis in muscle cells. Future work will further refine the contribution of autophagy to cholesterol abundance by selectively monitoring macrolipophagy and investigating the changes in cholesterol homeostasis that occur with inhibition or blockage of autophagy.

2. Future Directions

2A. Introduction

The work described in previous chapters of this thesis points the direction toward future developments that will broaden the application of the new techniques developed in this work for use in conjunction with additional experiments to define the contribution of autophagy to cholesterol homeostasis. To further advance the work in this thesis, it is imperative to develop additional tools to selectively monitor autophagy flux and macrolipophagy flux. It is also critical to investigate changes in cholesterol uptake, mevalonate pathway intermediates, and ER-phagy that occur with inhibition or blockage of autophagy. Sections 2 and 3 of this chapter describe CE-LIF approaches to measure autophagy flux and macrolipophagy flux, respectively. Section 4 of this chapter describes cholesterol uptake measurements, mevalonate pathway intermediate measurements, and ER-phagy flux measurements. Completion of these proposed experiments will advance understanding of how macrolipophagy contributes to cholesterol homeostasis.

2B. Measurement of Autophagy Flux by CE-LIF

Autophagy of lipid droplet cholesterol depots, through size or cholesterol abundance, may be a contributing third source of cellular cholesterol in skeletal muscle. Thus, it is critical to assess autophagy flux in primary myoblasts from adult and geriatric mice. The establishment of a CE-LIF based method for the analysis of antibody labeled autophagy organelles, described in Chapter 2, is the

first step towards developing a method for monitoring autophagy flux. CE-LIF of individual autophagy organelles provides a snapshot of the autophagy organelles present in a sample, but is inadequate to measure flux. Autophagy flux is the rate of degradation activity through the autophagy pathway[21] and is defined by the formation of LC3-II positive autophagosomes, fusion with lysosomes, and subsequent cargo release.[22] To quantify autophagy flux, the rate of formation and degradation of LC3-II positive organelles needs to be measured over time.

The method described in Chapter 2 used DyLight488 conjugated anti-LC3-II antibodies to label autophagy organelles prior to CE-LIF analysis. To assess autophagy flux in skeletal muscle myoblasts by CE-LIF, the number of DyLight488 positive organelles can be measured with a vinblastine treatment to accumulate autophagy organelles. Vinblastine destabilizes the cytoskeleton, preventing autophagosome to lysosome fusion[175]. Autophagy flux can then be calculated as the change in number of DyLight488 positive events over the time that the vinblastine treatment lasted. When compared with a control sample, samples with enhanced autophagy flux will have a higher number of events over time, and samples with impaired autophagy flux will have a lower amount of events over time. CE-LIF autophagy flux measurements should be performed in ATG7 siRNA treated myoblasts to further clarify the effect of ATG7 knockdown on autophagy flux. In addition, this method can be applied to primary myoblasts from adult and geriatric mice to document age-related changes in skeletal muscle autophagy flux.

2C. Selective Monitoring of Macrolipophagy Flux

Macrolipophagy is one of several forms of selective autophagy. Individual organelle measurements are needed to determine what fraction of autophagy organelles are associated with lipid droplets. That will determine the contribution of macrolipophagy to cholesterol abundance in aging muscle. LC3-II is the most commonly employed autophagy marker, and is found on phagophores, autophagosomes, and autolysosomes.[20] The method described in Chapter 2 is inadequate to distinguish amongst what type of cargo is associated with each LC3-II positive autophagy organelle. A combination of the LC3-II label with those for additional organelle types will enable the measurement of organelles involved in selective autophagy of other organelle types. The CE-LIF instrument used in Chapter 2 (pictured in Chapter 1, Figure 1) has the capability to detect two fluorophores simultaneously[71,72,80], including DyLight488 (excitation maximum 493nm, emission maximum 518nm) and an additional fluorophore conjugated antibody labeling a separate organelle (compatible with 488nm or 532nm excitation lasers, emission > 560nm).

To adapt the method discussed in Chapter 2 to measure LC3-II positive organelles associated with lipid droplets (LDs) in skeletal muscle myoblasts, LDs could be fluorescently stained with LipidTox Red (excitation maximum 577nm, emission maximum 609nm) and detected simultaneously in the home-built two-channel CE instrument.[71,72,80] DyLight488 positive events will represent

autophagy organelles and LipidTox Red labeled organelles will represent lipid droplets and dual labeled events will be representative of LDs inside autophagy related organelles. In order to monitor macrolipophagy flux, the number of dual labeled events can to be monitored as a function of time following vinblastine treatment. As with overall autophagy flux measurements, macrolipophagy measurements should be applied to ATG7 siRNA treated myoblasts, as well as primary myoblasts from adult and geriatric mice to clarify the role of macrolipophagy in maintaining lipid homeostasis in aging muscle.

Preliminary capillary cytometry data suggests that it is possible to characterize the properties of individual lipid droplets. LipidTox Red labeled droplets were delivered into a fused-silica capillary by 10kPa pressure and detected by LIF (Figure 1). In the resulting flow-gram, each spike is representative of an individual lipid droplet. This data represents the first LIF detection of Lipid Tox Red labeled individual lipid droplets.

Several challenges to the analysis of lipid droplets due to their unique biophysical characteristics can be met with future technical development. Two current challenges are (i) the floating of lipid droplets to the top of the capillary, and (ii) the interacting of lipid droplets with the capillary walls. Redesigning the CE-LIF instrument layout can be done to address lipid droplet floating. With a density less than that of water (specific gravity 0.92 g/cm^3), lipid droplets float in aqueous

buffer. Additional methods for modification of capillary coatings can be explored to reduce the absorption of lipid droplets to the capillary walls. Physical polyvinyl alcohol coating has been used to reduce the interaction between organelles and silanol groups on the capillary walls.[69,72,78,176] In a polyvinyl alcohol coated capillary, lipid droplets did not migrate towards the LIF detector, suggesting they are interacting with the capillary wall (unpublished observations). A future goal should be to find a stable capillary coating that does not interact with lipid droplets. A viable alternative is covalent coating with poly(acryloaminopropanal), which has been previously used in the analysis of individual liposomes by CE-LIF.[73] Therefore, future lipid droplet experiments using covalently coated capillaries have a high likelihood of success.

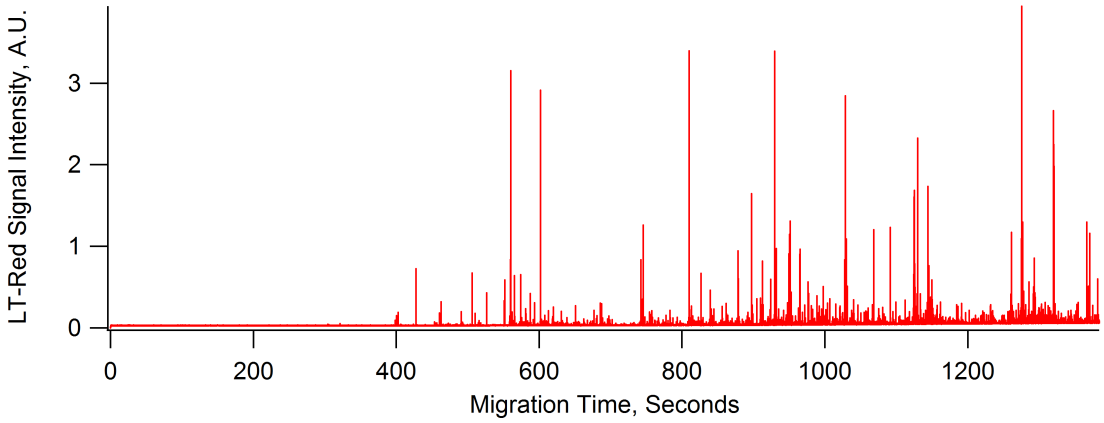

Figure 1. Flow-gram of Lipid Tox Red Labeled Lipid Droplets. Lipid droplets isolated from mouse liver were labeled with (1:200 v/v) Lipid Tox Red and analyzed by capillary cytometry. Parameters are: (1) Buffer, 250mM Sucrose, 10mM HEPES, pH 7.2. (2) Capillary, 30um inner-diameter uncoated fused silica (3) Detection, fluorescence 635df55 band pass filter (4) Delivery, 10kPA pressure.

2D. Confirmation of the Regulation of the Mevalonate Pathway by Autophagy

The experiments discussed in Chapter 4 resulted in a modified model for the regulation of the mevalonate pathway by autophagy. Although overall flux through the mevalonate pathway appears to be reduced, autophagy-inhibited L6 rat myblasts possess an accumulation of proteins involved in the mevalonate pathway, fatty acid synthesis, and nucleotide synthesis, as well as an increased steady state level of free cholesterol. The decreased flux through the mevalonate pathway promotes incorporation of prenylation modifications, while the increased free cholesterol induces negative feedback of cholesterol synthesis genes. Areas of this proposed model that need further investigation to test the current hypothesis are (i) maintenance of the steady state cholesterol pool, (ii) flux through the mevalonate pathway, and (iii) regulation of protein abundance by autophagy.

To clarify the source of the increased free cholesterol pool, reported in Chapter 4 (Figure 2), that occurred with autophagy inhibition, cholesterol degradation, cholesterol uptake and macrolipophagy need to be measured in addition to cholesterol synthesis. Despite an increase in free cholesterol, a decrease in cholesterol synthesis occurred in complete media and an increase in cholesterol synthesis occurred in cholesterol free media (Chapter 4, Figure 3). Impaired autophagy may reduce the rate of cholesterol degradation in cells. In complete media, cholesterol uptake may be accelerated to compensate for reduced flux

through the mevalonate pathway and impaired autophagy. In the cholesterol free media, the cell is forced to upregulate the mevalonate pathway to provide additional cholesterol in the absence of cholesterol in the media and functioning autophagy. Therefore, measurements of cholesterol degradation, cholesterol uptake and macrolipophagy in ATG7 knockdown autophagy inhibited cells are required. Measurement of macrolipophagy flux can proceed as discussed in the previous section. Experiments to measure cholesterol uptake are described below.

Preliminary data suggests that cholesterol uptake may be measured by microscopy. ATG7 siRNA and negative control siRNA cells were treated with NBD (green fluorophore) conjugated cholesterol and observed by confocal microscopy for 60 minutes. An image was taken every 5 minutes over the 60 minute period, and the mean pixel intensity per cell in three biological replicates was plotted versus time (Figures 2 and 3).

Due to the variation in fluorescence response among the biological replicates, these results were inconclusive. Several improvements could be made to improve the methodology of this experiment. Because each image did not capture the same z-position, this was likely a source of error. In addition, a lower magnification can be used to image a greater number of cells in each biological

replicate. Also, an area of the cell monolayer with low confluency must be selected to enable correct computational segmentation of individual cells.

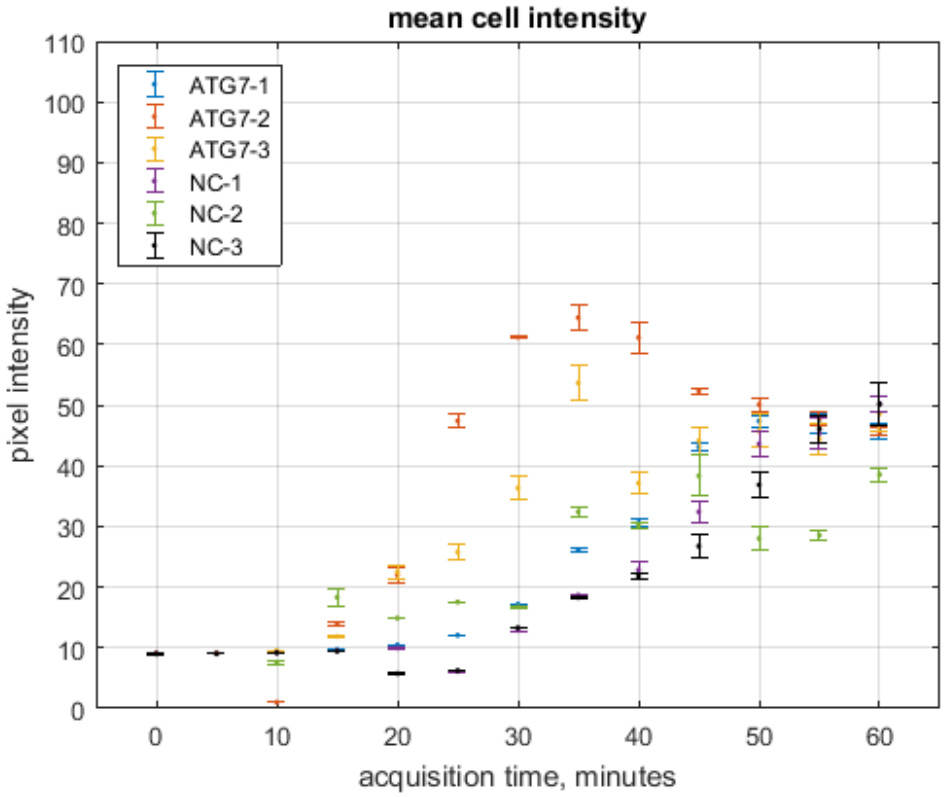

Figure 2. Mean pixel intensity per cell vs image acquisition time. Cells were incubated with 20µg/ml NBD-Cholesterol (Thermo Fisher, Waltham MA) for 60 minutes and imaged on a Nikon Ti-E confocal microscope, 20X water immersion objective. Before each image was taken, the z-axis was adjusted to re-focus on the cells, as live cells moved in and out of the focal plane. ATG7-1, ATG7-2, and ATG7-3 represent three biological replicate ATG7 siRNA transfections. NC-1, NC-2, and NC-3 represent three biological negative control siRNA transfections. Error bars represent ± SEM, n=3 cells minimum per replicate.

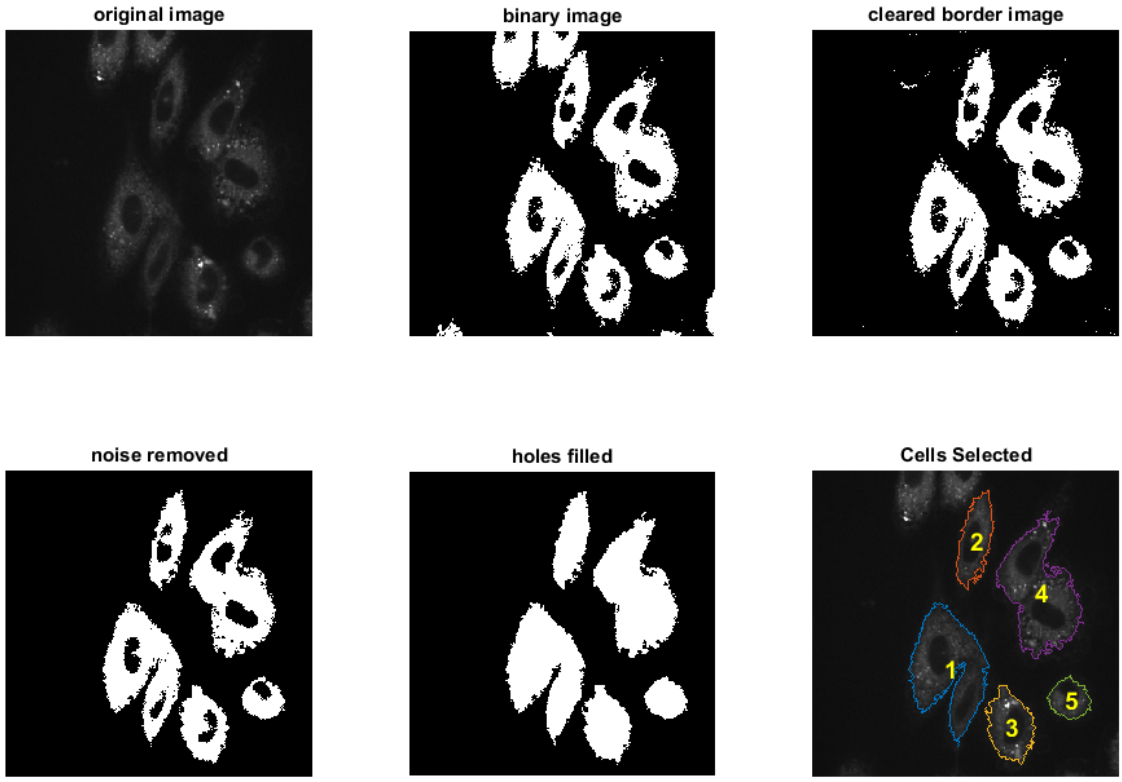

Figure 3. Computational Cell Segmentation Example. For analysis of fluorescence intensity per cell, an algorithm was written in MATLAB 2016b (Mathworks, Natick, MA). The original NBD channel image, top right corner, was thresholded to create the binary image. To select only intact cells, any objects that were 8-bit connected with the edge pixels were removed. Background noise was removed, and pixels that were not 8-bit connected to the edge pixels were filled in. The filled image was used to outline and index pixels corresponding to individual cells. The nuclei were segmented from the DAPI channel image using the same method. Pixels corresponding to nuclei in the NBD image were removed from each cell prior to mean intensity measurement.

The increased incorporation of the prenylation probe in ATG7 siRNA treated cells (Chapter 4, Figure 2) may be the result of decreased flux through the mevalonate pathway and an insufficient endogenous isoprenoid pool. As the prenylation assay only measures the probe incorporation due to prenylation activity, future work may be dedicated to a targeted metabolomics study quantifying the endogenous prenylation substrates farnesyl pyrophosphate and geranylgeranyl pyrophosphate[177].

To further elucidate the effect of ATG7 knockdown on autophagy, selective autophagy measurements are needed. The accumulation of mevalonate pathway proteins seen with autophagy inhibition may be the result of the autophagy machinery failing to break down ER resident cholesterol synthesis proteins. The CE-LIF method developed in Chapter 2 can be further adapted for selective monitoring of ER-phagy. As described above in Section 3, the CE-LIF instrument has the capability of detecting two different fluorophores. In addition to monitoring LC3-II positive autophagy organelles, ER could be monitored in a cell line expressing ER membrane protein p28[178] fused to a fluorescent protein. Dual labeled events will be representative of ER inside autophagy related organelles. In order to monitor ER-phagy flux, the number of dual labeled events can be monitored as a function of time following vinblastine treatment.

Bibliography

1. Sakuma, K., Aoi, W. & Yamaguchi, A. Current understanding of sarcopenia: possible candidates modulating muscle mass. *Pflugers Arch. Eur. J. Physiol.* **467,** 213–229 (2014).
2. Cree, M. G. *et al.* Intramuscular and liver triglycerides are increased in the elderly. *J. Clin. Endocrinol. Metab.* **89,** 3864–3871 (2004).
3. Nakagawa, Y. *et al.* Age-related changes in intramyocellular lipid in humans by in vivo H-MR spectroscopy. *Gerontology* **53,** 218–223 (2007).
4. Petersen, K. F. *et al.* Mitochondrial Dysfunction in the Elderly: Possible Role in Insulin Resistance. *Science (80).* **300,** 1140–1142 (2003).
5. Masiero, E. *et al.* Autophagy Is Required to Maintain Muscle Mass. *Cell Metab.* **10,** 507–515 (2009).
6. Schiaffino, S., Dyar, K. A., Ciciliot, S., Blaauw, B. & Sandri, M. Mechanisms regulating skeletal muscle growth and atrophy. *FEBS J.* **280,** 4294–4314 (2013).
7. Singh, R. *et al.* Autophagy regulates lipid metabolism. *Nature* **458,** 1131–1135 (2009).
8. Singh, R. & Cuervo, A. M. Lipophagy: connecting autophagy and lipid metabolism. *Int. J. Cell Biol.* **2012,** 282041 (2012).
9. Liu, K. & Czaja, M. J. Regulation of lipid stores and metabolism by lipophagy. *Cell Death Differ.* **20,** 3–11 (2013).
10. Lecker, S. H., Goldberg, A. L. & Mitch, W. E. Protein Degradation by the Ubiquitin-Proteasome Pathway in Normal and Disease States. *J. Am. Soc. Nephrol.* **17,** 1807–1819 (2006).
11. Lilienbaum, A. Relationship between the proteasomal system and autophagy. *Int. J. Biochem. Mol. …* **4,** 1–26 (2013).
12. Levine, B. & Kroemer, G. Autophagy in the pathogenesis of disease. *Cell* **132,** 27–42 (2008).
13. Cecconi, F. & Levine, B. The role of autophagy in mammalian development: cell makeover rather than cell death. *Dev. Cell* **15,** 344–357 (2008).
14. Mizushima, N. Autophagy: process and function. *Genes Dev* **21,** 2861–2873 (2007).
15. Boya, P., Reggiori, F. & Codogno, P. Emerging regulation and functions of autophagy. *Nat. Cell Biol.* **15,** 713–720 (2013).
16. Mizushima, N., Yoshimori, T. & Ohsumi, Y. The role of Atg proteins in autophagosome formation. *Annu. Rev. Cell Dev. Biol.* **27,** 107–32 (2011).
17. Ohsumi, Y. Molecular dissection of autophagy: two ubiquitin-like systems. *Nat. Rev. Mol. Cell Biol.* **2,** 211–6 (2001).
18. Tanida, I., Tanida-Miyake, E., Ueno, T. & Kominami, E. The human homolog of Saccharomyces cerevisiae Apg7p is a protein-activating enzyme for multiple substrates including human Apg12p, GATE-16, GABARAP, and MAP-LC3. *J. Biol. Chem.* **276,** 1701–1706 (2001).
19. Kabeya, Y. & Mizushima, N. LC3, a mammalian homologue of yeast

Apg8p, is localized in autophagosome membranes after processing. *EMBO …* **19,** 5720–5728 (2000).
20. Yang, Z. & Klionsky, D. J. Eaten alive: a history of macroautophagy. *Nat. Cell Biol.* **12,** 814–22 (2010).
21. Loos, B., Du Toit, A. & Hofmeyr, J. H. S. Defining and measuring autophagosome flux - Concept and reality. *Autophagy* **10,** 2087–2096 (2014).
22. Klionsky, D. J. *et al.* Guidelines for the use and interpretation of assays for monitoring autophagy (3rd edition). *Autophagy* **12,** 1–222 (2016).
23. Barth, S., Glick, D. & Macleod, K. F. Autophagy: Assays and artifacts. *J. Pathol.* **221,** 117–124 (2010).
24. Mizushima, N. & Yoshimori, T. How to Interpret LC3 Immunoblotting. *Autophagy* **3,** 542–545 (2007).
25. Klionsky, D. J. *et al.* Guidelines for the use and interpretation of assays for monitoring autophagy. *Autophagy* **8,** 445–544 (2012).
26. ASHFORD, T. P. & PORTER, K. R. Cytoplasmic components in hepatic cell lysosomes. *J. Cell Biol.* **12,** 198–202 (1962).
27. Deter, R. L. & De Duve, C. Influence of glucagon, an inducer of cellular autophagy, on some physical properties of rat liver lysosomes. *J. Cell Biol.* **33,** 437–449 (1967).
28. Eskelinen, E. L. Fine structure of the autophagosome. *Methods Mol. Biol.* **445,** 11–28 (2008).
29. Kadowaki, M. & Karim, M. R. Cytosolic LC3 Ratio as a Quantitative Index of Macroautophagy. *Methods Enzymol.* **451,** 199–213 (2009).
30. Kimura, S., Noda, T. & Yoshimori, T. Dissection of the autophagosome maturation process by a novel reporter protein, tandem fluorescent-tagged LC3. *Autophagy* **3,** 452–460 (2007).
31. Eskelinen, E. L. To be or not to be? Examples of incorrect identification of autophagic compartments in conventional transmission electron microscopy of mammalian cells. *Autophagy* **4,** 257–260 (2008).
32. Eng, K. E., Panas, M. D., Karlsson Hedestam, G. B. & McInerney, G. M. A novel quantitative flow cytometry-based assay for autophagy. *Autophagy* **6,** 634–641 (2010).
33. Shvets, E., Fass, E. & Elazar, Z. Utilizing flow cytometry to monitor autophagy in living mammalian cells. *Autophagy* **8627,** 621–628 (2008).
34. Hundeshagen, P., Hamacher-Brady, A., Eils, R. & Brady, N. R. Concurrent detection of autolysosome formation and lysosomal degradation by flow cytometry in a high-content screen for inducers of autophagy. *BMC Biol.* **9,** 38 (2011).
35. Degtyarev, M., Reichelt, M. & Lin, K. Novel quantitative autophagy analysis by organelle flow cytometry after cell sonication. *PLoS One* **9,** (2014).
36. Koga, H., Kaushik, S. & Cuervo, A. M. Altered lipid content inhibits autophagic vesicular fusion. *FASEB J.* **24,** 3052–3065 (2010).
37. Cuervo, A. M. *et al.* Autophagy and Aging: The Importance of Maintaining

'Clean' Cells. *Autophagy* **1,** 131–140 (2014).
38. Singh, R. *et al.* Autophagy regulates lipid metabolism. *Nature* **458,** 1131–5 (2009).
39. Zechner, R. & Madeo, F. Another way to get rid of fat. *Nature* **458,** 118–119 (2009).
40. Fujimoto, T. & Parton, R. G. Not Just Fat : The Structure and Function of the Lipid Droplet. 1–17 (2011).
41. Thiam, A. R., Farese, R. V & Walther, T. C. The biophysics and cell biology of lipid droplets. *Nat. Rev. Mol. Cell Biol.* **14,** 775–86 (2013).
42. Lass, A., Zimmermann, R., Oberer, M. & Zechner, R. Lipolysis - a highly regulated multi-enzyme complex mediates the catabolism of cellular fat stores. *Prog. Lipid Res.* **50,** 14–27 (2011).
43. Krahmer, N., Farese, R. V. & Walther, T. C. Balancing the fat: Lipid droplets and human disease. *EMBO Molecular Medicine* **5,** 905–915 (2013).
44. Ding, Y. *et al.* Isolating lipid droplets from multiple species. *Nat. Protoc.* **8,** 43–51 (2012).
45. Nishimoto, Y. *et al.* Cell death-inducing DNA fragmentation factor A-like effector A and fat-specific protein 27β coordinately control lipid droplet size in brown adipocytes. *J. Biol. Chem.* **292,** 10824–10834 (2017).
46. Shi, X. *et al.* Regulation of lipid droplet size and phospholipid composition by stearoyl-CoA desaturase. *J. Lipid Res.* **54,** 2504–2514 (2013).
47. Greenspan, P., Mayer, E. & Fowler, S. Nile red: a selective fluorescent stain for intracellular lipid droplets. *J. Cell Biol.* 965–973 (1985).
48. Yang, H. J., Hsu, C. L., Yang, J. Y. & Yang, W. Y. Monodansylpentane as a blue-fluorescent lipid-droplet marker for multi-color live-cell imaging. *PLoS One* **7,** (2012).
49. Mehlem, A., Hagberg, C. E., Muhl, L., Eriksson, U. & Falkevall, A. Imaging of neutral lipids by oil red O for analyzing the metabolic status in health and disease. *Nat. Protoc.* **8,** 1149–1155 (2013).
50. Klapper, M. *et al.* Fluorescence-based fixative and vital staining of lipid droplets in Caenorhabditis elegans reveal fat stores using microscopy and flow cytometry approaches. *J. Lipid Res.* **52,** 1281–1293 (2011).
51. Deutsch, M. J., Schriever, S. C., Roscher, A. A. & Ensenauer, R. Digital image analysis approach for lipid droplet size quantitation of Oil Red O-stained cultured cells. *Anal. Biochem.* **445,** 87–89 (2014).
52. McIntosh, A. L. *et al.* Direct interaction of Plin2 with lipids on the surface of lipid droplets: a live cell FRET analysis. *AJP Cell Physiol.* **303,** C728–C742 (2012).
53. Heintzmann, R. & Ficz, G. Breaking the resolution limit in light microscopy. *Briefings Funct. Genomics Proteomics* **5,** 289–301 (2006).
54. Smus, J. P. *et al.* Tracking adipogenic differentiation of skeletal stem cells by label-free chemically selective imaging. *Chem. Sci.* **6,** 7089–7096 (2015).

55. Cao, C., Zhou, D., Chen, T., Streets, A. M. & Huang, Y. Label-Free Digital Quantification of Lipid Droplets in Single Cells by Stimulated Raman Microscopy on a Microfluidic Platform. *Anal. Chem.* **88,** 4931–4939 (2016).
56. Ikonen, E. Cellular cholesterol trafficking and compartmentalization. *Nat. Rev. Mol. Cell Biol.* **9,** 125–38 (2008).
57. Ikonen, E. Mechanisms for Cellular Cholesterol Transport : Defects and Human Disease. *Physiol. Rev.* **86,** 1237–1261 (2006).
58. Maxfield, F. R. & Tabas, I. Role of cholesterol and lipid organization in disease. *Nature* **438,** 612–621 (2005).
59. Russell, D. Cholesterol biosynthesis and metabolism. *Cardiovasc. drugs Ther.* 103–110 (1992).
60. Goldstein, J. & Brown, M. Binding and Degradation of Low Density Lipoproteins by Cultured Human Fibroblasts. *J. Biol. Chem.* **249,** 5152–5162 (1974).
61. Brown, M. & Goldstein, J. The SREBP pathway: regulation of cholesterol metabolism by proteolysis of a membrane-bound transcription factor. *Cell* **89,** 331–340 (1997).
62. Horton, J., Goldstein, J. & Brown, M. SREBPs: activators of the complete program of cholesterol and fatty acid synthesis in the liver. *J. Clin. …* **109,** 1125–1131 (2002).
63. Chang, T. Y., Chang, C. C. Y. & Cheng, D. Acyl-coenzyme A:cholesterol acyltransferases. *Annu. Rev. Biochem* **66,** 613–634 (1997).
64. Buhman, K. F., Accad, M. & Farese, R. V. Mammalian acyl-CoA:cholesterol acyltransferases. *Biochim. Biophys. Acta - Mol. Cell Biol. Lipids* **1529,** 142–154 (2000).
65. Buhman, K. K. *et al.* Resistance to diet induced hypercholesterolemia and gallstone formation in ACAT2-deficient mice. *Nat. Med.* **6,** 1341–1347 (2000).
66. Phillips, M. C. Molecular mechanisms of cellular cholesterol efflux. *J. Biol. Chem.* **289,** 24020–24029 (2014).
67. Vedhachalam, C. *et al.* Mechanism of ATP-binding cassette transporter A1-mediated cellular lipid efflux to apolipoprotein A-I and formation of high density lipoprotein particles. *J. Biol. Chem.* **282,** 25123–25130 (2007).
68. Brunham, L. R. *et al.* Intestinal ABCA1 directly contributes to HDL biogenesis in vivo. *J. Clin. Invest.* **116,** 1052–1062 (2006).
69. Whiting, C. E. & Arriaga, E. a. CE-LIF analysis of mitochondria using uncoated and dynamically coated capillaries. *Electrophoresis* **27,** 4523–31 (2006).
70. Duffy, C. F., MacCraith, B., Diamond, D., O'Kennedy, R. & Arriaga, E. a. Fast electrophoretic analysis of individual mitochondria using microchip capillary electrophoresis with laser induced fluorescence detection. *Lab Chip* **6,** 1007–11 (2006).
71. Kostal, V. & Arriaga, E. Capillary electrophoretic analysis reveals subcellular binding between individual mitochondria and cytoskeleton.

Anal. Chem. **83,** 1822–1829 (2011).
72. Wolken, G. & Arriaga, E. Simultaneous Measurement of Individual Mitochondrial Membrane Potential and Electrophoretic Mobility by Capillary Electrophoresis. *Anal. Chem.* **86,** 4217–4226 (2014).
73. Duffy, C. F. *et al.* Determination of properties of individual liposomes by capillary electrophoresis with postcolumn laser-induced fluorescence detection. *Anal. Chem.* **73,** 1855–1861 (2001).
74. Gunasekera, N., Olson, K., Musier-Forsynth, K. & Arriaga, E. Capillary electrophoretic separation of nuclei released from single cells. *Anal. Chem.* **76,** 655–662 (2004).
75. Chen, Y., Walsh, R. J. & Arriaga, E. A. Selective determination of the doxorubicin content of individual acidic organelles in impure subcellular fractions. *Anal. Chem.* **77,** 2281–7 (2005).
76. Chen, Y., Xiong, G. & Arriaga, E. a. CE analysis of the acidic organelles of a single cell. *Electrophoresis* **28,** 2406–15 (2007).
77. Satori, C. P., Kostal, V. & Arriaga, E. A. Endocytic Organelles via Laser-Induced Fluorescence Detection. *Anal. Chem.* **83,** 7331–7339 (2011).
78. Satori, C. P. & Arriaga, E. A. Describing autophagy via analysis of individual organelles by capillary electrophoresis with laser induced fluorescence detection. *Anal. Chem.* **85,** 11391–400 (2013).
79. Taylor, T. H., Frost, N. W., Bowser, M. T. & Arriaga, E. A. Analysis of individual mitochondria via fluorescent immunolabeling with Anti-TOM22 antibodies. *Anal. Bioanal. Chem.* **406,** 1683–91 (2014).
80. Wolken, G. G., Kostal, V. & Arriaga, E. A. Capillary isoelectric focusing of individual mitochondria. *Anal. Chem.* **83,** 612–618 (2011).
81. Soo, C. Y. *et al.* Nanoparticle tracking analysis monitors microvesicle and exosome secretion from immune cells. *Immunology* **136,** 192–197 (2012).
82. Oosthuyzen, W. *et al.* Quantification of human urinary exosomes by nanoparticle tracking analysis. *J. Physiol.* **23,** 5833–5842 (2013).
83. Tatischeff, I., Larquet, E., Falcon-Perez, J. M., Turpin, P. Y. & Kruglik, S. G. Fast characterisation of cell-derived extracellular vesicles by nanoparticles tracking analysis, cryo-electron microscopy, and Raman tweezers microspectroscopy. *J. Extracell. Vesicles* **1,** (2012).
84. Gardiner, C., Ferreira, Y. J., Dragovic, R. A., Redman, C. W. G. & Sargent, I. L. Extracellular vesicle sizing and enumeration by nanoparticle tracking analysis. *J. Extracell. Vesicles* **2,** (2013).
85. Kramberger, P., Ciringer, M., Štrancar, A. & Peterka, M. Evaluation of nanoparticle tracking analysis for total virus particle determination. *Virol. J.* **9,** 265 (2012).
86. James, A. E. & Driskell, J. D. Monitoring gold nanoparticle conjugation and analysis of biomolecular binding with nanoparticle tracking analysis (NTA) and dynamic light scattering (DLS). *Analyst* **138,** 1212 (2013).
87. Ao, X., Zou, L. & Wu, Y. Regulation of autophagy by the Rab GTPase network. *Cell Death Differ.* **21,** 348–358 (2014).

88. Szatmári, Z. & Sass, M. The autophagic roles of Rab small GTPases and their upstream regulators: A review. *Autophagy* **10,** 1154–1166 (2014).
89. Miettinen, T. P. & Björklund, M. Mevalonate Pathway Regulates Cell Size Homeostasis and Proteostasis through Autophagy. *Cell Rep.* **13,** 2610–2620 (2015).
90. Wijdeven, R. H. *et al.* Cholesterol and ORP1L-mediated ER contact sites control autophagosome transport and fusion with the endocytic pathway. *Nat. Commun.* **7,** 11808 (2016).
91. Kaur, J. & Debnath, J. Autophagy at the crossroads of catabolism and anabolism. *Nat. Rev. Mol. Cell Biol.* **16,** 461–472 (2015).
92. He, C. & Klionsky, D. J. Regulation mechanisms and signaling pathways of autophagy. *Annu. Rev. Genet.* **43,** 67–93 (2009).
93. Rubinsztein, D. C., Mariño, G. & Kroemer, G. Autophagy and aging. *Cell* **146,** 682–95 (2011).
94. Cursio, R., Colosetti, P., Codogno, P., Cuervo, A. M. & Shen, H.-M. The Role of Autophagy in Liver Diseases: Mechanisms and Potential Therapeutic Targets. *Biomed Res. Int.* **2015,** 1–2 (2015).
95. Rautau, P.-E. *et al.* Autophagy in liver diseases. *J. Hepatol.* **53,** 1123–1134 (2010).
96. Kuma, A., Matsui, M. & Mizushima, N. LC3, an autophagosome marker, can be incorporated into protein aggregates independent of autophagy: Caution in the interpretation of LC3 localization. *Autophagy* **3,** 323–328 (2007).
97. Zhang, S. *et al.* High-Throughput Multiparameter Analysis of Individual Mitochondria. *Anal. Chem.* **84,** 6421–6428 (2012).
98. Jin, Y. *et al.* A CE-LIF method to monitor autophagy by directly detecting LC3 proteins in HeLa cells. *Analyst* **137,** 5571–5575 (2012).
99. Duffy, C., Fuller, K., Malvey, M., O'Kennedy, R. & Arriaga, E. Determination of electrophoretic mobility distributions through the analysis of individual mitochondrial events by capillary electrophoresis with laser-induced. *Anal. …* **74,** 171–176 (2002).
100. Chen, Y. & Arriaga, E. A. Individual acidic organelle pH measurements by capillary electrophoresis. *Anal. Chem.* **78,** 820–826 (2006).
101. Shimura, K. *et al.* Analysis of protein-protein interactions with a multi-capillary electrophoresis instrument. *Electrophoresis* **27,** 1886–1894 (2006).
102. Zhang, H. & Jin, W. Determination of different forms of human interferon-gamma in single natural killer cells by capillary electrophoresis with on-capillary immunoreaction and laser-induced fluorescence detection. *Electrophoresis* **25,** 1090–5 (2004).
103. Lacroix, M., Poinsot, V., Fournier, C. & Couderc, F. Laser-induced fluorescence detection schemes for the analysis of proteins and peptides using capillary electrophoresis. *Electrophoresis* **26,** 2608–2621 (2005).
104. Yang, W. C., Schmerr, M. J., Jackman, R., Bodemer, W. & Yeung, E. S.

Capillary electrophoresis-based noncompetitive immunoassay for the prion protein using fluorescein-labeled protein A as a fluorescent probe. *Anal. Chem.* **77,** 4489–4494 (2005).
105. Shintani, T. & Torimura, M. Optimization of a rapid and sensitive identi ¢ cation system for Salmonella enteritidis by capillary electrophoresis with. *FEMS Microbiol. Lett.* **210,** 245–249 (2002).
106. Frezza, C., Cipolat, S. & Scorrano, L. Organelle isolation: functional mitochondria from mouse liver, muscle and cultured fibroblasts. *Nat. Protoc.* **2,** 287–295 (2007).
107. Anderson, A. B., Xiong, G. & Arriaga, E. A. Doxorubicin accumulation in individually electrophoresed organelles. *J. Am. Chem. Soc.* **126,** 9168–9169 (2004).
108. Kostal, V., Fonslow, B. R., Arriaga, E. A. & Bowser, M. T. Fast determination of mitochondria electrophoretic mobility using micro free-flow electrophoresis. *Anal. Chem.* **81,** 9267–9273 (2009).
109. Davis, J. M. & Arriaga, E. A. Evaluation of peak overlap in migration-time distributions determined by organelle capillary electrophoresis: Type-II error analogy based on statistical-overlap theory. *J. Chromatogr. A* **1216,** 6335–6342 (2009).
110. Davis, J. M. & Arriaga, E. A. Estimation of migration-time and mobility distributions in organelle capillary electrophoresis with statistical-overlap theory. *Anal. Chem.* **82,** 307–315 (2010).
111. Baker, M. Blame it on the Antibodies. *Nature* **521,** 274–275 (2015).
112. Maecker, H. T. & Trotter, J. Flow Cytometry Controls, Instrument Setup, and the Determination of Positivity. *Cytom. Part A* **69A,** 1037–1042 (2006).
113. Mizushima, N., Ohsumi, Y. & Yoshimori, T. Autophagosome Formation in Mammalian Cells. *Cell Struct. Funct.* **27,** 421–429 (2002).
114. Mizushima, N. *et al.* Dissection of autophagosome formation using Apg5-deficient mouse embryonic stem cells. *J. Cell Biol.* **152,** 657–667 (2001).
115. Tanida, I., Ueno, T. & Kominami, E. LC3 conjugation system in mammalian autophagy. *Int. J. Biochem. Cell Biol.* **36,** 2503–2518 (2004).
116. Boswell, C. A. *et al.* Effects of charge on antibody tissue distribution and pharmacokinetics. *Bioconjug. Chem.* **21,** 2153–2163 (2010).
117. Dada, O. O. *et al.* Nine orders of magnitude dynamic range: Picomolar to millimolar concentration measurement in capillary electrophoresis with laser induced fluorescence detection employing cascaded avalanche photodiode photon counters. *Anal. Chem.* **83,** 2748–2753 (2011).
118. Murphy, D. J. The biogenesis and functions of lipid bodies in animals, plants and microorganisms. *Prog. Lipid Res.* **40,** 325–438 (2001).
119. Goldberg, A. A. *et al.* A novel function of lipid droplets in regulating longevity. *Biochem. Soc. Trans.* **37,** 1050–1055 (2009).
120. Mcintosh, A. L., Storey, S. M. & Atshaves, B. P. Intracellular Lipid Droplets Contain Dynamic Pools of Sphingomyelin: ADRP Binds Phospholipids with High Affinity. *Lipids* **45,** 465–477 (2010).

121. Londos, C., Brasaemle, D. L., Schultz, C. J., Segrest, J. P. & Kimmel, a R. Perilipins, ADRP, and other proteins that associate with intracellular neutral lipid droplets in animal cells. *Semin. Cell Dev. Biol.* **10,** 51–58 (1999).
122. Chanderbhan, R., Noland, B. J., Scallen, T. J. & Vahouny, G. V. Sterol carrier protein2. Delivery of cholesterol from adrenal lipid droplets to mitochondria for pregnanolone synthesis. *J. Biol. Chem.* **257,** 8928–8934 (1982).
123. Anstee, Q. M., Targher, G. & Day, C. P. Progression of NAFLD to diabetes mellitus, cardiovascular disease or cirrhosis. *Nat. Rev. Gastroenterol. Hepatol.* **10,** 330–344 (2013).
124. Day, C. P. & James, O. F. W. Steatohepatitis: A tale of two 'Hits'? *Gastroenterology* **114,** 842–845 (1998).
125. Daniele, J. R., Heydari, K., Arriaga, E. A. & Dillin, A. Identification and Characterization of Mitochondrial Subtypes in Caenorhabditis elegans via Analysis of Individual Mitochondria by Flow Cytometry. *Anal. Chem.* **88,** 6309–6316 (2016).
126. Malloy, A. & Carr, B. Nanoparticle tracking analysis - The Halo System. *Part. Syst. Charact.* **23,** 197–204 (2006).
127. Atshaves, B. P. *et al.* Sterol carrier protein-2 expression modulates protein and lipid composition of lipid droplets. *J. Biol. Chem.* **276,** 25324–35 (2001).
128. Storey, S. M., McIntosh, a. L., Senthivinayagam, S., Moon, K. C. & Atshaves, B. P. The phospholipid monolayer associated with perilipin-enriched lipid droplets is a highly organized rigid membrane structure. *AJP Endocrinol. Metab.* **301,** E991–E1003 (2011).
129. Chandrasekhar, S. Brownian Motion, Dynamical Friction and Stellar Dynamics. *Rev. Mod. Phys.* **21,** 383–388 (1949).
130. Einstein, A. On the Motion of Small Particles Suspended in a Stationary Liquid, as Required by the Molecular Kinetic Theory of Heat. *Ann. Phys.* **322,** 549–560 (1905).
131. Suzuki, M., Shinohara, Y., Ohsaki, Y. & Fujimoto, T. Lipid droplets: Size matters. *J. Electron Microsc. (Tokyo).* **60,** (2011).
132. Zhang, S. *et al.* Morphologically and Functionally Distinct Lipid Droplet Subpopulations. *Sci. Rep.* **6,** 29539 (2016).
133. Cohen, B.-C., Shamay, A. & Argov-Argaman, N. Regulation of lipid droplet size in mammary epithelial cells by remodeling of membrane lipid composition-a potential mechanism. *PLoS One* **10,** e0121645 (2015).
134. Slawik, M. & Vidal-Puig, A. J. Lipotoxicity, overnutrition and energy metabolism in aging. *Ageing Res. Rev.* **5,** 144–164 (2006).
135. Mizushima, N., Levine, B., Cuervo, A. M. & Klionsky, D. J. Autophagy fights disease through cellular self-digestion. *Nature* **451,** 1069–75 (2008).
136. Richler, C. & Yaffe, D. The in vitro cultivation and differentiation capacities of myogenic cell lines. *Dev. Biol.* **23,** 1–22 (1970).
137. McCoy, F. *et al.* Obatoclax induces Atg7-dependent autophagy

independent of beclin-1 and BAX/BAK. *Cell Death Dis.* **1,** 108 (2010).
138. Khan, M. J. *et al.* Inhibition of autophagy rescues palmitic acid-induced necroptosis of endothelial cells. *J. Biol. Chem.* **287,** 21110–21120 (2012).
139. Shimizu, S. *et al.* Inhibition of autophagy potentiates the antitumor effect of the multikinase inhibitor sorafenib in hepatocellular carcinoma. *Int. J. Cancer* **131,** 548–557 (2012).
140. Komatsu, M. *et al.* Impairment of starvation-induced and constitutive autophagy in Atg7-deficient mice. *J. Cell Biol.* **169,** 425–434 (2005).
141. DeGraw, A. J. *et al.* Evaluation of alkyne-modified isoprenoids as chemical reporters of protein prenylation. *Chem. Biol. Drug Des.* **76,** 460–71 (2010).
142. Palsuledesai, C. C. *et al.* Metabolic Labeling with an Alkyne-modified Isoprenoid Analog Facilitates Imaging and Quantification of the Prenylome in Cells. *ACS Chem. Biol.* **11,** 2820–2828 (2016).
143. Rio, D. C., Ares, M., Hannon, G. J. & Nilsen, T. W. Purification of RNA using TRIzol (TRI Reagent). *Cold Spring Harb. Protoc.* **5,** (2010).
144. Schmittgen, T. D. & Livak, K. J. Analyzing real-time PCR data by the comparative CT method. *Nat. Protoc.* **3,** 1101–1108 (2008).
145. Harsha, H. C., Molina, H. & Pandey, A. Quantitative proteomics using stable isotope labeling with amino acids in cell culture. *Nat. Protoc.* **3,** 505–16 (2008).
146. Mann, M. Functional and quantitative proteomics using SILAC. *Nat. Rev. Mol. Cell Biol.* **7,** 952–958 (2006).
147. Forner, F., Arriaga, E. A. & Mann, M. Mild protease treatment as a small-scale biochemical method for mitochondria purification and proteomic mapping of cytoplasm-exposed mitochondrial proteins. *J. Proteome Res.* **5,** 3277–3287 (2006).
148. Shevchenko, A., Tomas, H., Havli, J., Olsen, J. V & Mann, M. In-gel digestion for mass spectrometric characterization of proteins and proteomes. *Nat. Protoc.* **1,** 2856–2860 (2007).
149. Graumann, J. *et al.* Stable Isotope Labeling by Amino Acids in Cell Culture (SILAC) and Proteome Quantitation of Mouse Embryonic Stem Cells to a Depth of. *Proteins* **7,** 672–683 (2008).
150. Cox, J. & Mann, M. MaxQuant enables high peptide identification rates, individualized p.p.b.-range mass accuracies and proteome-wide protein quantification. *Nat. Biotechnol.* **26,** 1367–72 (2008).
151. Cox, J. & Neuhauser, N. Andromeda: a peptide search engine integrated into the MaxQuant environment. *J. proteome …* 1794–1805 (2011).
152. Käll, L., Storey, J. D., Maccoss, M. J. & Noble, W. S. Posterior Error Probabilities and False Discovery Rates: Two Sides of the Same Coin. *J. Proteome Res.* **7,** 40–44 (2007).
153. Navratil, M., Terman, A. & Arriaga, E. A. Giant mitochondria do not fuse and exchange their contents with normal mitochondria. *Exp. Cell Res.* **314,** 164–172 (2008).
154. de Pablo-Latorre, R. *et al.* Impaired parkin-mediated mitochondrial

targeting to autophagosomes differentially contributes to tissue pathology in lysosomal storage diseases. *Hum. Mol. Genet.* **21,** 1770–1781 (2012).
155. Brown, M. S., Dana, S. E. & Goldstein, J. L. Regulation of 3-hydroxy-3-methylglutaryl coenzyme A reductase activity in human fibroblasts by lipoproteins. *Proc. Natl. Acad. Sci. U. S. A.* **70,** 2162–6 (1973).
156. Towbin, H., Staehelint, T. & Gordon, J. Electrophoretic transfer of proteins from polyacrylamide gels to nitrocellulose sheets: Procedure and some applications (ribosomal proteins/radioimmunoassay/fluorescent antibody assay/peroxidase-conjugated antibody/autoradiography). **76,** 4350–4354 (1979).
157. Burnette, S. 'Western blotting': electrophoresis of protein from sodium dodecyl sulphate polyacrylamide gels to unmodified nitrocellulose and radiographic detection with antibody and radioiodinated protein A. *Anal. Biochem* **112,** 195–203 (1982).
158. Thissen, D., Steinberg, L. & Kuang, D. Quick and Easy Implementation of the Benjamini-Hochberg Procedure for Controlling the False Positive Rate in Multiple Comparisons. *J. Educ. Behav. Stat.* **27,** 77–83 (2002).
159. Jiang, Y. *et al.* Opposite roles of myocardin and atrogin-1 in L6 myoblast differentiation. *J. Cell. Physiol.* **228,** 1989–1995 (2013).
160. Lopez, V., Saraff, K. & Medh, J. D. Down-regulation of lipoprotein lipase increases glucose uptake in L6 muscle cells. *Biochem. Biophys. Res. Commun.* **389,** 34–39 (2009).
161. Millay, D. P. *et al.* Structure–function analysis of myomaker domains required for myoblast fusion. *Proc. Natl. Acad. Sci.* **113,** 2116–2121 (2016).
162. Sakai, J. *et al.* Sterol-regulated release of SREBP-2 from cell membranes requires two sequential cleavages, one within a transmembrane segment. *Cell* **85,** 1037–1046 (1996).
163. Sharpe, L. J. & Brown, A. J. Controlling cholesterol synthesis beyond 3-hydroxy-3-methylglutaryl-CoA reductase (HMGCR). *Journal of Biological Chemistry* **288,** 18707–18715 (2013).
164. Zerenturk, E. J., Sharpe, L. J. & Brown, A. J. Sterols regulate 3-hydroxysterol 24-reductase (DHCR24) via dual sterol regulatory elements: Cooperative induction of key enzymes in lipid synthesis by Sterol Regulatory Element Binding Proteins. *Biochim. Biophys. Acta - Mol. Cell Biol. Lipids* **1821,** 1350–1360 (2012).
165. Palsuledesai, C. C., Ochocki, J. D., Markowski, T. W. & Distefano, M. D. A combination of metabolic labeling and 2D-DIGE analysis in response to a farnesyltransferase inhibitor facilitates the discovery of new prenylated proteins. *Mol. Biosyst.* **10,** 1094–103 (2014).
166. Wang, H. J. *et al.* Chronic HMGCR/HMG-CoA reductase inhibitor treatment contributes to dysglycemia by upregulating hepatic gluconeogenesis through autophagy induction. *Autophagy* **11,** 2089–2101 (2015).
167. Peng, X. *et al.* Inhibition of Proliferation and Induction of Autophagy by Atorvastatin in PC3 Prostate Cancer Cells Correlate with Downregulation

of Bcl2 and Upregulation of miR-182 and p21. *PLoS One* **8,** (2013).
168. Dykstra, K. M., Allen, C., Born, E. J., Tong, H. & Holstein, S. A. Mechanisms for autophagy modulation by isoprenoid biosynthetic pathway inhibitors in multiple myeloma cells. *Oncotarget* **6,** 41535–41549 (2015).
169. Toepfer, N., Childress, C., Parikh, A., Rukstalis, D. & Yang, W. Atorvastatin induces autophagy in prostate cancer PC3 cells through activation of LC3 transcription. *Cancer Biol. Ther.* **12,** 691–699 (2011).
170. Reinhart, M. P., Billheimer, J. T., Faust, J. R. & Gaylor, J. L. Subcellular localization of the enzymes of cholesterol biosynthesis and metabolism in rat liver. *J. Biol. Chem.* **262,** 9649–9655 (1987).
171. Lipatova, Z., Shah, A. H., Kim, J. J., Mulholland, J. W. & Segev, N. Regulation of ER-phagy by a Ypt/Rab GTPase module. *Mol. Biol. Cell* **24,** 3133–3144 (2013).
172. Schuck, S., Gallagher, C. M. & Walter, P. ER-phagy mediates selective degradation of endoplasmic reticulum independently of the core autophagy machinery. *J. Cell Sci.* **127,** 4078–4088 (2014).
173. Bernales, S., McDonald, K. L. & Walter, P. Autophagy counterbalances endoplasmic reticulum expansion during the unfolded protein response. *PLoS Biol.* **4,** 2311–2324 (2006).
174. Khaminets, A. *et al.* Regulation of endoplasmic reticulum turnover by selective autophagy. *Nature* **522,** 354–358 (2015).
175. Xie, R., Nguyen, S., McKeehan, W. L. & Liu, L. Acetylated microtubules are required for fusion of autophagosomes with lysosomes. *BMC Cell Biol.* **11,** 89 (2010).
176. Muratore, K. A., Grundhofer, H. M. & Arriaga, E. A. Capillary Electrophoresis with Laser-Induced Fluorescent Detection of Immunolabeled Individual Autophagy Organelles Isolated from Liver Tissue.
177. Henneman, L. *et al.* Detection of nonsterol isoprenoids by HPLC-MS/MS. *Anal. Biochem.* **383,** 18–24 (2008).
178. Ng, F. W. H. *et al.* p28 Bap31, a Bcl-2/Bcl-X(L)- and procaspase-8-associated protein in the endoplasmic reticulum. *J. Cell Biol.* **139,** 327–338 (1997).
179. Atshaves, B. P. *et al.* Expression and intracellular processing of the 58 kDa sterol carrier protein-2/3-oxoacyl-CoA thiolase in transfected mouse L-cell fibroblasts. *J. Lipid Res.* **40,** 610–22 (1999).
180. Boulon, S. *et al.* Establishment of a Protein Frequency Library and Its Application in the Reliable Identification of Specific Protein Interaction Partners. *Mol. Cell. Proteomics* **9,** 861–879 (2010).
181. Daniele, J. R. *et al.* 'High-Throughput Characterization of Region-Specific Mitochondrial Function and Morphology'. *Sci. Rep.* **7,** 6749 (2017).

Appendix 1: Supplementary Information to Chapter 2

Supplementary Methods (Chapter 2)

Immunoblotting. Tris buffered saline, (TBS, 10 × concentration, 200nM Tris, 5M NaCl, pH 7.4), Tween-20, goat anti rabbit IgG: HRP, and 15% Tris-HCl Precast SDS-Page gels were obtained from Bio-Rad (Hercules, CA). Dylight488 conjugated rabbit anti-LC3 antibody, unconjugated rabbit anti-LC3 antibody, and rabbit anti-ATG5 antibody were obtained from Novus Biologicals (Littleton, CO). Skim milk powder was obtained from Wal-Mart (Bentonville, AR). Rabbit anti-GAPDH antibody was obtained from Rockland Immunochemical (Pottstown, PA). ATG5 (-/-) and (+/+) MEFS whole cell lysates were fractionated by 15% SDS-PAGE using a Criterion Cell apparatus (Bio-Rad). Gels were transferred to 0.45µm nitrocellulose membrane (Bio-Rad) using a Criterion Blotter apparatus (Bio-Rad). Membranes were blocked in 5% skim milk in TBS, 0.5% Tween-20. Membranes were probed overnight with 1:500 anti-ATG5, 1:5000 anti-GAPDH, and 1:1000 anti-LC3 primary antibody dilutions in 4% skim milk in TBS, 0.5% Tween-20. Secondary antibodies were goat anti rabbit IgG:HRP. All washes were with TBS, 0.5% Tween-20. The final washed blots were visualized on X-ray film using Pierce Super Signal West Femto substrate (Thermo Fisher Scientific). Films were digitized using a scanner and converted to 16-bit grayscale using ImageJ 1.51d (NIH, Bethesda, MD). Densitometry analysis was also performed in ImageJ.

Quantitative real-time PCR. Quantitative real-time PCR. The levels of ATG5 mRNA in ATG5 KO and WT MEFs were quantified using primers that amplify bases 242 to 341of ATG5 transcript variant 1 (NM.053069.6). RNA was isolated from ATG5 KO and WT MEFs using Trizol (Trizol Plus RNA Purification Kit, Thermo Fischer Scientific), followed by a DNAse treatment to rid samples of contaminating genomic DNA (RNAse-Free DNAse Set, RNeasy MinElute Kit, Qiagen). Single-strand cDNA was synthesized with oligo(dT) primers using AffinityScript Multiple Temperature Reverse Transcriptase (Agilent AffinityScript QPCR cDNA Synthesis Kit) and 5 ng of total RNA as template. Real-time analysis was performed using the Mx3000P QPCR System (Agilent) with the synthesized cDNA and Brilliant II SYBR Green PCR Master Mix (Agilent). Quantification of specific mRNA levels was calculated relative to the reference gene ACTB, using the comparative C_T method. A single dominant post-amplification product was confirmed via melting curves and agarose gel electrophoresis (single band corresponding to 100 or 188 bases for ATG5 or ACTB, respectively). Measured amplification efficiencies of both the ATG5 and ACTB amplicons were comparable, validating our use of the comparative C_T method. All reactions were run in triplicate and values are reported as mean ± SEM.

Supplementary Figure 1 (Chapter 2)

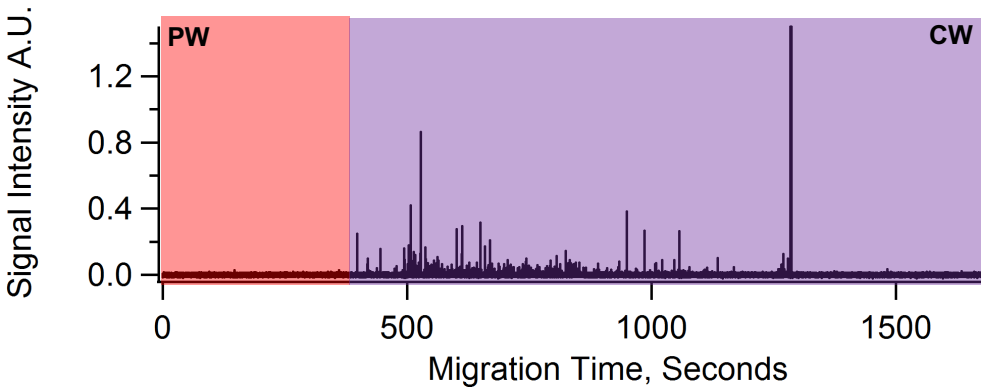

Supplementary Figure 1. False Positive Rate. The electropherogram (CE-LIF) or flowgram (capillary cytometry) are divided into "premigration" (PW) and "collection" (CW) windows. Equation 1 of the main text, uses the length of time it takes for the first organelle to reach the detector (P), the length of time where organelles are detected (W), the number of events (N) that occur during the PW, which are considered false positives, and the number of events (O_T) observed in the CW, which includes both false and true positives. Equation 1, assumes that the rate of false positives remains constant throughout the PW and CW. In the example electropherogram above, P = 418s, W = 1262s, N = 3 events, and O_T = 278 events. Equation 1 predicts that the number of true positives (O_C) is 269.

Supplementary Figure 2 (Chapter 2)

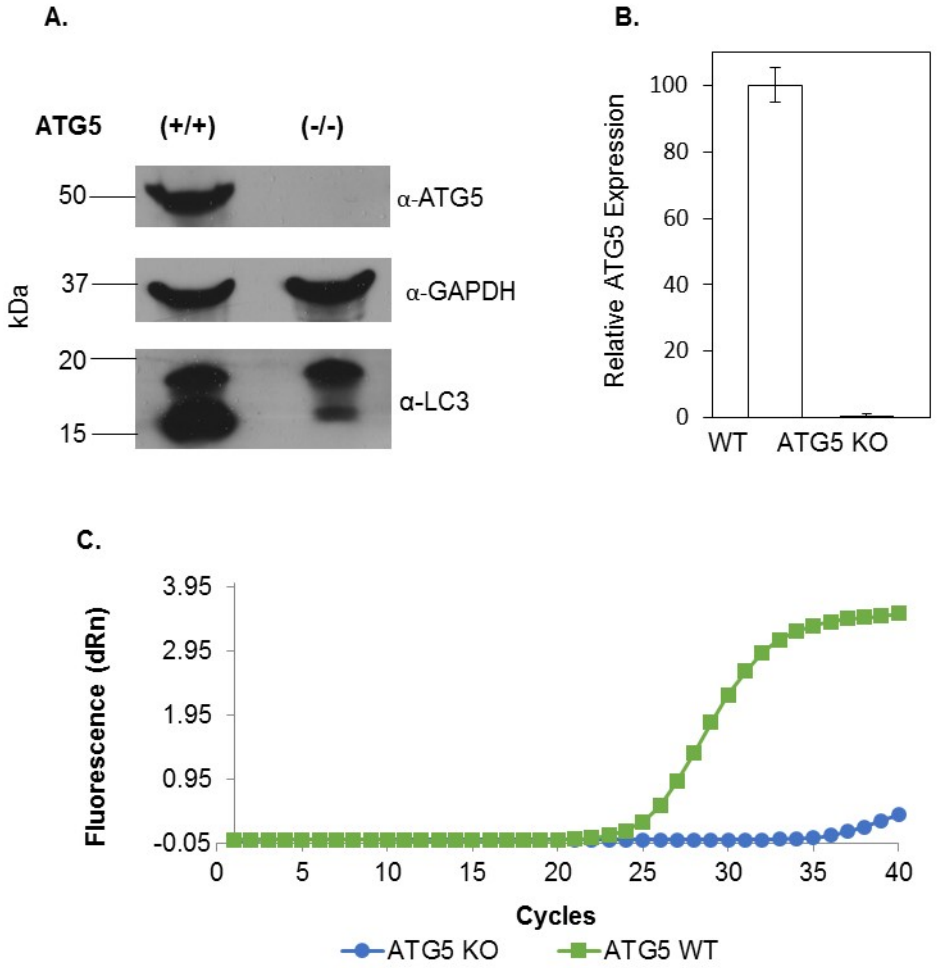

Supplementary Figure 2. Validation of wild type ATG5 (+/+) and knock-out ATG5 (-/-) MEFs. (A) Cell extracts were subject to separate blots probed independently with rabbit anti-ATG5, rabbit anti-GAPDH, or rabbit anti-LC3 antibodies. All lanes were loaded with 8µg protein. Positions of molecular mass markers are indicated on the left side. For ATG5 (+/+), S/N ~13,000; minimum amount of protein needed for detection ~ 15 fg. (B) ATG5 mRNA levels in the knock-out (ATG5 KO) and Wild type ATG5 (WT) MEFS were determined by qRT-PCR. Normalized data are means +/- SEM (n=3). The following primer sequences were used to assess ATG5 and ACTB mRNA levels: *ATG5* sense CTC GGT TTG GCT TTG GTT GA and antisense ACC ACA CAT CTC GAA GCA CA; *ACTB* sense AGG TGA CAG CAT TGC TTC TG and antisense GCT GCC TCA ACA CCT CAA C. (C) Representative amplification plot from qPCR reaction.

Supplementary Figure 3 (Chapter 2)

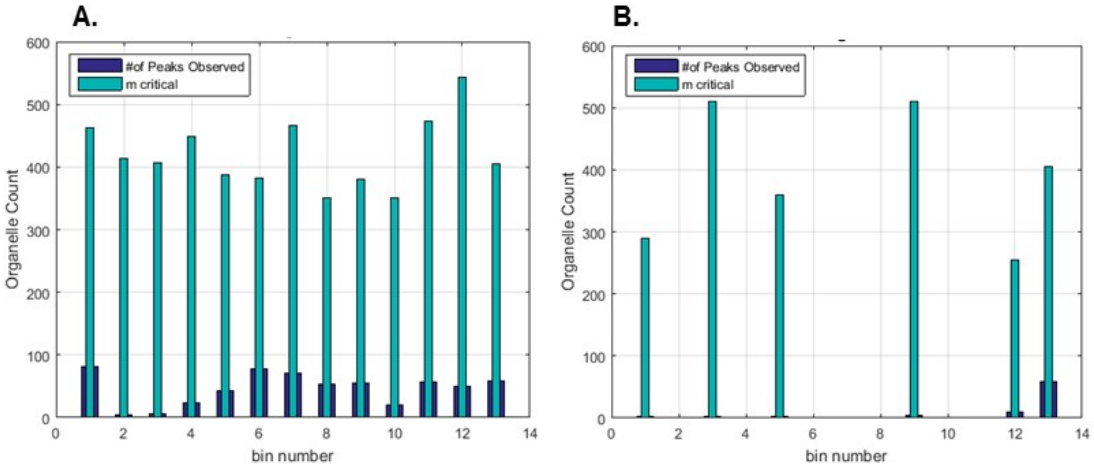

Supplementary Figure 3. **Statistical overlap theory of autophagy organelles from ATG5 (+/+) and *(-/-)* MEFS labeled with 300nM DyLight488-conjugated anti-LC3 antibody**. (A) Organelle counts for ATG5 (+/+). (B) Organelle counts for ATG5 (-/-) data. CE-LIF data was partitioned into bins of a consistent length, and the threshold saturation value was estimated based on the bin length in seconds, average peak width, and number of bins. The threshold saturation value is represented as m critical in the bar graph. For more information see Figure 2 in the main manuscript.

Supplementary Figure 4 (Chapter 2)

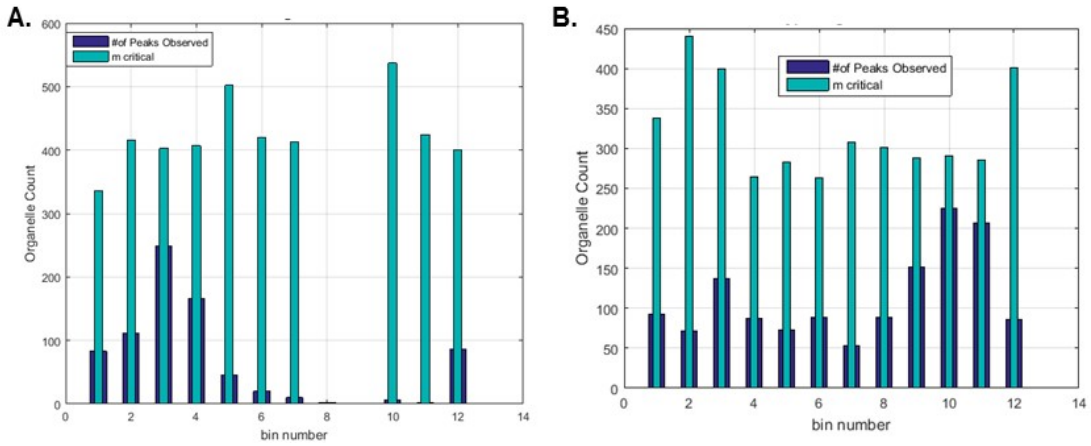

Supplementary Figure 4. **Statistical overlap theory of autophagy organelles from murine liver tissue labeled with 300nM DyLight488-conjugated anti-LC3 antibody and Dylight488-conjugated Isotype control.** (A) Organelle counts for labeling with DyLight488-conjugated anti-LC3 antibody. (B) Organelle counts for labeling with DyLight488-conjugated isotype control. Other conditions were as described in Figure S2. For more information see Figure 3 in the main manuscript.

Supplementary Figure 5 (Chapter 2)

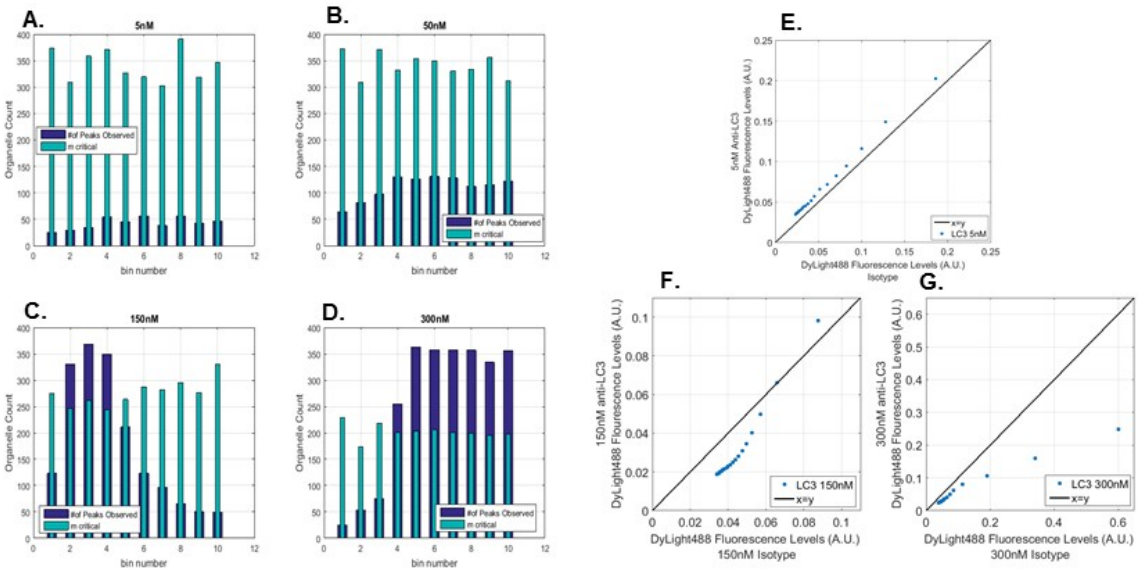

Supplementary Figure 5. Statistical overlap theory and QQ plot analysis of autophagy organelles from murine liver tissue labeled with 5-300nM DyLight488-conjugated anti-LC3 antibody. (A-D) Statistical overlap theory of autophagy organelles from murine liver tissue labeled with (A) 5nM, (B) 50nM, (C) 150nM, or (D) 300nM DyLight488 anti-LC3. Other conditions were as described in Figure S2. There were severe SOT violations when using 150 nM (C) and 300 nM (D) antibody concentrations. Elimination of compromised bins results in 59% and 94% reduction, respectively, in the number of organelles that are representative of individual events. (E-G) QQ plots to compare intensity distributions from anti-LC3 antibody and isotype control. The intensity percentiles from 5nM (E), 150nM (F), and 300nM (G) anti-LC3 labeled sample (y-axis) are plotted against the intensity percentiles from the isotype labeled sample (x axis). Data from 150 nM and 300 nM exclude data with SOT violations represented in (C) and (D), respectively. For more information see Figure 4 in the main manuscript.

Supplementary Figure 6 (Chapter 2)

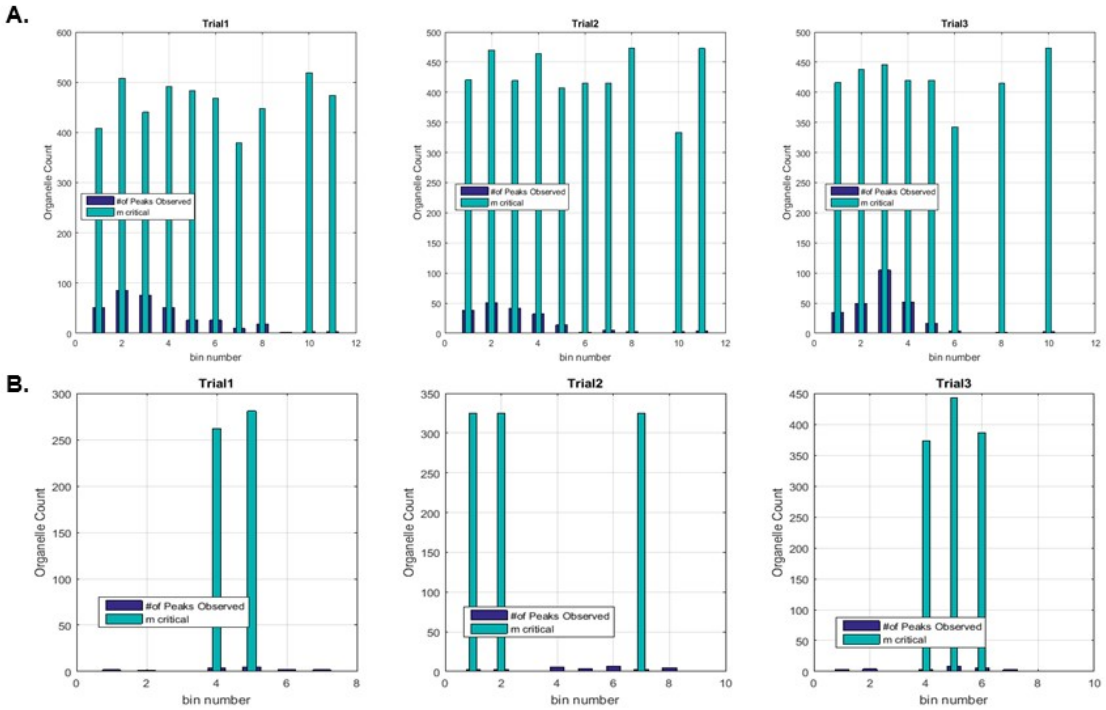

Supplementary Figure 6. **Statistical overlap theory of autophagy organelles from murine liver tissue labeled with 50nM DyLight 488-conjugated anti-LC3 antibody or 50nM DyLight 488-conjugated isotype control.** (A) Organelle counts for DyLight 488-conjugated anti-LC3 antibody. (B) Organelle counts for DyLight 488-conjugated isotype control. Other conditions were as described in Figure S2. Data correspond to Figure 5 of the main manuscript.

Supplementary Figure 7 (Chapter 2)

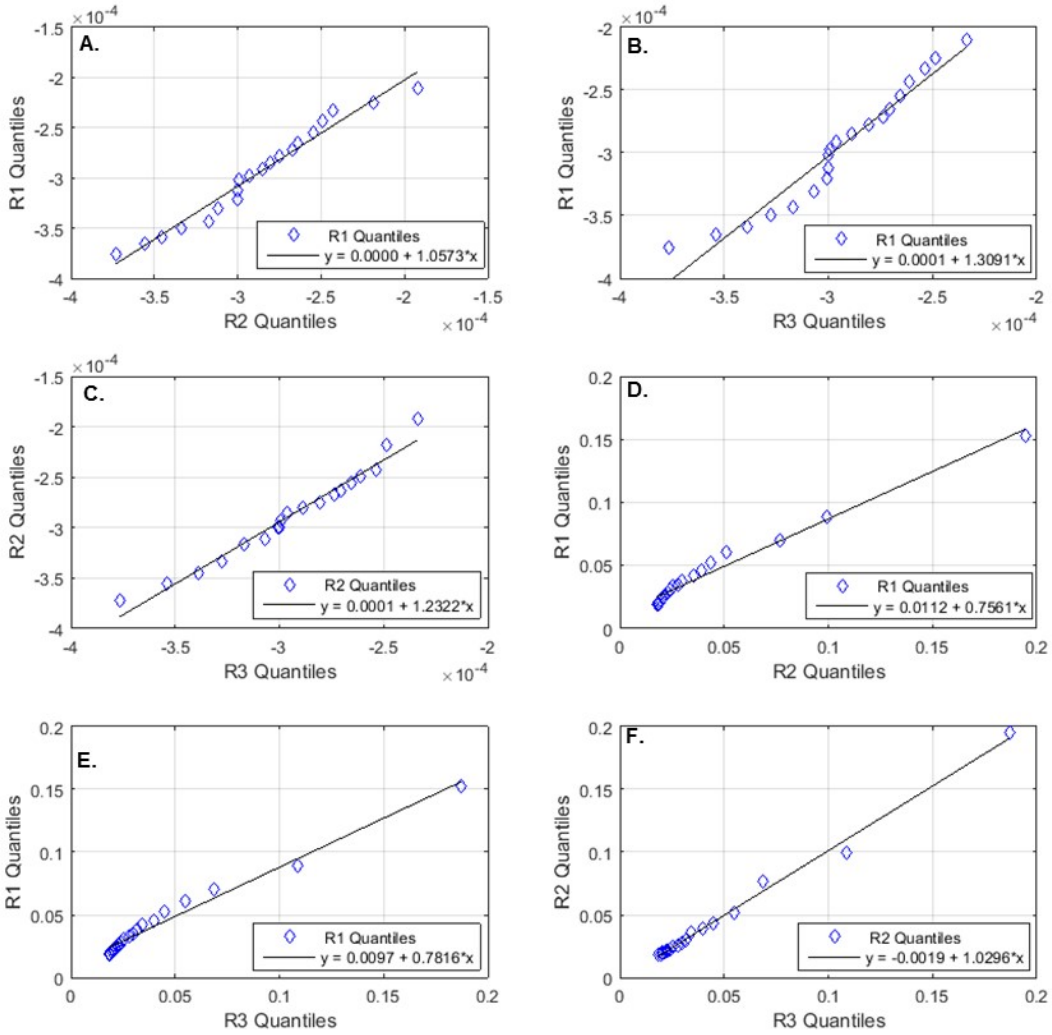

Supplementary Figure 7. Linear regression analysis of QQ data of murine liver autophagy organelles labeled with 50nM DyLight488-conjugated anti-LC3 antibody. (A-C). Linear regressions between quantiles of electrophoretic mobility distributions of pairs of replicates. From (A) to (C), the 95% confidence intervals for the slope of each comparison were [1.0 1.2], [1.2 1.5], [1.1 1.2], respectively; the slopes were not statistically different (p=0.05). (D-F). Linear regressions between quantiles of intensity distributions of pairs of replicates. From (D) to (F), the 95% confidence intervals for the slope of each comparison were [0.7, 0.8], [0.7 0.8], and [1.0, 1.1], respectively; the slopes were statistically different (p=0.05). Replicate 1 (R1), Replicate 2 (R2), Replicate 3 (R3) are described in Figure 5 of the main manuscript. Data acquired using conditions described in Figure 1 of the main manuscript.

Appendix 2: Supplementary Information to Chapter 3

Supplementary Data Analysis (Chapter 3)

For particle size standards measured by NTA, we report the following % error and correction factors, as defined in the main text:

Size Standard	Nominal Size, nm	Size by TEM, nm	Size by NTA, nm	*e*	*c*
3030A	31	25	38	0.52	0.48
3K-100	102	102	108	0.05	0.95
3K-200	203	203	203	0	1

To determine the correction factor at additional particle sizes in this study, we performed linear interpolation in MATLAB 2016b between the correction factors of the standards. The correction factor for sizes <25 nm was assumed to be 0.48 and the correction for sizes >203nm was assumed to be 1.

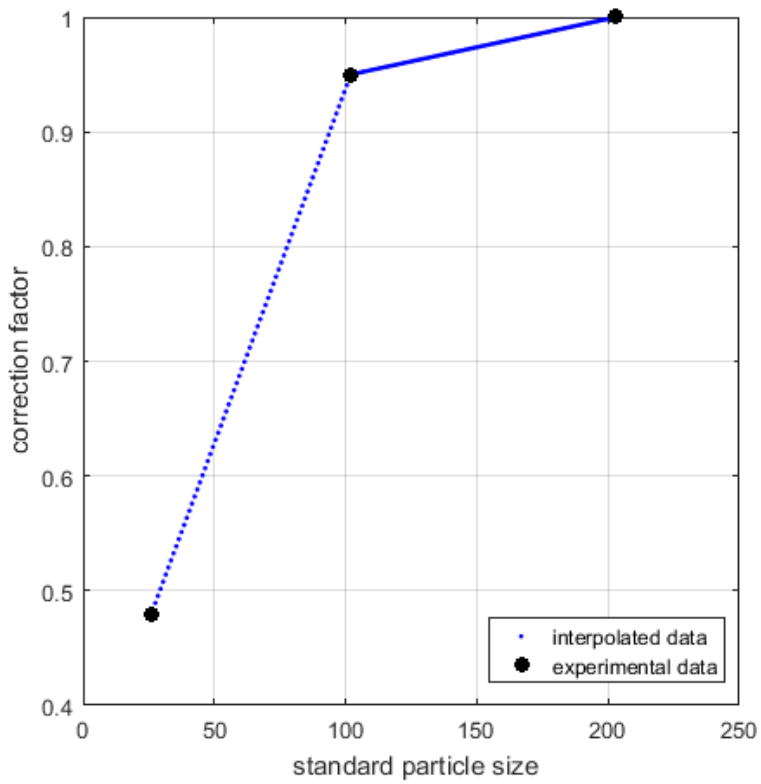

Supplementary Tables (Chapter 3)

1A. ANOVA Table

Sources of Variation	*SS*	*df*	*MS*	*F*	*P*
Between Groups	9345	3	3115	65.58	P<0.0001
Within Groups	760	16	47.5		
Total	10110	19			

1B. Tukey's Multiple Comparison Test	**Mean Diff.**	**q**	**P value**	**95% CI of diff**
Day 0 vs Day 1	3	0.9733	P > 0.05	-9.471 to 15.47
Day 0 vs Day 2	-10	3.244	P > 0.05	-22.47 to 2.471
Day 0 vs Day 7	-51	16.55	P < 0.001	-63.47 to -38.53
Day 1 vs Day 2	-13	4.218	P < 0.05	-25.47 to -0.5294
Day 1 vs Day 7	-54	17.52	P < 0.001	-66.47 to -41.53
Day 2 vs Day 7	-41	13.3	P < 0.001	-53.47 to -28.53

Supplementary Table 1. ANOVA and post-hoc Tukey analysis of mean LD size. Rows highlighted in yellow indicate statistical significance.

2A. ANOVA TABLE

Sources of Variation	*SS*	*df*	*MS*	*F*	*P*
Between Groups	2.678	3	0.8928	13.68	0.0001
Within Groups	1.044	16	0.06525		
Total	3.722	19			

2B. Tukey's Multiple Comparison Test

	Mean Diff.	**q**	**P value**	**95% CI of diff**
Day 0 vs Day 1	0.02	0.1751	P > 0.05	-0.4422 to 0.4822
Day 0 vs Day 2	0.75	6.565	P < 0.01	0.2878 to 1.212
Day 0 vs Day 7	-0.22	1.926	P > 0.05	-0.6822 to 0.2422
Day 1 vs Day 2	0.73	6.39	P < 0.01	0.2678 to 1.192
Day 1 vs Day 7	-0.24	2.101	P > 0.05	-0.7022 to 0.2222
Day 2 vs Day 7	-0.97	8.491	P < 0.001	-1.432 to -0.5078

Supplementary Table 2. ANOVA and post-hoc Tukey analysis of mean LD concentration. Rows highlighted in yellow indicate statistical significance.

Supplementary Figure 1 (Chapter 3)

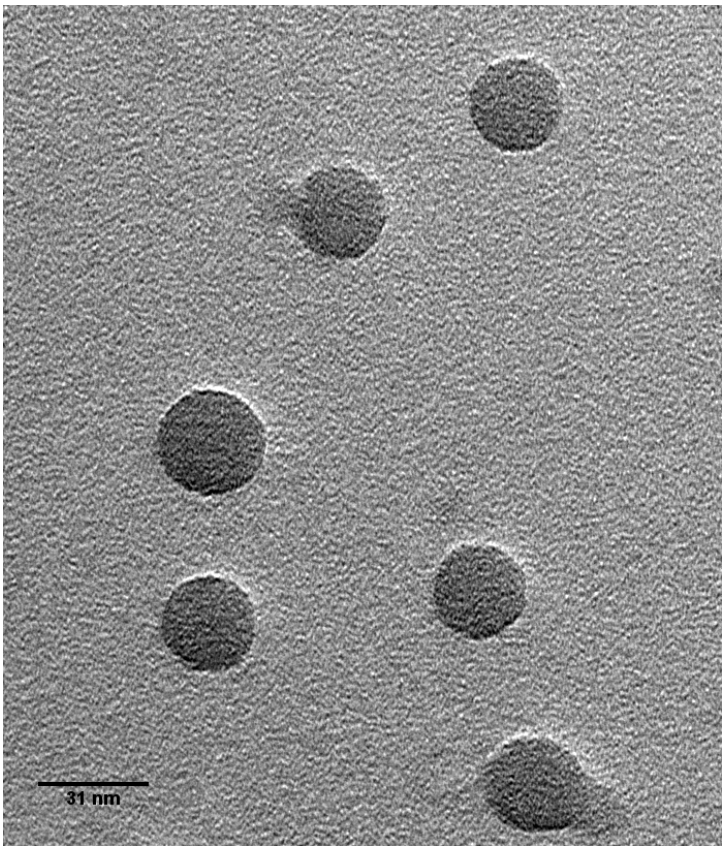

Supplementary Figure 1. TEM of 31nm Polystyrene Latex Nanospheres. 2µl nanosphere suspension was pipetted onto a copper grid and allowed to air dry. The nanospheres were imaged on a Tecnai T12 transmission electron microscope (FEI, Hillsboro, Oregon). The nanosphere size was determined from the resulting images using ImageJ (NIH, Bethesda, Maryland). The mean particle size was 25nm ± 5nm (± SEM), n=60 nanospheres. The above image is representative of several images used to measure 60 nanospheres total. *Data collected by Nick Livezey.*

Supplementary Figure 2 (Chapter 3)

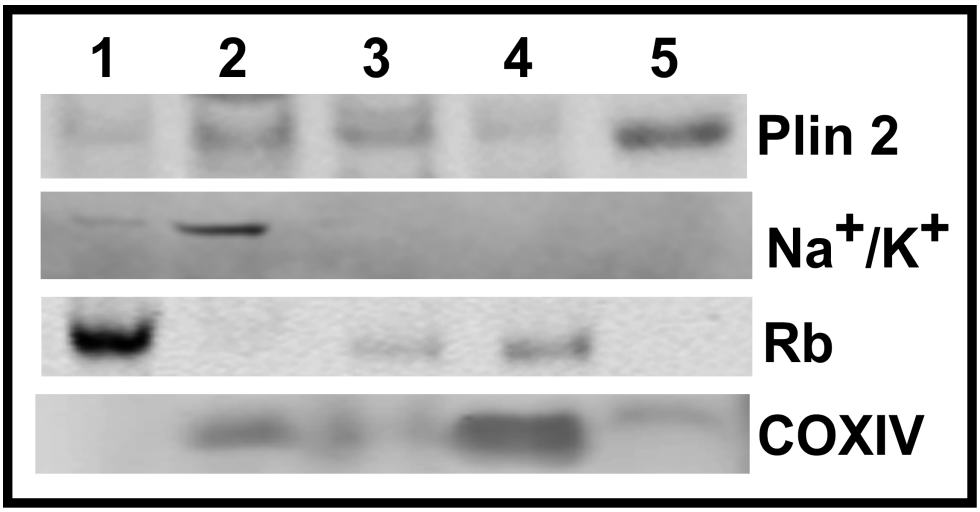

Supplementary Figure 2. Isolation of lipid droplets from mouse liver. Representative Western blots of cellular fractions isolated from wild type mouse liver: lane 1, nucleus; lane 2, plasma membrane; lane 3, cytosol; lane 4, mitochondria; and lane 5, lipid droplets. Liver homogenates (10-20 µg protein) were separated on 10% tricine gels using a Mini-Protean II cell (Bio-Rad lab, Hercules, CA) system at constant amperage (40 mA per gel) for about 2 hrs. Proteins were then transferred onto PVDF membranes at constant voltage (90 V) for 2 hrs. Blots were stained with Ponceau S to confirm uniform protein loading before blocking in 5% BSA in TBST (10 mM Tris-HCl, pH 8, 100mM NaCl, 0.05% Tween-20) for 1 hour. Rabbit polycolonal antibodies against Na+/K+ channel (plasma membrane marker), Rb (nuclear marker), and COXIV (mitochondrion marker) were obtained from Cell Signaling Technology (Danvers, MA) and used at 1:1000 dilution in 5% BSA/TBST. Rabbit polyclonal antibody against Plin2 (lipid droplet marker) was prepared in house as previously described[52,179] and used at 1:1000 dilution in 5% BSA/TBST. Blots were incubated with primary antibodies overnight and were developed with IRDye 800CW anti-mouse (LI-COR) or IRDye 680RD anti-rabbit (LI-COR) secondary antibodies. To visualize the bands of interest, blots were scanned using the LI-COR Odyssey imaging system (Lincoln, NE). *Data collected by Charlie Najt.*

Supplementary Figure 3 (Chapter 3)

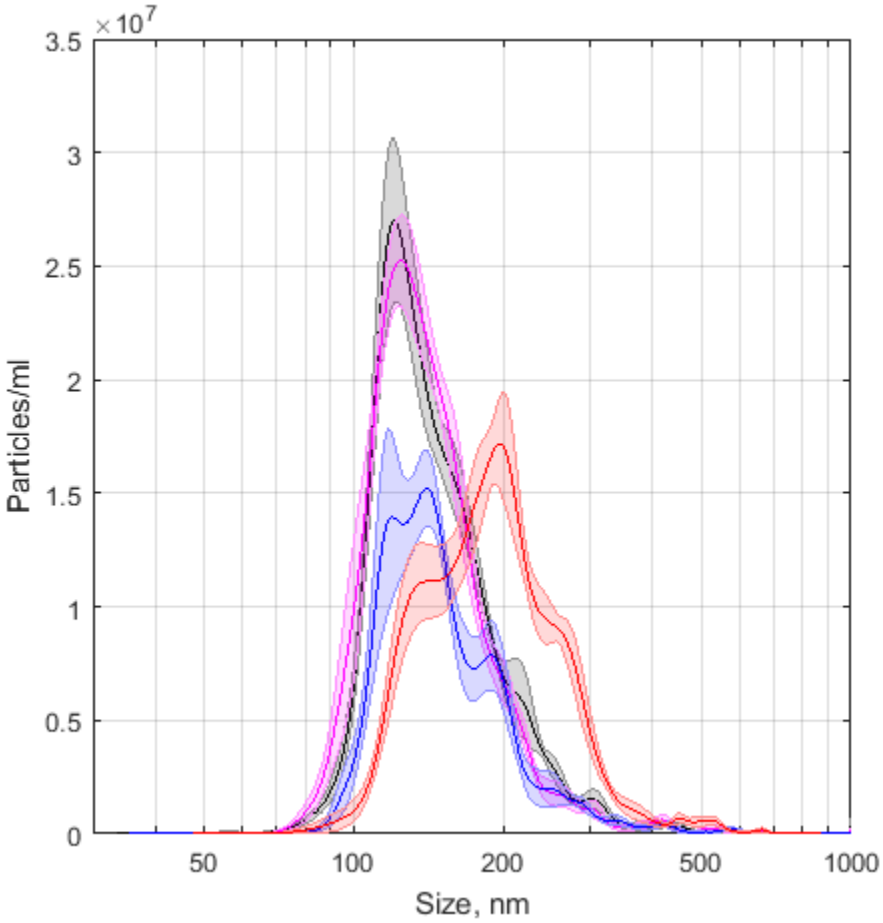

Supplementary Figure 3. Histograms for stability study. Day 0 is black, Day 1 is magenta, Day 2 is blue, and Day 7 is red, respectively. Shaded area represents +/- SEM, n=5 technical replicates.

Supplementary Figure 4 (Chapter 3)

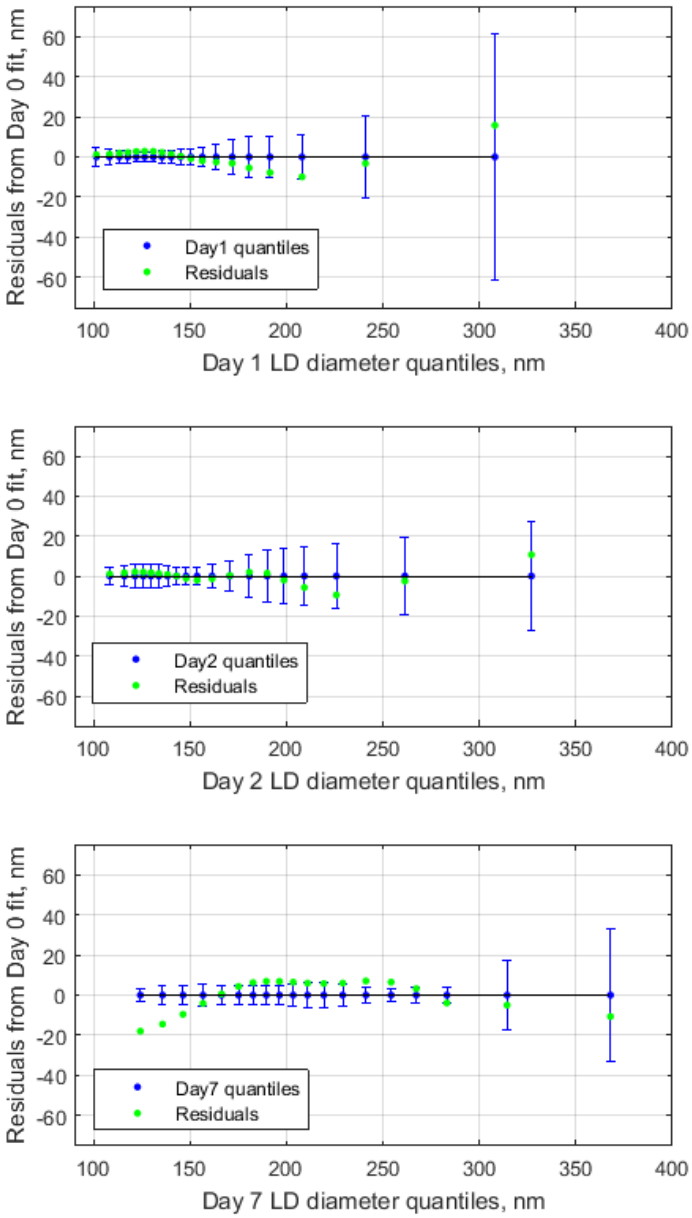

Supplementary Figure 4. Stability Study Residuals Analysis. The residuals are graphically represented on top of the quantiles from each data set +/- SEM, n=5 technical replicates. If a majority of residuals fall within the error bars, the linear fit predicted by the Day 0 distribution is a suitable model. When the residuals for the Day 1 vs Day 0 and Day 2 vs Day 0 are graphed, they are within the range of SEM for each day, respectively. When the residuals are graphed for Day 7 vs Day 0, the majority of the residuals fall outside the SEM. This strengthens the evidence for a statistically significant difference in distribution shape between Day 0 and Day 7, and suggests that the linear regression model based on Day 0 is not sufficient to predict the distribution shape on Day 7. Is also important to note that as quantiles, the data points are not independent. Thus, the residuals do not follow a random pattern in any of the plots.

Supplementary Figure 5 (Chapter 3)

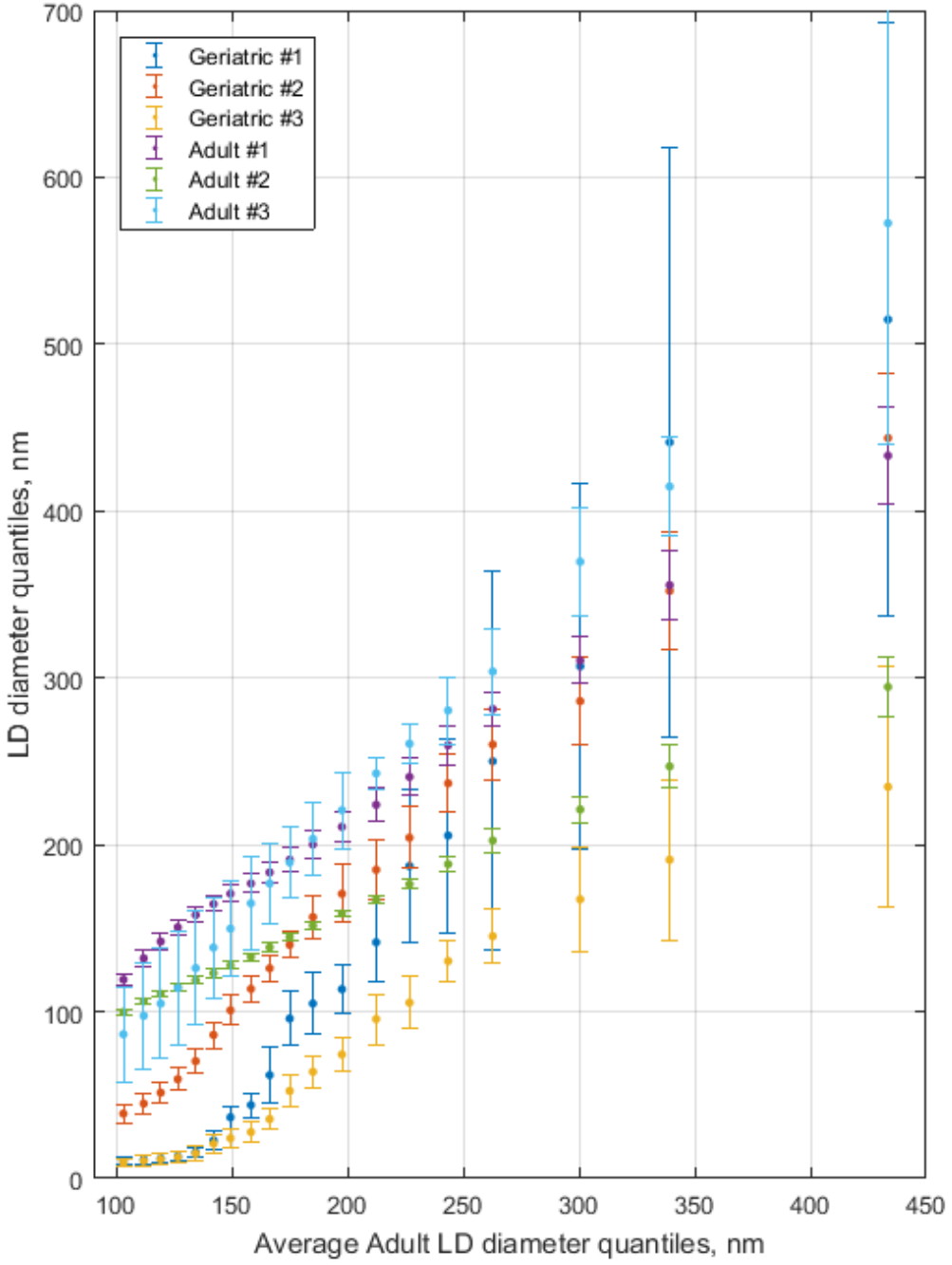

Supplementary Figure 5. QQ plot of Individual Mice. Lipid droplets were isolated from n=3 livers from geriatric mice and n=3 livers from adult mice prior to NTA. LD diameter (nm) size distribution from individual geriatric mice and individual adult mice (y axis) ± SEM, n=5 technical replicates vs average adult (x-axis) ± SEM, n=3 biological replicates. Markers represent the average 5^{th}-95^{th} percentiles.

Supplementary Figure 6 (Chapter 3)

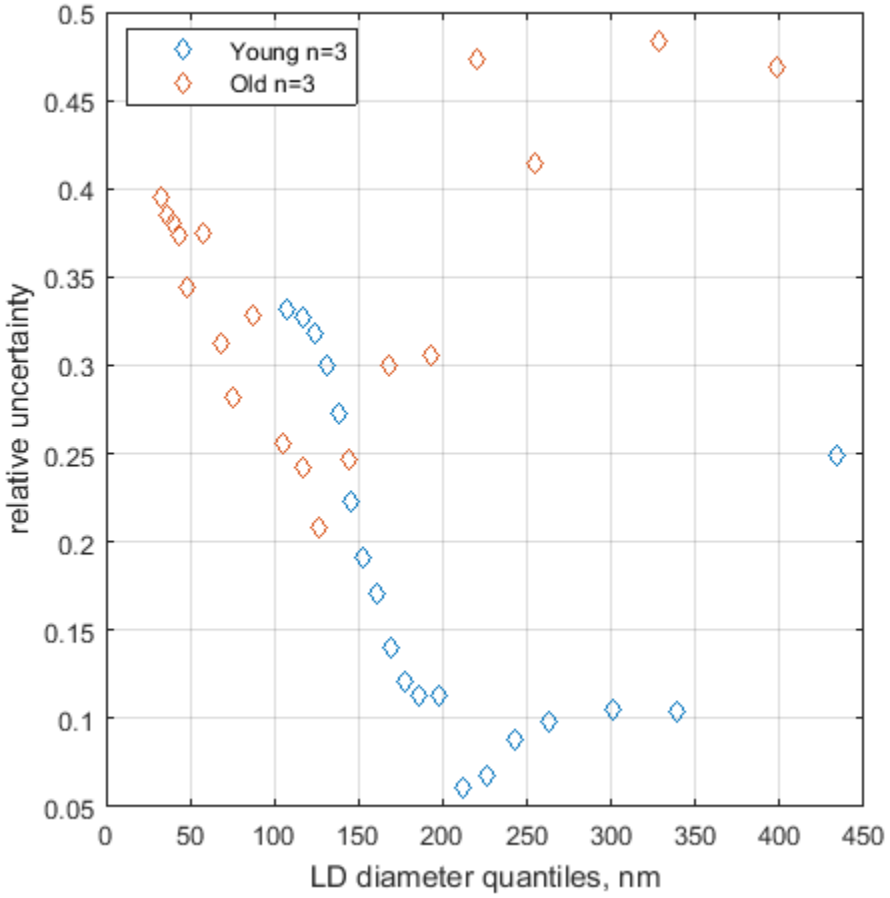

Supplementary Figure 6. Scatter plot of relative uncertainty. Percentile relative uncertainty (y-axis) vs 5^{th}-95^{th} percentiles (x-axis) of young and old, respectively.

Appendix 3: Supplementary Information to Chapter 4

Supplementary Methods (Chapter 4)

siRNA transfection. Apg71_predicted-RSS319788 (#10620319 & #10620318, Invitrogen, Carlsbad, CA) StealthTM RNAi (Primer 1: UUA UUC UGC AGA AUG GAU GAC CAG G; Primer 2: CCU GGU CAU CCA UUC UGC AGA AUA A) or a scrambled siRNA control (StealthTM RNAi Negative Control, Medium GC Duplex, #45-2001, Invitrogen, Carlsbad, CA) was dissolved in Opti-MEM serum-free media. The Atg7 or negative control siRNA were delivered into the L6 cell cultures via Lipofectamine 2000 (#11668-019, Thermo Fisher, Waltham, MA). The final concentration of Atg7 siRNA in culture was 66nM. The cells were incubated with the transfection reagents for 4 hours before replacing the media with fresh SILAC DMEM. The cells were then cultured for an additional 48 hours before harvest for MS analysis.

Table 1: Primer Sequences

TARGET	SEQUENCE
HMGCR-F	CGG GTC CTT GCA GAT GGG AT
HMGCR-R	CGT GCA AAT CTG CTC GTG CT
FDPS-F	CCA GGA ACT GGT GGA ACC AA
FDPS-R	GAA GAA AGC CTG GAG CAG TTC
FDFT-F	GGG ACA TAC GTC ATG CGG TG
FDFT-R	TTT CGC AGC AGT GGG ATC TT
ATG7-F	CAG TCG GTG TGT AGC ATC CC
ATG7-R	AAA CTG CCG CTC CAT CTG TG
RPL32-F	AAA CTG GCG GAA ACC CAG AG
RPL32-R	GCA GCA CTT CCA GCT CCT TG

Supplementary Figure 1 (Chapter 4)

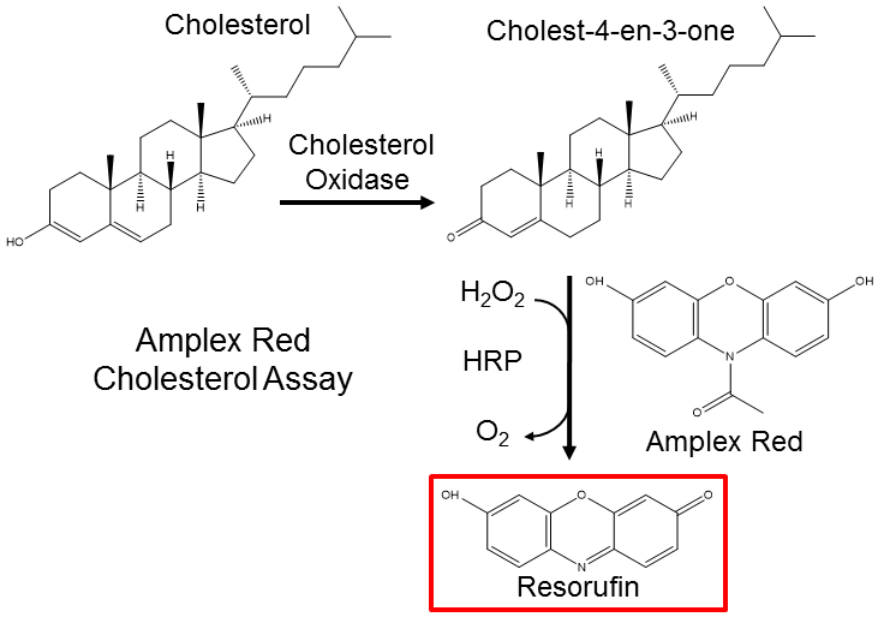

Figure 1. Amplex Red Cholesterol Assay. Free cholesterol reacts with cholesterol oxidase to form hydrogen peroxide and cholest-4-en-3-one. In the presence of horseradish peroxidase (HRP), hydrogen peroxide reacts with Amplex Red to form fluorescent resorufin in a 1:1 stochiometric ratio, enabling the measurement of free cholesterol.

Supplementary Figure 2 (Chapter 4)

A.

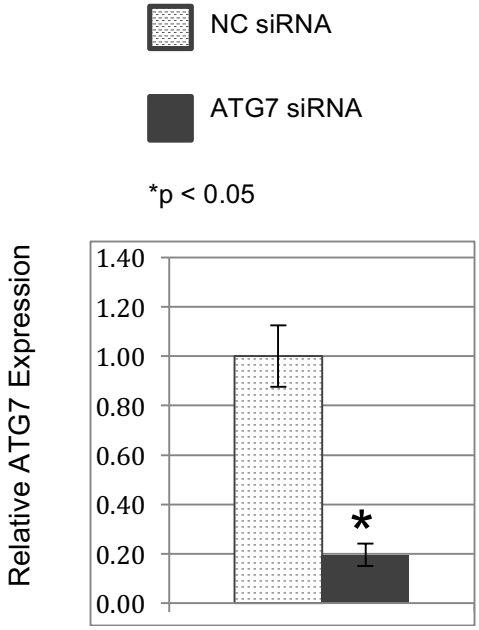

B.

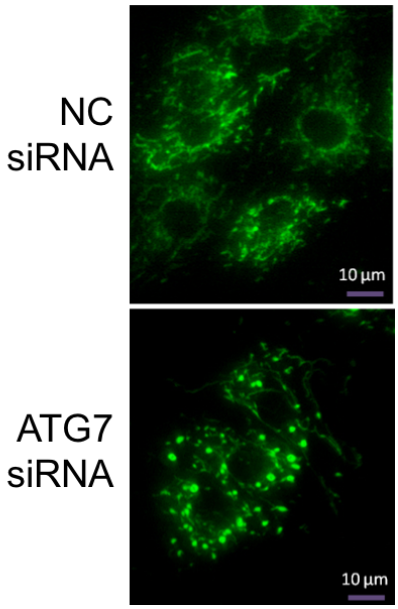

C.

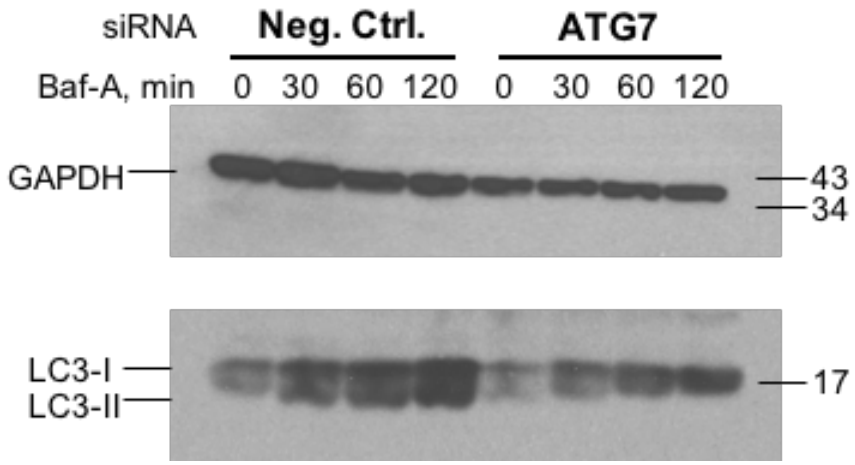

Supplementary Figure 2. A. qPCR of ATG7 gene in ATG7 siRNA treated cells and negative control treated cells. Cells treated with ATG7 siRNA had a 5.0 fold decrease in ATG7 mRNA compared to negative control siRNA treated cells, p=0.003. Error bars represent (+/-) SEM**. B. Visualization of giant mitochondria in ATG7 siRNA and negative control siRNA treated L6 myoblasts.** Mitochondria are labeled with Mitotracker Green (Thermo Fisher Scientific, Waltham, MA). *Data collected by Vrata Kostal.* **C. LC3 I and II abundance in ATG7 siRNA and negative control treated cells, (+/-) 100nM balfilomycin A.** BafA treatment time is indicated above each lane of the blot. Treatment with bafilomycin A resulted in an accumulation of LC3-II in negative control siRNA treated cells only.

Supplementary Figure 3 (Chapter 4)

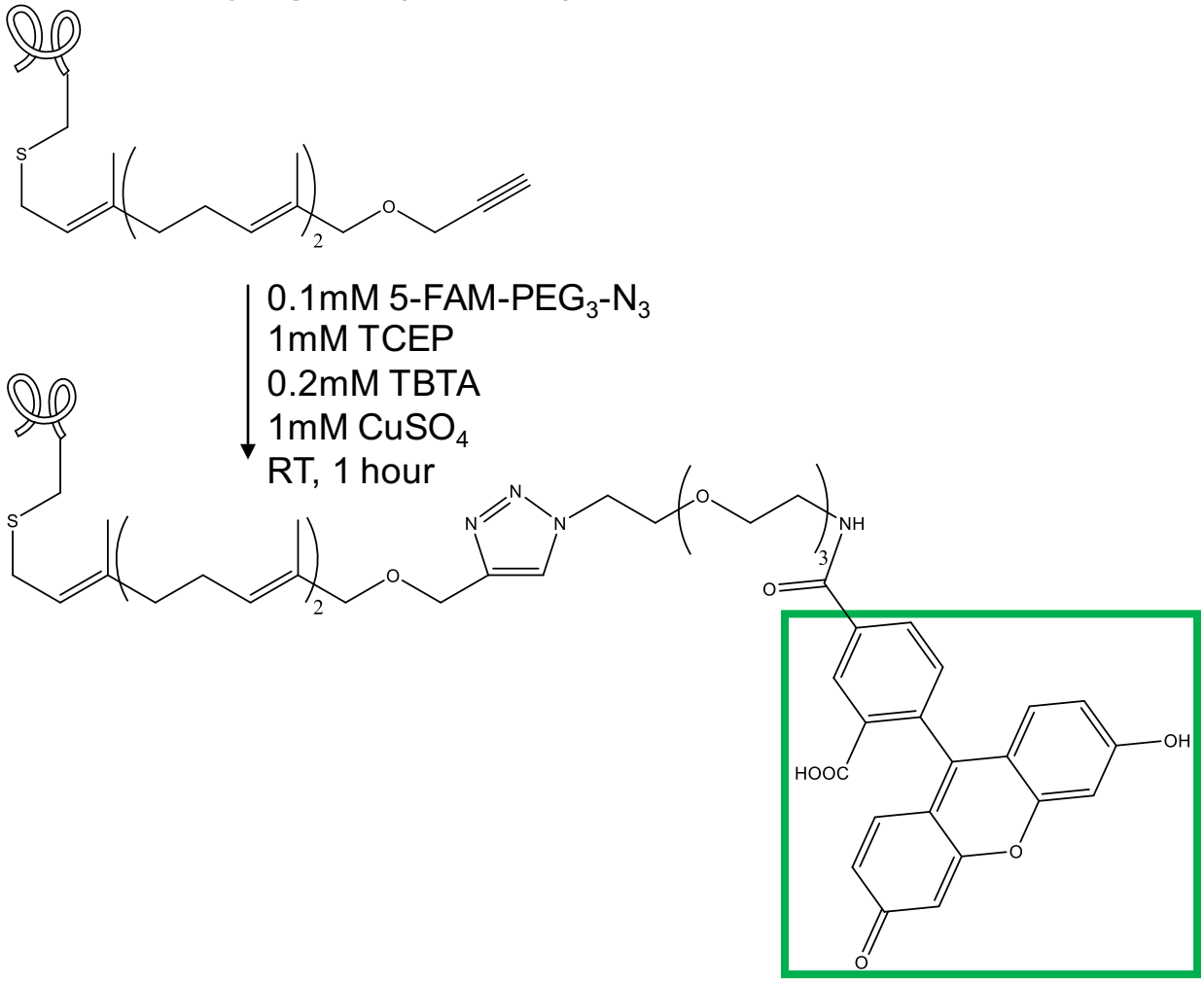

Supplementary Figure 3. Prenylation Assay. C15 alkyne is incorporated as a prenylation modification by farneysltransferase and geranylgeranyltransferase type-I onto the cysteine residues. Click chemistry is used to subsequently label the prenylation modification with a fluorophore, which is subsequently used for detection by flow cytometry.

Supplementary Figure 4 (Chapter 4)

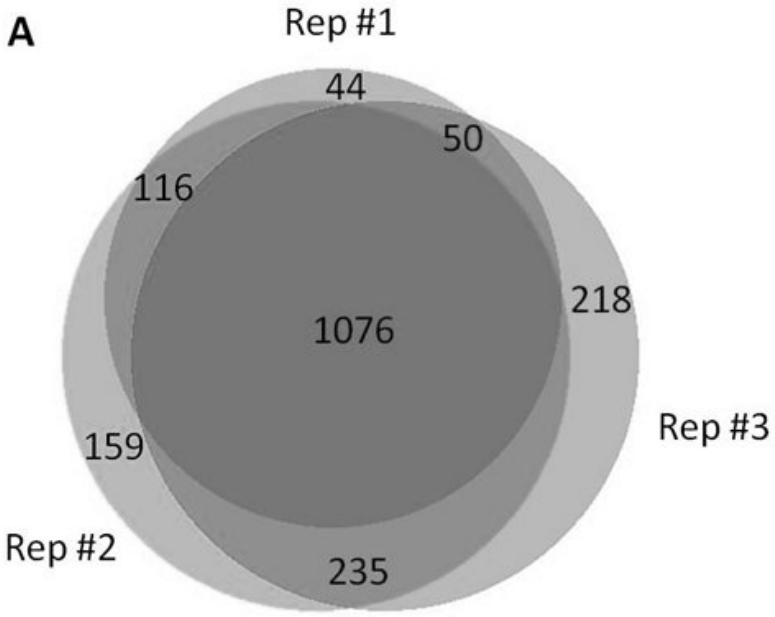

Supplementary Figure 4. (A) Bulk MS results of SILAC-labeled ATG7 siRNA treated and negative control siRNA treated L6 cells. Venn diagrams illustrate the overlap in protein identifications between the three biological replicates. There was ~57% overlap in protein identifications between all replicates (1076 proteins) with 1898 total non-redundant protein identifications (4451 total identifications, including duplicate identifications between biological replicates). This degree of overlap is consistent with the mass spectrometry method where the top eight most-intense peptide ions are processed for each survey scan, which reduces the frequency of sampling of low abundance peptides. Only about 0.1% of the proteins have a PEP score of 0.002 or higher (chance of misidentification is 0.2%), with the highest chance of misidentification at about 1% for a single protein. The vast majority of proteins have PEP scores less than 0.001. Such low protein PEP scores indicate high confidence in protein identifications for quantified proteins.[152] *Data collected by Michelle Kuhns.*

Supplementary Figure 5 (Chapter 4)

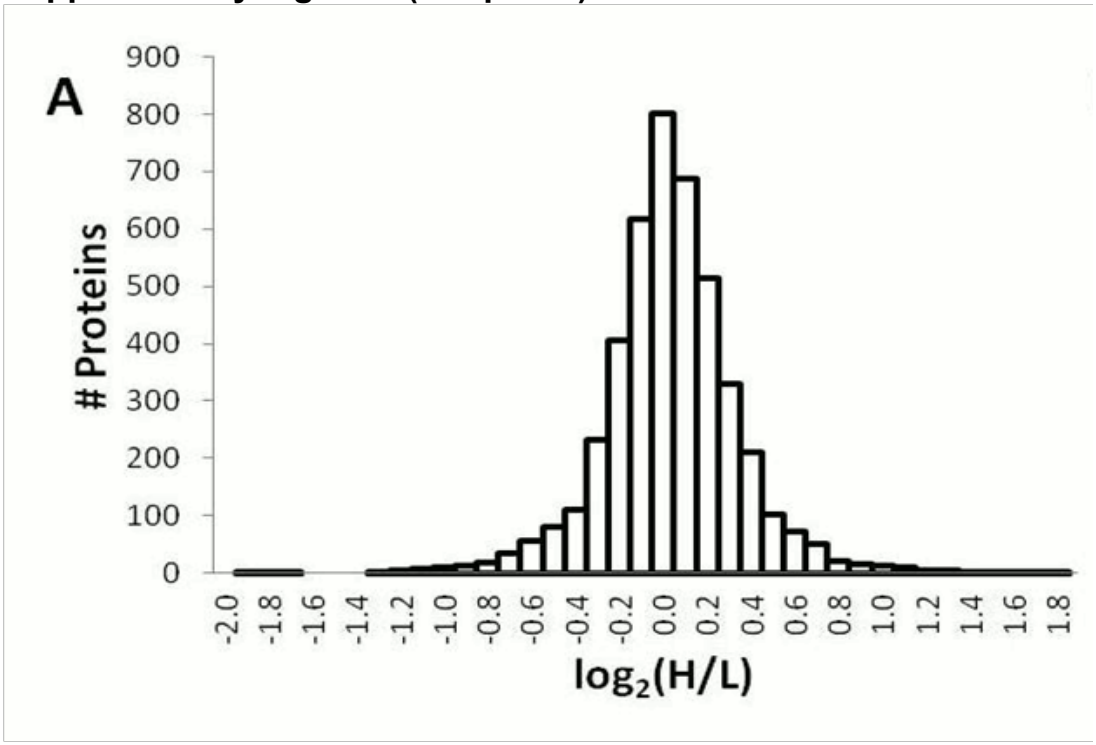

Supplementary Figure 5. (A) Histogram of SILAC ratios. This plot illustrates a symmetrical distribution around H/L = 1 (log2(H/L) = 0), indicating that there was not an experimental bias. An experimental bias would shift the distribution of H/L ratios away from unity or heterogeneous biological systems could result in overlapping distributions resembling multi-modal distributions.[180] The histogram includes the ratios found for all identifications in all three biological replicates (4432 proteins). Only 19 proteins had log2(H/L) values of greater than 2.0 or less than -2.0 (not included in histogram). *Data collected by Michelle Kuhns.*

Supplementary Figure 6 (Chapter 4)

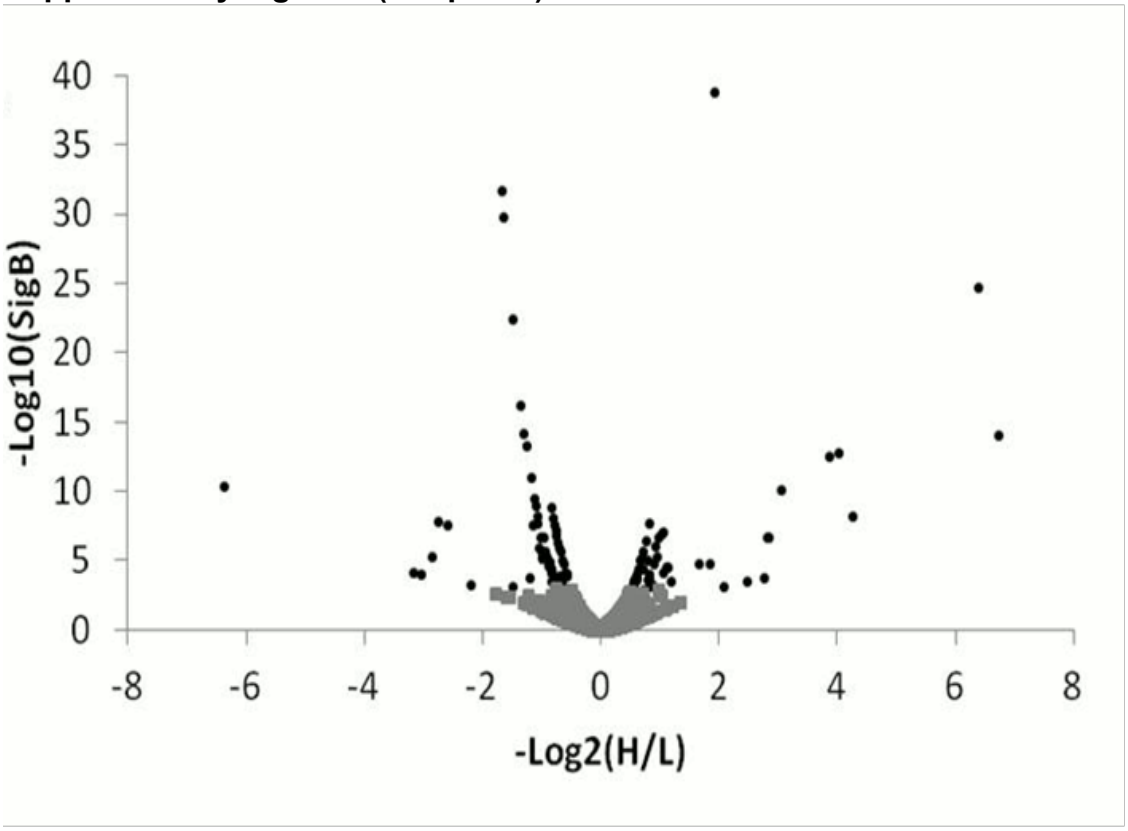

Supplementary Figure 6. Volcano plot of Significance B values versus H/L ratios. Proteins with significant changes in abundance appear in this plot as black dots while the majority of the proteins are not significantly changed in abundance with ATG7 siRNA treatment and appear as grey diamonds. Consistently, the relatively low number of proteins with significant changes in abundance defined by the Benjamini-Hockberg test (black dots in Figure 4C) have high –Log10(Significance B) and Log2(H/L) ≠ 1. One extreme (and significant) data point was excluded from this plot for ease of visualization (-Log10(SigB) = 212.5; -Log2(H/L) = -2.79). *Data collected by Michelle Kuhns.*